2019

Interfacial Mechanical Behavior Between Nacreous Tablets Under Normal And Shear Stresses

Saleh Jaman Alghamdi
University of Vermont

INTERFACIAL MECHANICAL BEHAVIOR BETWEEN NACREOUS TABLETS UNDER NORMAL AND SHEAR STRESSES

A Dissertation Presented

by

Saleh J. Alghamdi

to

The Faculty of the Graduate College

of

The University of Vermont

In Partial Fulfillment of the Requirements
for the Degree of Doctor of Philosophy
Specializing in Civil and Environmental Engineering

May, 2019

Defense Date: March 21st, 2019
Dissertation Examination Committee:

Ting Tan, Ph.D., Advisor
Jie Yang, Ph.D., Chairperson
Frederic Sansoz, Ph.D.
George Pinder, Ph.D.
Appala Raju Badireddy, Ph.D.
Cynthia J. Forehand, Ph.D., Dean of the Graduate College

Abstract

Nacre, a natural composite consisting of biogenic aragonite and protein, possesses superior strength and toughness compared to its brittle aragonite components. In this work, we first show that dry nacreous sections exhibit complete brittle fracture along the tablet interfaces at the proportional limit under pure shear of torsion. We quantitatively separate the initial tablet sliding primarily resisted by nanoscale aragonite pillars from the following sliding resisted by various microscale toughening mechanisms. In addition, we use the pure shear of torsion to demonstrate how hydrated nacre resists the initial tablet sliding by tuning its nanoscale toughening mechanisms. In hydrated nacre, hydrogen bonds between water molecules and organic matrices provide temporal paths for stress redistributions, through which the shear resistance is gradually transferred from mineral bridges to contacted nanoasperities. In the subsequent sliding, dynamical interactions between nacreous tablets enable substantial plasticity before the catastrophic failure of hydrated nacre.

Microscale growth layers between nacreous tables possess distinctive aragonite structures, including columns, spherulites and organic matrices. High temporal resolution experiments were performed to elucidate the tensile and shear behavior of growth layers under dry and hydrated conditions. Hydrated growth layers exhibited lower strengths and larger failure strain than hydrated nacre under both shear and tensile loadings. However, they successfully confined or deflected cracks within themselves when failure happened.

Keywords- *nacre, growth layers, torsion, pure shear, layered structures, multiscale toughening mechanisms*

Citations

Material from this dissertation has been published in the following form:

(1) **Alghamdi, S.**, Tan, T., Hale-Sills, C., Vilmont, F., Xia, T., Yang, J., Huston, D., Dewoolkar, M..(2017). Catastrophic failure of nacre under pure shear stresses of torsion. Scientific Reports, 7, 13123. (Top 100 in Materials Science by Scientific Reports in 2017)

(2) **Alghamdi, S.**, Du, F., Yang, J., Tan, T..(2018). The role of water in the initial sliding of nacreous tablets: findings from the torsional fracture of dry and hydrated nacre. Journal of the Mechanical Behavior of Biomedical Materials, 88, 322-329.

Material from this dissertation has been submitted for publication to *Journal of the Mechanics and Physics of Solids* on (2019) in the following form:

(3) **Alghamdi, S.**, Du, F., Yang, J., Tan, T..(2018). Tensile and shear behavior of microscale growth layers between nacre. Under review.

Acknowledgements

I would like to express my sincere gratitude to my advisor Prof. Ting Tan for his endless support, patience, motivation, and guidance. Besides my advisor, I would like to thank the rest of my dissertation committee: Prof. George Pinder, Prof. Jie Yang, Prof. Frederic Sansoz and Prof. Appala Raju Badireddy for their insightful comments and invaluable guidance. I would like to acknowledge the funding support from Taif University and Saudi Arabian Cultural Mission. I also would like to take this opportunity to express my sincere gratitude to my parents (Jaman, Abu Saleh, and Azza, Um Saleh) and my sisters (Suad, Ashwaq, Amal, Shahad and Bushra) for their unceasing encouragement and support. I would particularly like to thank my colleagues in Perkins 203A, and the members of my research group Yujie Li and Zhuang Liu who helped and supported me throughout this venture. My sincere thanks also go to Michele von Turkovich from the Scanning Electron Microscope at the University of Vermont.

Table of Contents

Content Page

List of Tables

List of Figures

Chapter 1: Introduction and Background

Nacre and growth layers in seashells have been studied extensively throughout the last few decades. This chapter aims to provide the necessary background information to facilitate understanding the topics discussed in this dissertation.

1.1 Introduction

Many of the materials found in nature exhibit exceptional mechanical properties such as high stiffness, toughness and strength [1-2]. One of these materials is nacre, which is a natural composite that can be found in the inner layer of many shells such as oysters and abalones [3-5]. Nacre, composes of a mineral and an organic material, i.e., aragonite and proteins, respectively. Nacre exhibits extraordinary strength, stiffness and toughness, which are believed to be results of its hierarchical brick-and-mortar microstructures [1,2,5-21]. One of the many shells that contains nacre is the shell of red abalone, shown in Fig. 1. It can be found along the west coast of North America, and their habitat is distinguished by its rockiness and the abundance of seaweeds. The location of their habitat ranges from intertidal zones to 30-meter-deep in water. In addition, red abalone feed mainly on seaweeds, particularly, bull kelp and giant kelp [22]. In their environment, abalones encounter numerous dangers, such as attacks from predators, heavy falling objects and other oceanic threats. Therefore, red abalone have evolved over the years and adapted an appropriate protection in the form of a shell [23]. The protective shell is large and thick

and can reach a maximum of 12.2 inches in diameter, which makes it the largest species of abalone in the world [23]. The shell's outer surface is pinkish to red and is described as rough and wavy. The shell's interior is iridescent with a large, oval muscle scar [22]. The red abalone shell was specifically selected to be studied in this work for two reasons: its comparatively large size and thickness which makes the preparation of torsion sample easier and more consistent. The second reason is the fact that red abalone's widespread usage in scientific research allows us to compare our findings to prior results. Red abalone shells essentially comprise of two basic components; calcium carbonate and proteins. The calcium carbonate components include both aragonite and calcite.

Nacre's microstructure is described as brick-and-mortar structure and is comprised of alternating layers of aragonite platelets (~500 nm thick) and organic matrices within the nanogaps (~30 nm thick), see Fig. 2 [1,5,7,14,28-30]. Furthermore, the structure of red abalone contains what is known as growth layers [31-33], which are layers of alternating aragonitic and organic structures in the shell, as shown in Fig. 2. The aragonitic components within the growth layers include both columns and spherulites that are harder than nacre [31,33]. In this dissertation, the strength and toughness along with the toughening mechanisms of nacre and growth layers are investigated under different loading conditions and hydration states.

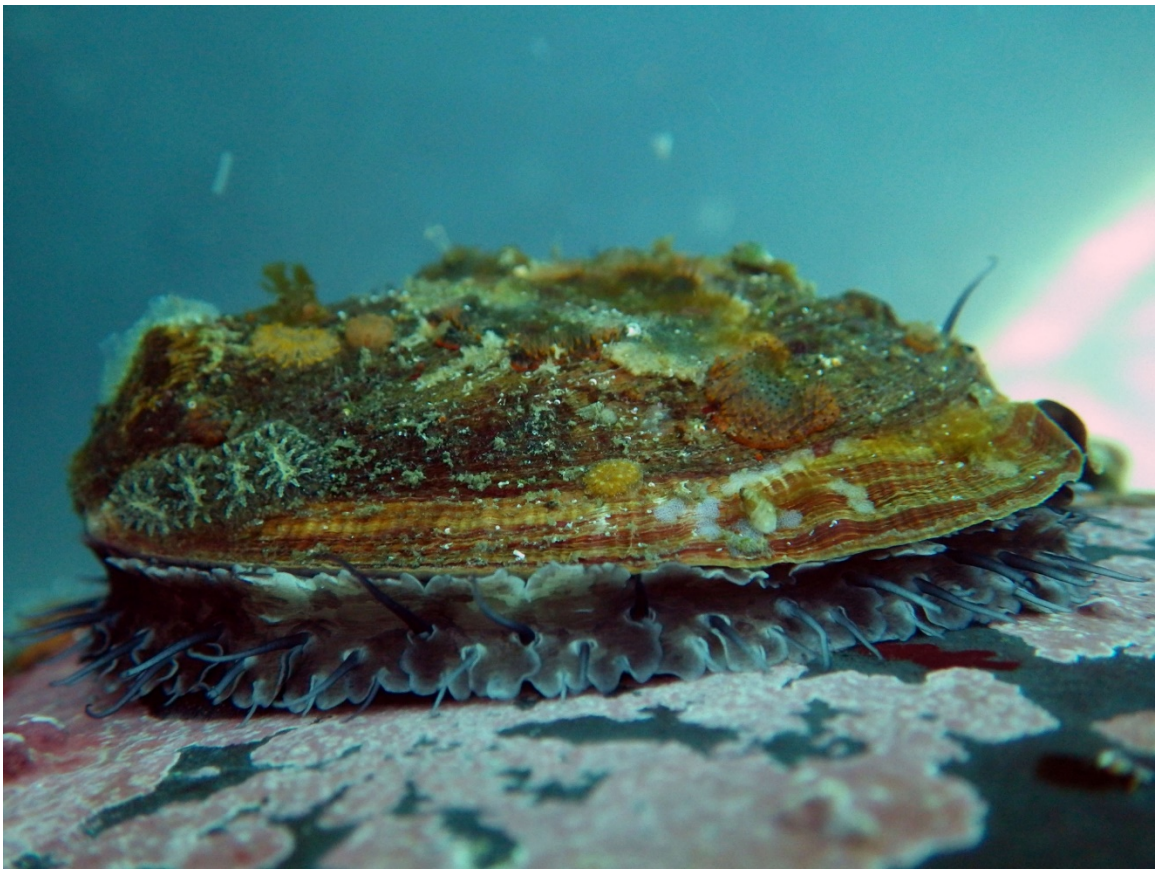

Figure 1: A photograph of a red abalone in its natural habitat [34].

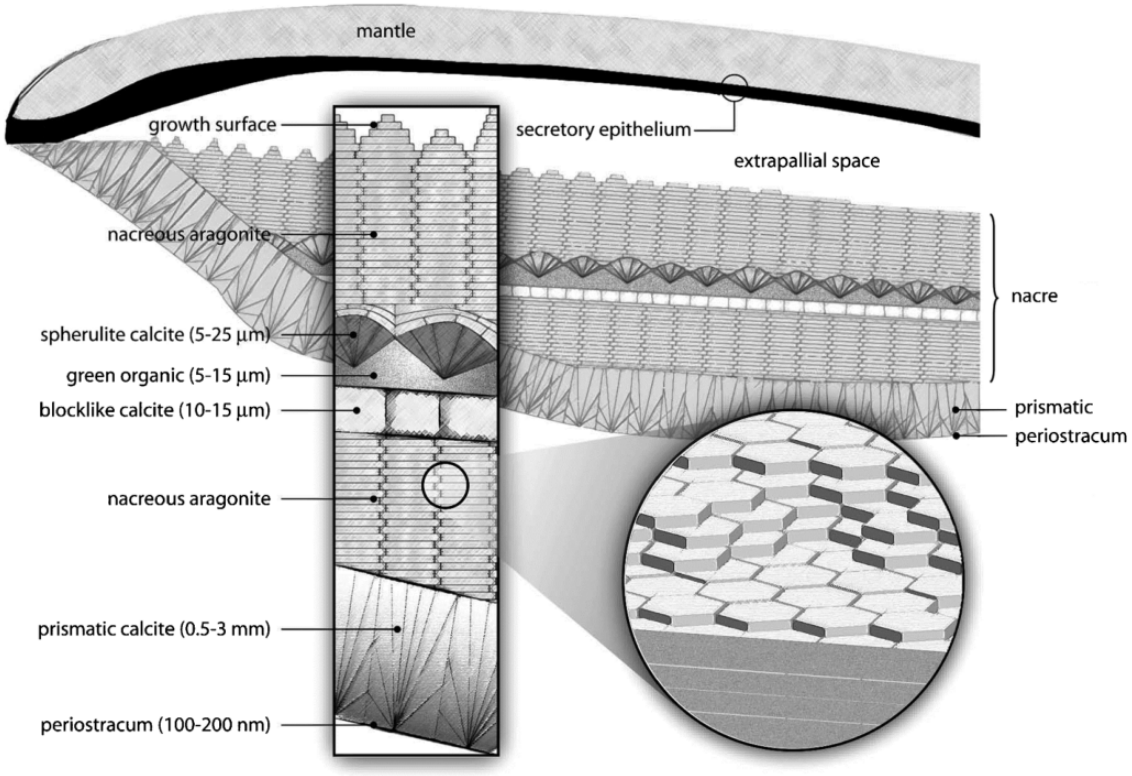

Figure 2: A cross sectional view of the shell of red abalone, showing calcite, nacre and growth layers [35].

1.2 Literature Reviews

Nacre from red abalone and from other seashells have been studied throughout the last three decades. This chapter further details the composition and mechanical response of nacre and growth layers under various loading conditions.

The main constituents of red abalone shells are minerals and proteins, the minerals are aragonite and calcite. Aragonite is believed to be the second most common polymorph of the natural calcium carbonate ($CaCO_3$). It is metastable and has the ability to transform

to calcite when environmental conditions are appropriate. Aragonite's morphology can be described as; short to long prismatic [100], flattened {010}; acicular or tabular {001} [36]. Aragonite has a strength of 30 MPa and has an elastic modulus ranging from 80 to 205 GPa [7,37-39] A typical fragment of a naturally-occurring calcite is shown in Fig. 3a. Calcite, on the other hand, is also a polymorph of calcium carbonate ($CaCO_3$) but is more common and abundant than aragonite, in fact, over 800 different forms have been documented. Calcite exhibits a relatively low Mohs hardness, and has different strengths along different crystallographic orientations [36]. A typical fragment of naturally-occurring calcite is shown in Fig. 3b. In red abalone shells, the outer layer is usually calcite while the inner layers are made of aragonite layers sandwiching proteins i.e., nacre.

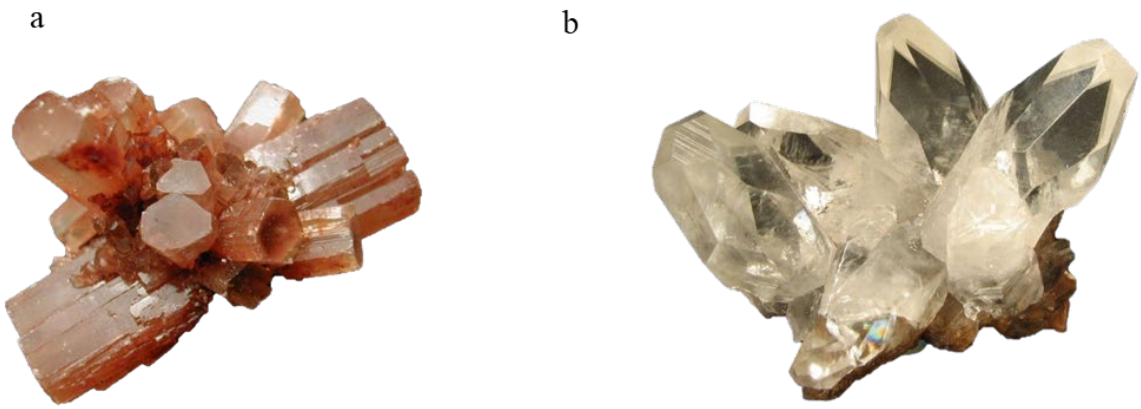

Figure 3: (a) natural aragonite and (b) natural calcite [36].

As mentioned in chapter 1, nacre is comprised of a hierarchical structure consisting of tightly stacked and organized polygonal aragonite platelet layers of thickness of ~0.5

μm. A thin layer of bio-polymers 20-50 nm composed mainly of proteins is sandwiched between the aragonite tablets [5,7,9,26,40]. The brittle aragonite tablets or "bricks" occupy around 95% of the volume of nacre, where the remaining 5% is occupied by the organic layer [38]. In addition, it is reported that nacre is 3000 times tougher than its fragile constituent, i.e., calcium carbonate ($CaCO_3$) [7,37,41]. To further understand these unique mechanical properties of nacre, immense research have been conducted over the past few decades. The high toughness of nacre is ascribed to how its organized microstructure deals with external loading. For instance, it is believed that sliding of the aragonite tablets and shearing of their interfaces contribute to the inelastic deformations observed in nacre's response [37,41,42]. Inside the nacreous interfaces, nano-asperities enhance the composite's toughness by providing interlocking mechanisms to resist tablet sliding [42-44]. In addition, mineral bridges are considered to be another nano-scale toughening component in the tablets' interfaces [25,45,46]. Moreover, upon studying the nano-scale structures of tablets from abalone nacre, Li et al. (2004) [11] suggested that nanograins strengthen nacre tablets and reduce the possibility of tablet braking during deformation. Barthelat et al. (2007) [39,41] reported that the wavy nature of the tablets, especially tablets' ends, contribute to the hardening and damage tolerance of nacre. Evans et al. (2001) [45] reported that the organic material is responsible for nacre's toughness. Other toughening mechanisms are reported in literature, including; tablet pull out, crack deflection and crack bridging [8,47].

While nacre's organic matter or "mortar" is made primarily of proteins, tablets or "brick" are made of aragonite tablets, where each "brick" is a polygonal tablet that is ~0.5

μm thick and 5-8 μm in diameter Fig. 4. Individual tablet has core overlap areas with both the top and bottom layer. This overlap is estimated to cover about 1/3 of the surface area of the tablet layers [48]. Barthelat et al. (2006) [44] conducted nano-indentation studies and showed that the elastic properties of nacre aragonitic tablets are very similar to those of biogenic single-crystal aragonite minerals. However, tablets show higher strengths than the documented values for biogenic aragonite. Li et al. (2004) [11] also used indentation as well as atomic force microscopy to examine the deformation behavior of nacre tablets. Their study involved creating micro-indentations on red abalone nacreous tablets to induce cracks. They show that radial cracks initiated and advanced along the interfaces of nacreous tablets in a zigzag manner. More importantly, instances of plastic deformations in the aragonite tablets were detected around the crack tips. They concluded that aragonite tablets are not entirely brittle but exhibit ductile behavior, that is due to the presence of the protein-glued nano-grains in the tablet's composition. Young's modulus of the nacreous tablets was reported in literature and ranged from 50 GPa [49], 70 GPa [43], 80 GPa [50], 100 GPa [37] to 205 GPa [51]

Besides aragonite, nacre contains 5% (by volume) organic matter, sandwiched between the tablets with a thickness of ~30 nm Fig. 4. The main constituent of the organic layer is protein, particularly, chitin (N-acetylglucosamine) networks and different other proteins [29,52-54]. By performing Fourier-transform infrared spectroscopic analysis, Verma et al. [55] revealed that there are different forms of water in hydrated nacre, including the partially hydrogen bonded water with organic matrices, the fully hydrogen bonded water clusters inside organic matrices or aragonite tablets, and the chemisorbed

water on the tablet surfaces. The organic matrices are believed to contribute to the mechanical behavior of nacre. Evans et al. (2001) [43] reported that the organic macromolecules (protein lustrin A in abalone nacre [56]) adds to nacre's toughness by working as a viscoelastic adhesive at the interfaces between tablets. Smith et al. (1999) [24] showed that when the protein chains are stretched, saw-tooth patterns manifest in the force-extension curves, indicating that the structures unfold or the sacrificial bonds break. This deformation mechanism of the matrix ligaments was confirmed by a transmission electron microscopy (TEM) study by Sumitomo et al. (2008) [57]. Additionally, Ghosh et al. (2007) [58] reported how proximity of proteins to aragonite tablets affects the unfolding mechanisms of proteins when pulled. They show that the amount of work needed to unfold proteins that are close to the aragonite tablets is substantially higher than when proteins domains are afar. The shear strength of the organic matrix was determined by Jackson et al. (1988) [5] to be around 37 MPa, with shear moduli of 1.4 GPa for wet organic matrix and 4.6 for a dry one; whereas a shear modulus value of 0.8 GPa was analytically calculated and reported by Barthelat et al. (2006) [59].

The interface of nacre contains other nanoscale structural features that contribute to its high toughness. These features include: Nano-asperities, which adds to nacre toughness by providing an interlocking mechanism when nano-asperities contact during sliding [43,60], see Fig. 4. Nano-asperities are found on the faces of the aragonite tablets. They are ~50 nm in diameter and 10-30 nm tall [26,61,62]. The density of nano-asperities on one tablet was estimated by Song et al. [45,46] as ~105/μm^2. Another feature on the surface of the aragonite tablets is mineral bridges (also known as shear pillars), see Fig. 4.

Mineral bridges are described as cylinders with diameters of ~50 nm and heights of ~30 nm. By treating the organic matrix layer as a fiber-reinforced composite, consisting of an organic matrix and fibers of the mineral bridges [25,46], reported that when shear pillars are present in the nacreous interface, the composite is five times stronger in resisting fracture than in the case where there are no mineral bridges in the nacreous interface. They also showed that when nacre is under three-point bending, resulting cracks propagate along the interfaces only but are eventually arrested due to the presence of mineral bridges in the interfaces. Song et al. (2001, 2002, and 2003) [25,45,46] estimated the density of mineral bridges on one aragonite tablet to be around 91-116 /μm^2. Further, they reported that bridges are more abundant in the central region of the tablet than the peripheral one. Overall, mineral bridges are believed to enhance the stiffness, the strength and toughness of nacre [25].

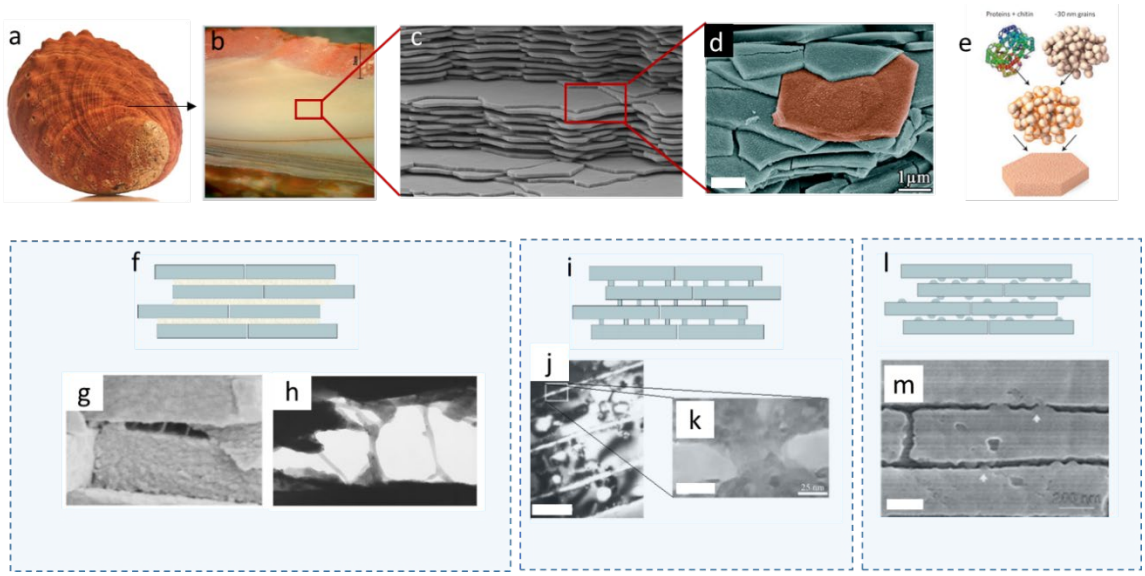

Figure 4: Structure of red abalone nacre. (a) Red abalone shell. (b) a cross sectional view of the red abalone shell where the top red layer is calcite, the beige layer is nacre and the brown lines are growth layers. (c) A scanning electron microscope image (SEM) of layered nacreous tablets (adapted from [3]). (d) An SEM image of individual tablets of nacre (adapted from [4]). (e) A schematic showing the composition of an individual nacreous tablet; i.e., nanograins and proteins (adapted from [2]). (f,g and h) organic matrix between nacre tablets (adapted from [24]). (i,j and k) mineral bridges between nacre tablets (adapted from [25]). (l an m) nano-asperities between nacre tablets (adapted from [26]). Scale bar in (d) 1 µm, (j) 330 nm (k) 25 nm and (m) 200 nm

When nacre is hydrated, its mechanical behavior is different from that of the dry nacre. Substantial research has been devoted to study the mechanical behavior of pure nacre under various loadings, i.e., under tension and compression [7,37,39,41,59,60,63,64]. Jackson et al. (1988) [37] calculated the tensile strength of nacre to be ~140 MPa for wet nacre and ~170 MPa for dry nacre. Further, Barthelat et al. (2006) [59] preformed tensile tests on dog-bone shaped samples of red abalone nacre and showed that nacre has elastic moduli of 70 and 90 GPa for wet and dry nacre, respectively. Tests

by Wang et al. (2001) [60] showed that when abalone nacre is tested in tension parallel to the tablets, it exhibits an elastic behavior up to a strain of about 0.15%, then continues at a steady-state stress level of at least 100 MPa until failure, which takes place at strain of 1%. The high inelastic strain was reported to be due to the dilatation bands occurring at the inter-tablets boundaries. In compression along the tablets, on the other hand, nacre shows a brittle behavior until failure. Additionally, Barthelat et al. (2006) [44] studied nacre under compression across the tablets and demonstrated that it exhibits an average strength of 450 MPa. Barthelat et al. (2007) [41] also tested nacre in tension along the tablets and observed that dry nacre behaves like a brittle material and fails when tensile stress reaches an average of about 114 MPa, which is similar to the tensile strength of pure aragonite. Wet nacre, on the other hand, shows an elastic behavior up to a strain of 0.06 %, then exhibits an inelastic deformation until failure. Furthermore, Barthelat and Espinosa (2006) [44] tested nacre in tension across tablets and reported that it exhibits a strength of 15 MPa. Nacre from red abalone was also evaluated by Menig et al. (2000) [65] under different compressive loading rates and sample orientations. By preforming Weibull analyses with the fracture probability of 50%, they estimated the compressive strength of nacre to be 235 MPa when the loading is quasi-static and is parallel to the tablets; and 540 MPa for loading direction perpendicular to the layers of tablets. In contrast, under dynamic loading, the compressive strength of nacre increases by about 50% to 548 MPa when tablet layers are parallel to the loading direction, and to 735 MPa when the layers are perpendicular to the compressive load direction.

Nacre was also tested under bending [37,60,64]; Jackson et al. (1988) [37] performed three-point bending experiments on nacre and reported that dry nacre (E=70 GPa) from *Pinctada* shell is stiffer than wet nacre (E=60 GPa). Similar tests were performed by Wang et al. (2001) [42] on nacre samples that were taken from pearl oyster and red abalone. They showed that both flexural strength and Young's modulus of red abalone are higher when the orientation of the tensile surface is parallel to the lamellar boundaries.

Beside bending and normal loadings, nacre was also tested under shear [39,44,65,66] and 45° shear tests ([39,42,44]). Menig et al. (2000) [67]determined the shear strength of nacre by applying shear stresses to small cube-shaped samples of nacre from abalone an abalone shell. The applied load was parallel to the tablets' layers of nacre, with the goal of generating a shearing action on a 2 mm-wide gap in the cube. The stress-strain curves exhibited a linear segment up to 12 MPa, followed by another segment that monotonically increased until failure. A shear strength of 30 MPa was obtained with a corresponding shear strain of 0.45. Using a similar test set-up, Barthelat et al. (2007) [48] studied the interfacial shear behavior in wet and dry nacres with the help of an optical microscope for strain measurements. Similar to Menig et al., (2000), the direct shear tests were conducted on cube-shaped nacre samples. For both dry and hydrated nacre, test results showed an elastic region followed by an inelastic shear deformation and strain hardening. However, the yielding shear strengths of dry and wet nacre were different, i.e., 55 MPa and 20 MPa and shear moduli of 14 GPa and 10 GPa for dry and wet nacre, respectively. In addition, they observed that for both dry and wet samples, a significant amount of

expansion across the tablets took place during the shearing process. They concluded that this lateral expansion was due to the presence of obstacles in the nacreous interfaces. Additionally, a combined shear and compression test was performed to study the impact of compressive stresses on the shearing resistance of dry and hydrated nacre. Results showed that although compressive stresses have limited effect on the shearing resistance of wet nacre, they cause dry nacre to exhibit higher shear strength. Lin et al. (2009) [66] also studied the interfacial shear strength of abalone nacre using a similar test set-up as Menig et al., (2000) but with a smaller shearing gap. Instead of a shearing distance of 2 mm, a 200 μm distance was chosen to ensure that the shearing occurs in the nacreous regions between mesolayers and does not slide across them. The resulting shear strength was 36.9 ± 15.8 MPa with the corresponding shear strain of 0.3. Fracture studies have also been conducted on nacre, for example, it has been reported that the fractured hydrated nacre exhibits more pulled-out nacreous tablets, whereas the fractured dry nacre exhibits more broken tablets [68]. In addition, Jackson et al. (1988) [37] investigated nacre's work of fracture via bending tests and reported that it ranges from 350 to 1240 J/m^2, depending on various facets, such as the span-to-depth ratio and the degree of hydration. This work of fracture value is 3000 greater than that of pure calcium carbonate. Sarikaya et al. [8,47] tested single notched red abalone nacre samples using 3-point and 4-point bending tests and reported that nacre has a fracture strength of 185 ± 20 MPa and a fracture toughness of 8 ± 3MPa $m^{1/2}$.

In addition to mechanical experimentations, different analytical and numerical models have been implemented to understand the mechanical behavior of nacre. For

instance, Kotha et al. (2001) [69] developed a two-dimensional shear-lag model to study how stresses transfer between the nacreous tablets. Their results suggested that in order to synthesize high toughness nacre-inspired materials, the tablets' aspect ratio must be small. Further, Bertoldi et al. (2008) [70] proposed a two-dimensional micromechanical model to analyze the macroscopic behavior of nacre. It was shown that it is imperative that nacre's bi-modularity and anisotropy be taken into consideration for a valid interpretation of the experimental data. Nacre's response has also been modeled computationally, for instance, Barthelat et al. (2007) [41] created a three-dimensional FEM model to show if tablets' waviness has the potential to enhance the toughness of nacre. Furthermore, Evans et al. (2001) [43] used FEM models to show if nano-asperities, along with other toughening mechanisms, are responsible of the high toughness observed in nacre. Their results suggested that nano-asperities contribute to the inelastic deformation of nacre by causing strain-hardening to occur, and that it is high enough to ensure that a sufficient number of dilatation bands are formed. At the same time, the strain hardening cannot be so large that nacreous tablets break internally. In addition, Katti et al. [51,71] also developed three-dimensional FEM models to investigate multiple toughening mechanisms and overall behavior of nacre. Furthermore, Dashkovskiy et al. (2007) [72] used a two-dimensional FEM models to study how the organic matrix's incompressibility affects the elastic modulus of nacre. Additionally, Barthelat et al. (2006) [44] modeled the inter-tablet interfaces in nacre and concluded that during early stages of tablets sliding, nano-asperities are strong enough to resist that sliding and withstand nano-asperities climbing.

The structure of red abalone contains what is known as growth layers or growth lines [31,33,73], which are bands of alternating aragonitic and organic structures, see Fig. 5. The growth of nacre has been an intriguing research topic for many years [13,26,28,74-83]. Several essential growth interfaces are present in the layered composite at different growth stages, such as the organic matrices between adjacent nacreous tablets [32,75], the calcite-nacre transitions [81,84-87] and the growth lines between bulk nacre [31,32]. For the calcite prism-aragonite nacre transitions, Gilbert et al. [81] used the synchrotron spectromicroscopy to measure crystal orientations, tablet sizes and tablet stacking directions of *H. Rufescens.* They reported that orientation ordering occurred gradually over a distance of 50 μm. A theoretical model [81,88] based on kinetics and the selection of fastest growth rates generated predictions that were in good agreement with the experimental measurements. They found that the spherulitic aragonites at the calcite prism-nacre transitions maintained the same crystal orientations as those in pure nacre. Dauphin et al. (2008) [85] studied the early nacre-calcite prism transition of *P. Margaritifera* using an integrated microstructural, mineralogical and chemical approach. They identified three growth stages in the transition with distinctive microstructural and biochemical compositions, i.e., the completion of calcite prisms, formation the fibrous layer, and development of organized nacreous layers. Griesshaber et al. (2013) [86] used the high-resolution, low acceleration voltage electron backscatter diffraction (EBSD) to study the calcite-aragonite polymorph interface in *M. Edulis*. They observed that a 1-2 micrometer wide granular aragonite layers exist, exhibiting a high density of organic matrix and a relatively low degree of preferred crystallographic orientation. Hovden et al. (2015)

[87] used the high-resolution scanning transmission electron microscopy and the wedge-polishing technique to investigate the onset of nacre from calcitic prims to aragonite tablets of *P. Nobilis* over the entire interface. They reported a transition from nanofibrillar aggregation to irregular early-nacre layers, to well-ordered mature nacre. The assembly process was driven by the aggregation of nanoparticles (~50-80 nm) within an organic matrix with fiber-like polycrystals. In freshwater bivalves, the outer prisms could be constructed from aragonite. Freer et al. (2009) [89] used EBSD to study the aragonite prism-nacre interfaces of two freshwater molluscs, i.e. *A. Anatine* and *A. Cygnea*. In *A. Cygnea*, the nacre below prisms was featured by distinct concave imprints; but these were not found in *A. Anatine.* In both species, the overall crystallographic orientation, i.e., the *c*-axis of nacre, was perpendicular to the nacre-prism interface. In *A. Cygnea*, where alternate prisms had slight deviations from the perpendicular, the crystallographic orientation adjusted very quickly (within a few micrometers) to the regular nacre orientation. Microscale periodic growth layers occur between bulk nacre with thicknesses ranging from 15 to 300 μm. These variations are related to the age and seasonal changes, such as water temperature, current and feeding interruptions [31,40,73,81,90-94]. Su et al. (2002) [31] elegantly showed that the growth layers of *H. Rufescens* include different aragonite structures, i.e., columns, a green matrix and spherulites. The columns are aragonite crystals with central cores aligned along the *c*-axis of nacreous tablets, where spherulites are cone-shaped aragonite crystals with radially-scattered lines on the conical surfaces. The green matrix is a polymeric composite mainly composed of protein and polysaccharides with distinctive structural and compositional properties on both sides [92]. It was reported that

one side, the richer in tyrosine, is fabricated to ensure high adhesion of the green sheet to the prismatic crystals of aragonite, while the other side facilitates mineral deposition. Gilbert et al. (2008) [81] also reported the presence of spherulitic aragonite in the growth lines between bulk nacre. The introduction of these growth layers leads to different mechanical behavior of the composite from that of pure nacre sections. By performing bending tests using nacreous sections with growth layers, Lin and Meyers (2005) [40] showed that growth layers of *H. Fulgens* effectively deflected cracks between tablets so as to hinder crack propagations. Sumitomo et al. (2011) [33] used nanoindentation techniques to study the mechanical properties of growth lines in *H. Gigantean*. They reported that the columns and spherulites exhibit relatively higher elastic moduli and hardnesses than nacreous tablets even though they are all made of aragonite crystals. Lopez et al. (2014) [95] studied the tensile strength of demineralized and deproteinized nacre. Results showed that the mesolayers contributed limitedly to the composite strength, and their primary role is to control crack paths. Zhang (2017) [30] used nanoindentation tests to measure the elastic moduli of growth layers in *H. Rufescens*. Their results showed that the spherulites and columns exhibited substantially higher elastic moduli than the green matrix. These studies shed essential lights on the understanding of microscale growth layers between bulk nacre.

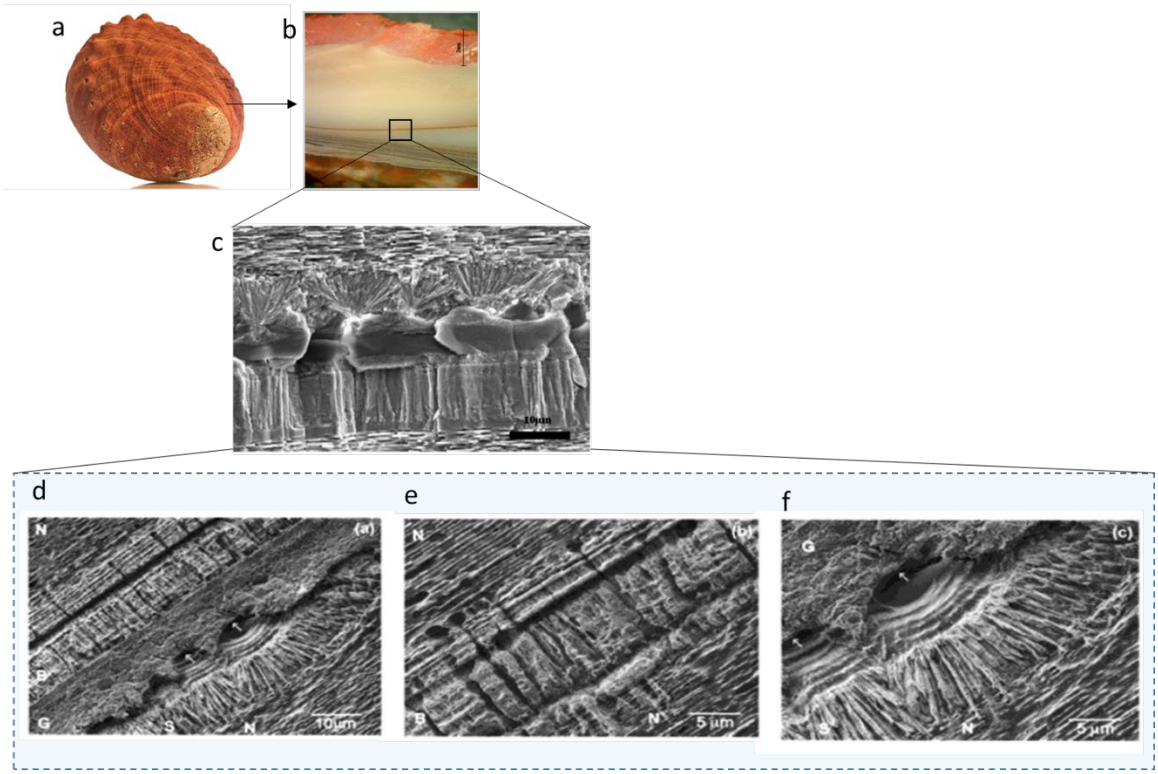

Figure 5: Structure of red abalone growth layers. (a) Red abalone shell. (b) a cross sectional view of the red abalone shell where the top red layer is calcite, the beige layer is nacre and the brown lines are growth layers. (c) SEM image of cross section of growth layers (adapted from [26]). (d) SEM image showing green matrix. (e) SEM image showing column-like structures, and (f) SEM image showing spherulites. (d,e,and f were adapted from [31]).

1.3 Mechanical properties

Based on the literature review in Section 1.2, the young's modulus, shear modulus and Poisson's ratio of nacre, nacreous tablets and organic matrices are summarized in table 2.

Table 1: Summary of upper and lower bounds of the reported mechanical properties of nacre and its constituents. Values in curly brackets are used by researchers in their models.

Young's modulus (GPa)		
Nacre [39],[32]	**Tablets** [49],[51]	**Organic matrix** [59],[96]
70-90	50-{205}	0.02-{20}
Shear modulus (GPa)		
Nacre [39]	**Tablets**	**Organic matrix** [37]
14	-	1.4-4.6
Poisson's ratio		
Nacre	**Tablets** [39],[51]	**Organic matrix** [51]
-	{0.2}-{0.3}	{0.1 to 0.499}

1.4 Hypotheses

In this dissertation, four related topics have been studied, for the first topic, the catastrophic failure of nacre under torsion, we hypothesized that when torque is applied about an axis that is orthogonal to a plane parallel to the nacreous interfaces, the resulting pure shear stress gradient will disclose new insights into the mechanical behavior of interfaces between nacreous tablets, such as that mineral bridges will contribute the most to the interfacial sliding resistance during the initial tablets sliding stage.

In the following study, the effect of water on the initial sliding of nacre, we hypothesized that hydrated nacre will behave differently than dry nacre under torsion. In

particular, we assumed that the presence of water will enable the ductility of interfaces between nacreous tablets.

In the study of tensile and shear behavior of microscale growth layers between nacre we hypothesized that inclusion of the growth layers in the samples' gauge sections will yield a response that is different from the response of samples containing pure nacre only, in both dry and hydrated conditions. In particular, the structures of the growth layers will affect the deformation process resulting in lower overall strength but generally larger failure strains.

1.5 Objectives

In the past three decades, nacre has been extensively studied using a variety of experimental, analytical and numerical approaches. Despite these efforts, limited research exists to quantify the shear behavior of dry and hydrated nacre, and how abalone resists external loads through their composite layers, i.e., the alternating nacreous and growth layers. In addition, the interfacial interactions between nacreous tablets during sliding has not been experimentally detailed. Thus, we employ integrated experimental and theoretical approaches to study these topics and generate new knowledge.

Chapter 2: Catastrophic Failure of Nacre under Pure Shear Stresses of Torsion

In this work, we focus on separating adjacent nacreous tablets using pure shear stresses of torsion [97,98]. We created composite dog-bone shaped specimens using the pure nacreous sections without any growth layers [31,32,90,99] from a red abalone shell. The hexagonal surfaces of aragonite tablets are perpendicular to the cylindrical axis (Fig. 6b). For a shaft under torsion, pure shear stresses exist in every two-dimensional cross-sectional planes over the entire gauge section. This feature enables the nanoscale interfaces between nacreous tablets to be tested successfully. The shear stress and strain in torsion are described by

$$\tau = \frac{T \cdot \rho}{J} \tag{1}$$

$$s_{max} = \Delta\theta \cdot r = \gamma_{max} \cdot l \tag{2}$$

Where τ is the shear stress on the horizontal plane of the gauge section, T is the torque, r is the gauge section radius, ρ is the distance between an arbitrary point on the cross section to the center varying from 0 to r, $J=0.5\pi r^4$ is the polar moment of inertia, γ_{max} is the shear strain at the external edge, s_{max}, $\Delta\theta$, and l are the sliding distance at the external edge, twisting angle, and height of adjacent tablets, respectively. Since nacre specimens are transversely isotropic, shear stresses increase linearly from zero in the center to the

maximum in the external edge before the specimen fails. τ_b represents the shear stress distribution before the specimen failure. Once the external aragonite tablets fail, large gradients of shear stresses occur radially due to the rapid decrease in the polar moment of inertia, which is a fourth-order function of the cylindrical radius. These gradients promote fast crack propagations radially until the specimen fails completely. τ_a represents the shear stress distribution after the specimen failure. In this study, the failure of specimens is achieved when the interfacial shear strength is reached. The maximum tablet sliding distance upon failure is measured as the maximum rotational distance between two adjacent brick layers at the external edge. The shear strain is the ratio between the sliding distance and the height of adjacent tablets (Fig. 6c). In the experiments (Fig. 6a), the axial load was precisely controlled (~0.22 N), and the catastrophic failure after peak load was detailed using data collected at a high sampling rate (200,000 samples per second).

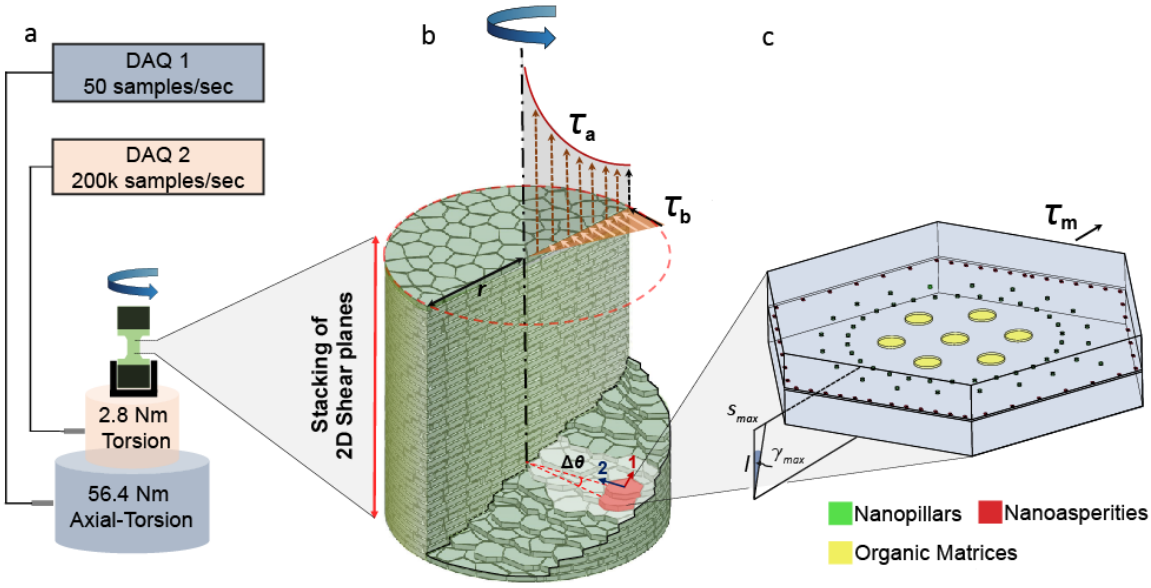

Figure 6: Schematics of the experimental system. (a) The dual system that includes an axial-torsional load cell (4.4 kN and 56.4 Nm) at the sampling rate of 50 samples per second and a torsional load cell (2.8 Nm) at the sampling rate of 200,000 samples per second. (b) Distributions of pure shear stresses of torsion before (τ_b) and after (τ_a) the failure of nacre specimens. Arrows 1 and 2 denote the sliding and crack directions, respectively. (c) A close view of two tablets at the external edge of the gauge section subjected to the maximum shear stress (τ_m) before failure. This geometrical model was used in the finite element analysis.

2.1 Results and discussion

Pure shear stresses generate complete brittle fracture of nacre. A total of five successful composite dog-bone shaped nacre specimens (Fig. 8a) were created due to the scarce of pure nacre sections in red abalone shells. For each specimen, the torque-rotation curve collected during quasi-static monotonic torsional tests exhibits an increase and a sharp drop (Fig. 7a). The increase segments are almost linear since R^2 values of the linear fitting are above 0.99 for all specimens (Fig. 7c). The shear strength is 41.5 ± 14.7 MPa at 2.0 ± 0.8% strain. The variation is due to the specimen locations in the red abalone shell.

The post-peak curves are nearly vertical, showing that catastrophic failures happen in a short time (Figs. 7a and 7b). In comparison, single-crystal aragonite minerals were shaped to the same size and orientation of nacreous specimens. The shear strength of aragonite is 14.5 ± 2.2 MPa at 1.4 ± 0.2% strain. Although the R^2 values of aragonite segments are close to unity, the relatively flat drop (Fig. 7b) indicates that crack propagations are affected by the spiral fractural surfaces (Fig. 8d). For the same geometry, cracks travel faster between the nacreous tablets than in aragonite minerals since the dropping periods of nacre specimens last shorter (5.0 ± 2.0 milliseconds) than those of aragonite specimens (20.0 ± 0.6 milliseconds). By discretizing the twisting angle of the gauge section to the rotational angle of two adjacent tablets, the measured sliding distance at the external edge in the initial stage is ~20 nm (20.0 ± 8.4 nm) that agrees with prior estimations[43].

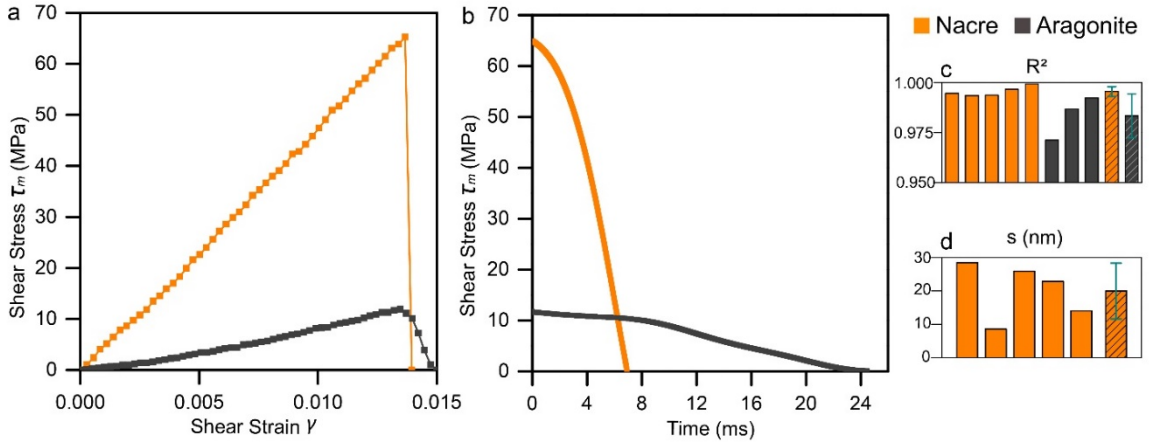

Figure 7: Monotonic torsional tests for nacre and aragonite specimens. (a) Shear stress-stress curves. (b) Post-peak drop periods with respect to time. (c) R^2 values of the linear-fitting for the increase segments. (d) Sliding distances of adjacent nacreous tablets.

Fractographic characterization proves interfacial fracture in nacre. We observed two flat surfaces over the entire 3mm-diameter circular cross sections of nacreous specimens after failure (Figs. 8a-8c). Under the white light, the flat surface exhibits a combination of green ($\lambda \approx 510$ nm) and yellow ($\lambda \approx 570$ nm) colors, which is different from the iridescence of the inner surface of red abalone shells. The reason is that uniform horizontal tablet (~500-nm thick) layers underneath reinforce lights with specific wavelengths over the entire fracture surface. Elevated tablet sections appear on the left (Figs. 8b and 8c). This is because pure shear stress condition is no longer maintained once cracks start to propagate after the failure of external tablets. As a result, cracks kink from one interface to another that eventually separate the specimen. Detail SEM image (Fig. 8e) shows that large areas of tablets are exposed and are interlaced with broken edges that transit spirally from one layer to the next [100]. The broken edges (Fig. 8f) include both the smooth intertablet delamination and brutal transtablet breakage. However, these sharp edges are different from the blunted edges of polished nacre specimens [101], demonstrating that tablets and spiral connections are quickly removed during crack propagations. The microCT image (Fig. 8d) clearly shows the different brittle fracture of aragonite specimens. Aragonite specimens exhibit a classical 45-degree helical fracture perpendicular to the principal tensile stress, while nacreous specimens fracture sharply through the interfaces between aragonite tablets.

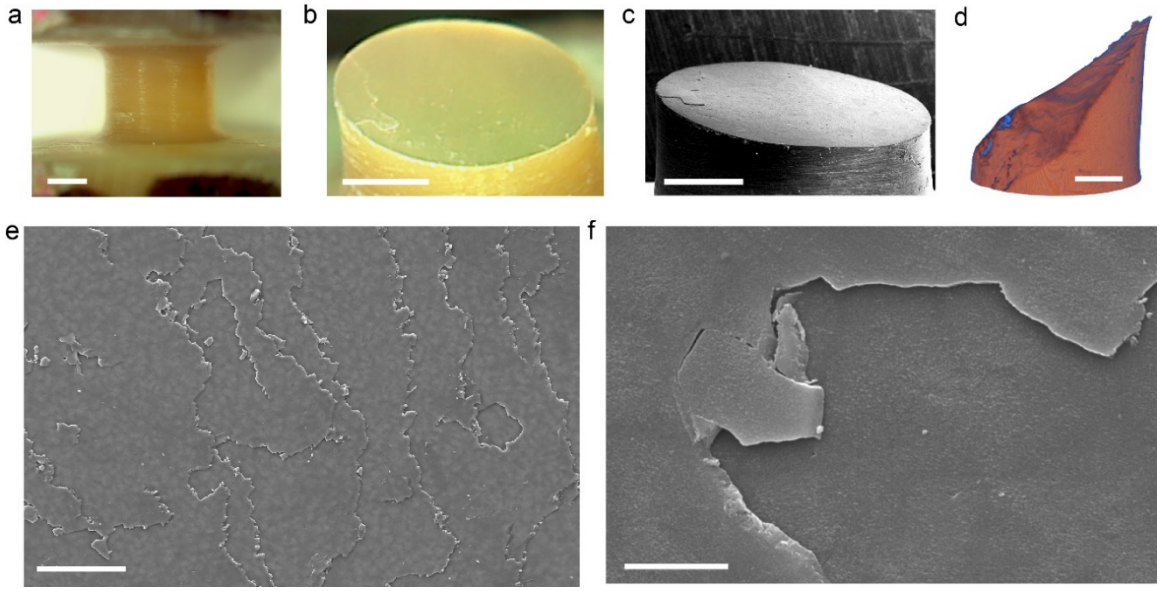

Figure 8: Fractographic characterization. (a) A representative dog-bone shaped nacre specimen. (b) and (c) Optical and SEM images of the fractured nacre half, respectively. (d) A microCT image of a fractured aragonite half under torsion, showing a 45˚ helical fracture. (e) A closer view of broken edges and interlayer spiral transitions of nacreous specimens. (f) A detail look at inter- and transtablet breakage of nacreous tablets under pure shear stresses of torsion. The scale bars are 1 mm in (a), (b), (c), (d), 50 μm in (e), and 5 μm in (f).

Mathematical modeling quantifies nanoscale toughening mechanisms. To detail the nanoscale toughening mechanisms in the initial sliding stage, we created isotropic linear elastic finite element models to quantify the contribution of nanopillars, nanoasperities and protein chains to the shear resistance. A contour of an exposed tablet (Fig. 9a) shows that stresses in nanopillars and nanoasperities (E=100 GPa) are substantially higher than those of protein chains (E=20 MPa) due to the significantly different elastic moduli. The lower and upper bounds of shear stress curves (Fig. 9b) correspond to nanopillar densities of 1.4 and 5.6/μm^2, respectively. The mean shear strength (~41.5 MPa) curve corresponds to a density of ~2.2/μm^2. By decoupling the contribution of each mechanism with respect to

various tablet moduli (E=80 to100 GPa) and pressures (p= -35 to 35 kPa), Figure 9c shows that nanopillars contribute to more than 95% of the shear resistance, while nanoasperities and protein chains contribute limitedly in the initial sliding stage. High shear stresses in the middle section of nanopillars (~1.0 GPa) enable their breakage at the end of the initial sliding stage. Compared to the shear strength of aragonite mineral specimens (~14.5 MPa), nacreous nanopillars exhibit much higher shear resistance, demonstrating the 'smaller-is-stronger' size effect down to the nanoscale.

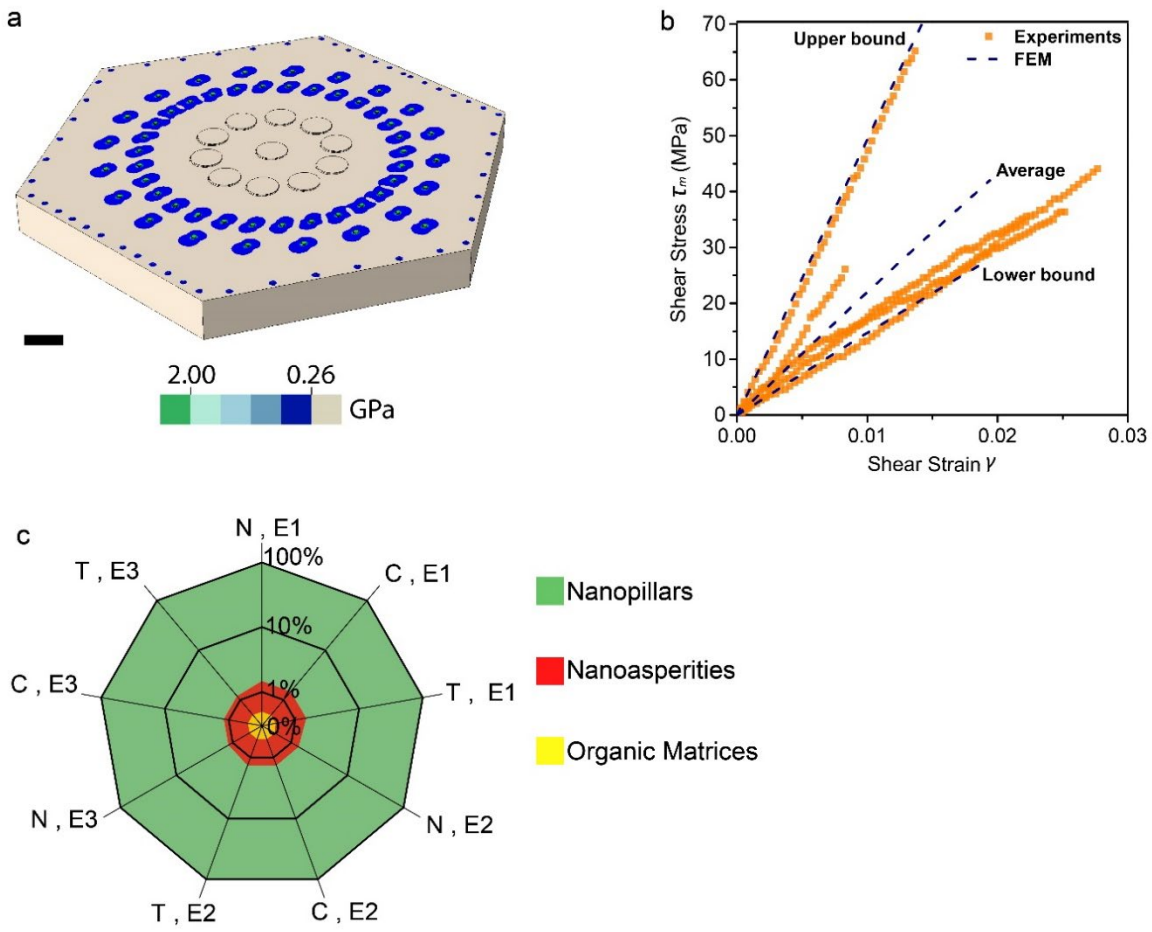

Figure 9: Mathematical modeling. (a) Mises stress contours of nanopillars, nanoasperities and organic matrices at the end of the initial sliding. (b) Predictions of the upper, lower and average shear stress lines in the torsional tests. (c) Contributions of nanopillars, nanoasperities and organic matrices to the shear resistance of nacre in the initial sliding stage. E1, E2 and E3 correspond to the elastic moduli of 100, 90 and 80 GPa, respectively. N, C and T denote zero, compressive (-35 kPa) and tensile (35 kPa) stresses on tablets, respectively. The scale bar is 500 nm in (a).

The Achilles heel of nacre. If we define the intact nanopillars, nanoasperities and protein chains before sliding as 'mortar', the ductile or brittle behavior of nacre is highly dependent on how bricks (tablets) perform after mortar sections fail. When mineral bridges break after sliding about twenty nanometers, distances between tablets decrease (Figs. 10a and

5b). In most stress conditions, contact areas between tablets increase gradually and substantially as cracks propagate completely or partially parallel to the sliding direction (Fig. 10c). The toughening mechanisms then change to the nanoasperity contact in nanoscale, and to interactions of wavy tablets, tablet pulling-out and crack deflections in microscale [2,102,103] (Fig. 10d). For example, when nacre is in tension along the tablets [7,56,60], mortar sections fail first (the linear increment), and some tablets start to touch each other (the nonlinear increment). Then, microscale toughening mechanisms are triggered at various locations continuously (the extended stress plateau). Similar behavior exists in nacre under compression [65,104], bending [60], 45-degree shear [41,60] or direct shear [41,66]. However, when nacre is under torsion normal to aragonite layers, the sliding of tablets (tangential) is perpendicular to the crack propagation (radial), and the large stress gradients enable the specimen to fail quickly (Fig. 6b). Thus, nacre exhibits completely interfacial brittle fracture since there is little chance for brick interactions after the mortar sections fail (Fig. 10e). The Achilles heel of nacre is to avoid triggering microscale toughening mechanisms that can induce the ductile behavior. The discretization nature of torsional loads enable us to study nano- and microscale material behavior using relatively large specimens. Torsion can be particularly advantageous to study interlayer/interfacial mechanical behavior of layered materials.

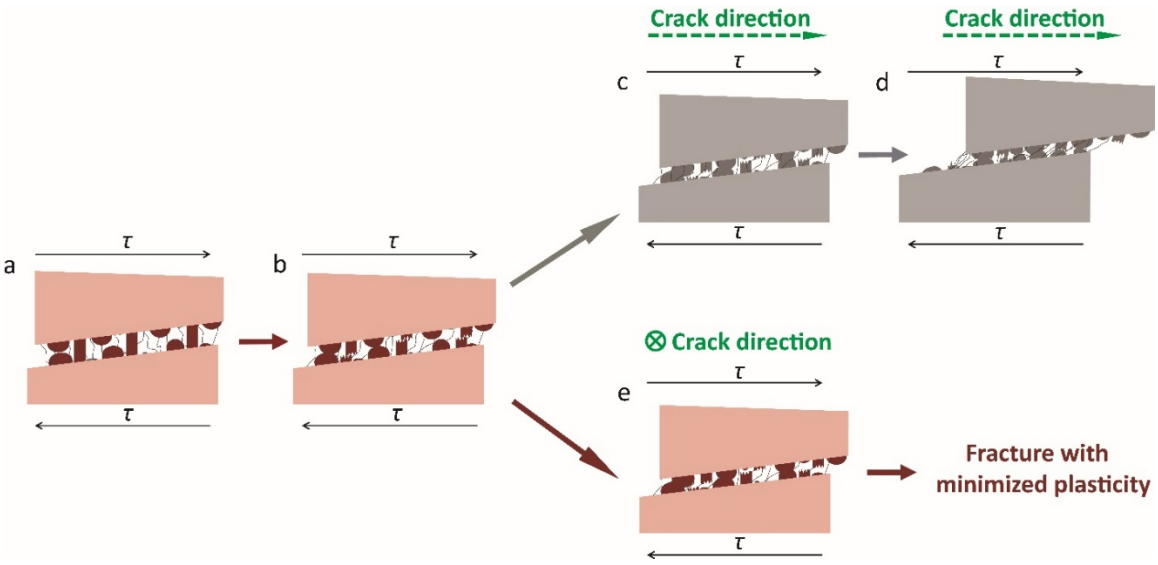

Figure 10: Schematics of the evolution of toughening mechanisms in the nacre deformation. (a) The beginning of tablet sliding. (b) Initial sliding up to the breakage of nanopillars. (c) Decrease in spacing induces more tablet contact. (d) Tablet geometries (waviness, pulling out, etc.) contribute to the shear resistance in the microscale toughening stage. Diagram (e) shows the direction of the crack propagation is perpendicular to tablet sliding under pure shear stresses of torsion, in which (c) and (d) are not fully triggered.

In summary, by applying pure shear stresses of torsion, we exhibit the linear response in the initial sliding stage of nacreous tablets. Mathematical modeling shows that nanopillars contribute dominantly to the shear resistance, while nanoasperity contact and protein chains contribute limitedly in this stage. Complete brittle fracture observed between tablet interfaces in torsion is convincing proof that microscale toughening mechanisms are not triggered to promote ductile behavior of nacreous structures. These findings open an exciting perspective into studying mechanical properties of natural and artificial layered materials using pure shear stresses of torsion. Future effort could also be extended to study the interactions between nanoparticles that build the nacreous tablets, such as rotations, orders, protein strengthening, and deformation twinning.

2.2 Materials and methods

Sample preparation. A red abalone shell with a maximum length of ~210 mm (The Shell shop, CA, US) was obtained to prepare specimens for mechanical tests. The shell was first shaped to 7.6 mm by 7.6 mm cubes, and epoxy ends (Loctite Fixmaster, Rocky Hill, CT) were bonded to increase the gripping area. Using a modified minilathe G8688 (Grizzly Industrial Inc., WA, US) with the high precision control, dry composite dog-bone shaped specimens were created by tuning the cylindrical axis perpendicular to the tablet layers. The gauge sections had diameters of ~3.0 mm and lengths of ~3.0 mm. Then, sample surfaces were smoothed using 400 to 1200 grit sandpapers (3M Company, Maplewood, Minnesota). A total of five specimens were created using pure nacreous gauge sections that are devoid of growth lines. A similar procedure was followed to create single-crystal aragonite specimens (Gold Nugget Miner online) with diameters of ~3.4 mm and gauge section lengths of ~3.4 mm.

Torsional tests. Monotonic torsional tests were performed to study the fracture of nacre specimens using an eXpert 8600 Series axial-torsion testing systems (ADMET, Norwood, MA). Displacement control was used to apply the torque at the rate of 90 degrees per minute with a pre-load of ~0.023 Nm, during which quasi-static loading was assumed. Fixtures with four-independent jaws were created to clamp the specimens. A constant tension of ~0.22 N was maintained during the torsional test. The resulting tensile stress was ~35 kPa, which was far below the tensile strength of nacreous tablets[4]. A dual-system was created to detail the torque-rotation curves using two load cells and two data acquisition systems. A small torsional load cell with a maximum torque of 2.82 Nm (Futek,

Irvine, CA) was mounted on top of a big axial-torsion load cell (ADMET, Norwood, MA) with a maximum torque of 56.5 Nm and a maximum axial load of 4.45 kN. Signals from the big load cell were collected at 50 samples per second using the MtestQuatro's system (Admet, Norwood, MA); while signals from the small load cell were collected via a 14-bit U2531A data acquisition unit (Keysight Technologies, Santa Rosa, CA) at 200,000 samples per second. Calibration of the dual system ranged from 0.0025 to 1.24 Nm. The resulting R^2 value of the linear fitting is 1.0. The twisting angle of the gauge section was measured by subtracting twisting angles of the small load cell and the tapered sections between the clamp end and gauge section from the total rotation recorded. By applying the same series of torque ranging from 0 to 2.25 Nm, twisting angles in the elastic range of an aluminum sample with a 12.7 mm-diameter gauge section were measured using only the big load cell or the two load cells, respectively. The rotation differences were used to establish the torque-rotation relation of the small load cell. Finite element analysis was performed to obtain the torque-rotation relation of the tapered segments. The results show that the twisting angle of the gauge section is ~92% of the total rotation measured.

Fractographic characterization. Different microscopes were used to characterize fractural surfaces of nacre specimens, including optical, scanning electron and microCT techniques. The optical imaging was conducted using an Aven 26700-300 digital microscope (Aven, Ann Arbor, MI) with the built-in white LED light source. For scanning electron imaging, fractured samples were sputter-coated with gold/palladium film without polishing the surfaces. The coated samples were then examined using JEOL 6060 Scanning Electron Microscope (JEOL USA, Peabody, MA) at the beam voltage of ~20 kV. To

compare nacre and aragonite specimens, microCT analysis was performed to scan aragonite samples with the resolution of 6.3 μm at 60 kV and 110 μA for ~6 hours using the Skycan 1173 Xray microtomographer (Microphotonic Inc., Allentown, PA).

Finite element simulation. Three-dimensional finite element models were created using the ABAQUS software (Simulia, Providence, RI) to simulate the initial sliding between two adjacent tablets on the circumference of the gauge section. Different mechanisms, including mineral bridges, nanoasperities, and organic components, are activated simultaneously in the models. Aragonite tablets were modeled as hexagonal disks with edge lengths of 6 μm and the thickness of 500 nm. The vertical spacing in between was 30 nm. Organic matrices were modeled as cylinders with diameters of ~368 nm, and the total area of matrices occupied 5% of the hexagonal area. Similarly, nanopillars were modeled as cylinders with diameters of 50 nm between tablets. Asperities were modeled as half spheres with diameters of 50 nm and heights of 17.5 nm. Thus, the asperity-asperity inception height was 5 nm, and a normal frictionless contact was assumed for the asperity interaction. When nacre grows, nanopillars extrude between proteins to connect the top and bottom tablets [32,99]. Thus, the contact of nanoasperities was not prevalent before tablets slide. In the models, a maximum of 100 nanoasperities could be placed between two parallel hexagonal edges, 50% of which were assumed to contact their mates on the other tablet. Finite element results show that contact stress between asperities is ~14 GPa when the inception height is 5 nm, i.e., close to the theoretical strength of aragonite (E/10 to E/5, i.e., 10 to 20 GPa) [105]. If the inception height was greater than 5nm, asperities were assumed to break and were treated as nanopillars. All materials were assumed isotropic,

linear and elastic based on the stress-strain curves (Fig. 7a). The models were meshed using 2 to 4 million tetrahedral elements. The elastic modulus for organic matrices was 20 MPa [49]. The elastic moduli for aragonite tablets, nanopillars and nanoasperities were the same, ranging from 80 to 100 GPa [50,72]. The Poisson's ratios were 0.4 for organic matrices [44] and 0.3 for aragonite [41]. The bottom tablet was fixed, while the top tablet was constrained except for the sliding and pressure directions. Based on the habitat depths of red abalone [106], i.e., 3.0–4.5 m and 7.0–10.0 m, residual stresses induced by hydrostatic conditions were assumed ranging from 0, -35 and -70 kPa. When these pressures were superimposed with the tensile stress in experiments (35 kPa), the total stresses applied on tablets were 35, 0 and -35 kPa.

Chapter 3: The Role of Water in the Initial Sliding of Nacreous Tablets

In this work we elucidate how water affects the nanoscale interfaces between nacreous tablets compared to that of the dry nacre during the initial sliding. We also provide an experimental evidence of how nanoasperities interact with each other dynamically and how different nanoscale toughening mechanisms evolve as the nacreous tablets slide are scarce.

One primary challenge to explicitly display the evolution of nanoscale toughening mechanisms between nacreous tablets is to isolate the sliding of two adjacent tablets from the rest of the brick-and-mortar structure. The discretizational nature of torsion [107-109] could reveal the behavior of two nacreous tablets in the initial nanoscale sliding. In torsion, two-dimensional planes of pure shear stresses are stacked along the longitudinal axis. If nacre is treated as transversely isotropic, the shear stress distribution along the radius is linear before the specimen fails (See Supplementary Materials, Fig. S1). Due to the differences between nacreous tablets and the nanogaps (~30 nm) in between [13,32], the mismatch of shear stresses causes nacre to fail through the tablet interfaces. Because the polar moment of inertia decreases substantially once the interface between the surface tablets fail, the stress gradients along the radius fail the inside tablet interfaces rapidly. The shear stress and strain in torsion are described by

$$\tau = \frac{T \cdot \rho}{J}$$

(3)

$$s_m = \Delta\theta \cdot r = \gamma_m \cdot l$$

(4)

Where τ is the shear stress on the horizontal plane of the gauge section, T is the torque, r is the gauge section radius, ρ is the distance between an arbitrary point on the cross section to the center varying from 0 to r, $J=0.5\pi r^4$ is the polar moment of inertia, γ_m is the surface shear strain, s_m, $\Delta\theta$, and l are the surface sliding distance, twisting angle, and the height of adjacent tablets, respectively. The surface sliding distance upon failure is measured as the rotational distance between two adjacent tablets on the cylindrical surface. The surface shear strain is the angle between the sliding distance and the height of adjacent tablets. The primary goal of this work is to elucidate how hydrated nacre exhibits different mechanical behaviors from dry nacre in the initial sliding by tuning the nanoscale toughening mechanisms. We do not further distinguish the roles of different types of water in hydrated nacre. We performed fractural experiments under torsion with high temporal resolution measurements, and used pure stresses to detail the microstructural interactions between nacreous tablets during the initial sliding. We discussed these findings with finite element simulations and statistical analyses of the minute structural variations at nanoscale.

3.1 Materials and methods

3.1.1 Materials

Two red abalone shells with the diameters of ~210 mm and ~160 mm (The Shell shop, CA, US) were obtained to prepare the dry and hydrated nacre specimens, respectively. Hydrated nacre samples were submerged in distilled water for four weeks before testing. Both dry and hydrated nacre samples have pure nacreous gauge sections that are devoid of growth lines [32].

3.1.2 Specimen preparations

Dog-bone shaped specimens with diameters of 2.6 ± 0.2 mm and gauge section lengths of 2.4 ± 0.0 mm were prepared by aligning the cylindrical axes perpendicular to the polygonal surfaces of nacreous tablets (Fig. 11b). The shells were first cut to cubes with lengths of ~7.6 mm. Epoxy segments (Loctite Fixmaster, Rocky Hill, CT) were then added to cube ends to increase the gripping areas. Using a modified lathe, the gauge sections of dog-bone specimens were machined with transition areas. Sample surfaces were polished using 400 to 7000 grit sandpapers (3M Company, Maplewood, Minnesota). Due to the scarce of pure nacre sections, a total of six dry nacre specimens and three hydrated nacre specimens were created. The match between the discretizational feature of torsion and the microstructure of nacre enables a detailed illustration of the nanoscale interfacial behavior between nacreous tablets using relatively large specimens.

3.1.3 High temporal resolution experimental systems

An experimental system was created by coupling two load cells to collect the torque-rotation curves at ultrahigh sampling rates (Fig. S1). A small torsional load cell was mounted on top of a large axial-torsional load cell with a maximum torque of 56.5 Nm and a maximum axial load of 4.5 kN (Admet, Norwood, MA). Two types of small load cells were used, i.e. a 2.8 Nm load cell (Futek, Irvine, CA) and a 1.0 Nm load cell (Kistler, Winterthur, Switzerland). Torques from the large load cell were collected at 50 points per second using MtestQuatro (Admet, Norwood, MA), whereas torques from the small load cell were collected at 200,000 points per second using the U2531A data acquisition unit (Keysight Technologies, Santa Rosa, CA). The ultrahigh sampling rate used for the small load cell can record the tiny stress variations caused by the microstructural interactions. The integrated system was well calibrated, of which the linear fitting values (R^2) were 1.0 for the torque ranging from 0.0025 to 1.0 Nm. The rotation of the gauge section was calculated by subtracting rotations from the transition segments and the small load cell from the total rotation measured (Equations S1 and S2). Results show that the rotation of the gauge section is ~92% of the total rotation measured. Due to the laminated microstructure of nacre, the rotation of the gauge section is discretized to obtain the rotation of two adjacent surface tablets along the longitudinal axis, which was used to calculate the nanoscale sliding distance between them. Special fixtures with four-independent jaws were created to load the dog-bone specimens successfully, in which samples were securely held by two pairs of orthogonal surfaces. Each jaw moves freely to make sure that samples are centered along with the loading axis. To fully disclose the interfacial behavior between

nacreous tablets, quasi-static, monotonic, torsional tests were performed to fail dry and hydrated specimens at the displacement rate of 90 degrees per minute. A pre-torque of ~0.023 Nm was applied in the torsional test, and a constant tensile force of ~0.22 N was applied during the test. The resulting tensile stress was ~35 kPa that was far below the tensile strength across nacre tablets [32]. In total, five dry nacre tests were tested using the Futek small load cell. One dry and three hydrated nacre tests were tested using the Kistler small load cell. Consistent results were obtained between different load cells.

3.1.4 Microscopic characterization

Scanning electron microscopes were used to characterize the fractural surfaces of dry and hydrated nacre specimens. Fractured samples were sputter-coated with gold/palladium film without polishing the surfaces. The coated samples were examined using JEOL 6060 Scanning Electron Microscope (JEOL USA, Peabody, MA) at the beam voltages of ~20 kV.

3.1.5 Wiener filtering

Wiener filter [110,111] was used to reduce the noise at high frequency of stress-strain curves collected at 200,000 points per second. The filter minimizes the differences between the observed and the true signals by eliminating the noise in the frequency domain (Equation S3) [110].

3.2 Results and discussion

The surface shear stress-strain curves for dry and hydrated nacre specimens under monotonic torsional tests are shown in Fig. 11. Because the data from the small load cell was collected at 200k points per second, corresponding stress-strain curves were capable of recording the minute variations in the microstructure. In the dry nacre, the stress-strain curve has an increase stage and a sharp decrease stage (Fig. 11a). The R^2 values of the increase segments are above 0.99 for all six dry specimens, meaning that the failures occurred almost at the end of the linear stage (Fig. 11c). It is shown that no large stress variations at high frequencies were found in the increase stage of dry specimens (Fig. 11a), proving that the nacreous microstructures deformed evenly with limited fluctuations during the quasi-static loading process. The shear strength of the dry specimens is 45.2 ± 16.0 MPa at 2.0 ± 0.8% strain. By discretizing the rotation of the entire gauge section into angles between adjacent nacreous tablets, the sliding distance calculated between two dry nacreous tablets upon failure is ~21.3 ± 8.1 nm. However, very different stress-strain curves under monotonic torsion were acquired for the hydrated nacre specimens (Fig. 11e). Three different segments are included, i.e., a linear increase, a transition stage, and a strain-hardening stage with intermittent bumps. The high sampling rate data clearly demonstrated stress variations during the extended bumpy stage (Fig. 11e), whereas no similar variations were detected for the increase and decrease segments (Fig. 11f). The bump height ($\Delta\tau$) and bump distance (ΔS) are defined accordingly for further analysis in the later section. Similarly, R^2 values of the linear segments in the three hydrated specimens are all above 0.99 (Fig. 11c). The yielding shear strength of the hydrated nacre is 39.0 ± 4.0 MPa at 3.8

± 0.67% strain, and the ultimate shear strength is 54.8 ± 6.5 MPa at 12.7 ± 2.0% strain. The maximum sliding distance of the hydrated nacre upon failure is 130.2 ± 20.8 nm (Fig. 11d). For both dry and hydrated specimens, variations of strengths and failure strains were correlated to the specimen locations in the red abalone shells. Catastrophic failures occurred for both dry and hydrated nacre specimens in the end. The tests of dry nacre lasted 1.3 ± 0.4 seconds, whereas the tests of hydrated nacre lasted 9.1 ± 1.4 seconds. These results demonstrated that different nanoscale toughening mechanisms were activated between nacreous tablets to resist the initial sliding in dry and hydrated conditions, respectively.

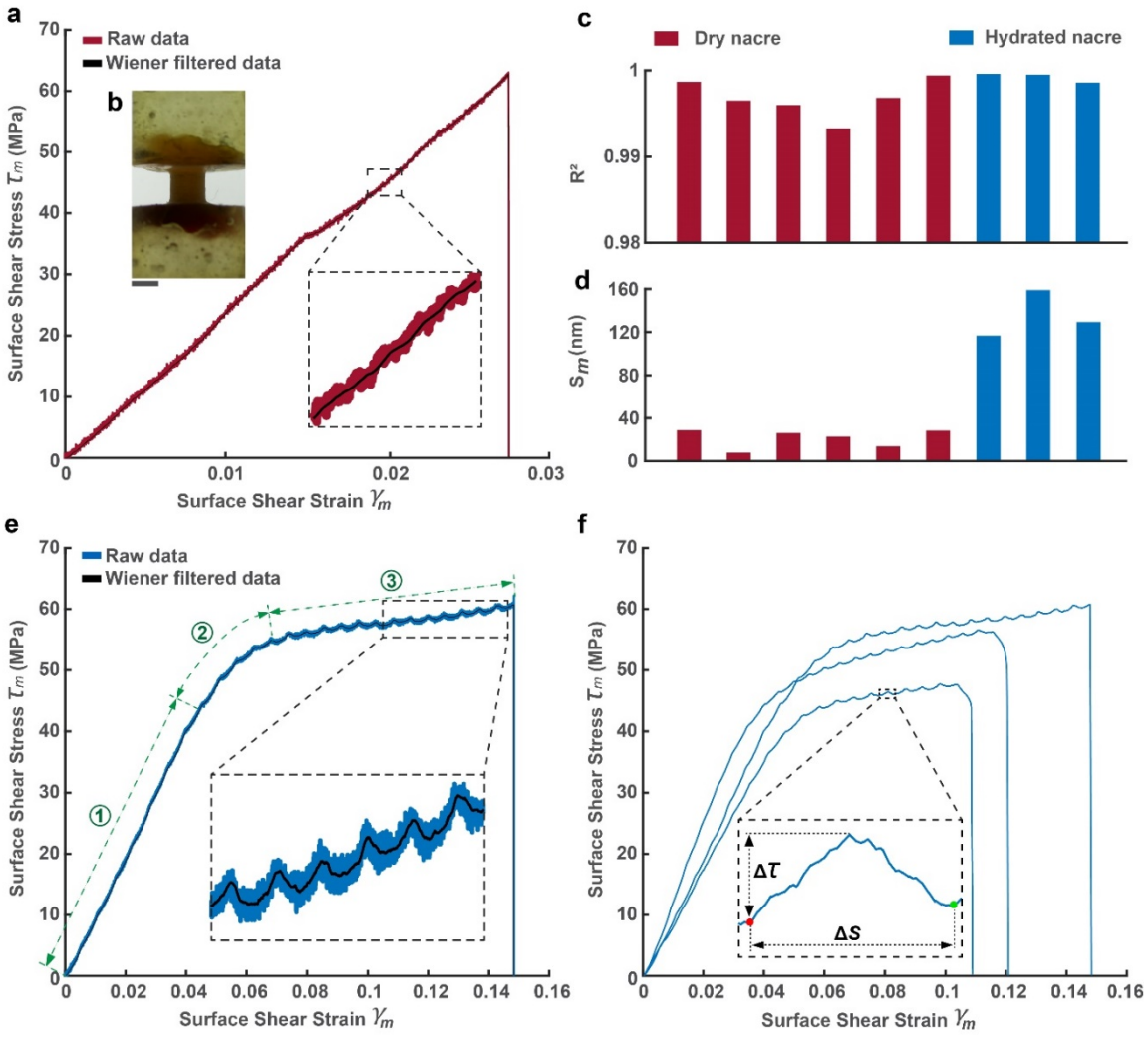

Figure 11: (a) A representative shear stress-strain curve of the dry nacre specimen collected at 200,000 data points per second, in which the wiener filtered curve is overlapped with the raw data. (b) An optical image of a representative dry nacre specimen, where the bright areas at both ends are epoxy and the middle dark area is nacre; the scale bar is 2 mm. (c) R^2 values of the increase segments in dry nacre and the stage 1 segments in hydrated nacre. (d) Surface sliding distances S_m in dry and hydrated nacre specimens. (e) A representative shear stress-strain curve of the hydrated nacre specimens includes a linear stage 1, a transition stage 2 and a bumpy stage 3 before the sudden drop of the shear stress. (f) Three filtered stress-strain curves of the hydrated nacre are illustrated. The red and green dots are the starting and ending points of a bump, respectively, in which the bump height ($\Delta\tau$) and bump distance (ΔS) are defined accordingly. $\Delta\tau$ is the maximum stress difference within the bump, whereas ΔS is the sliding distance between the starting and ending points.

The dry and hydrated specimens exhibited very different fractural surfaces. For the dry nacre specimens, a flat fractural surface was found over the entire cross section (2.6 mm in diameter) of the gauge section (Fig. 12a). A small plateau was observed on the surface, which formed probably because cracks kinked from one nacreous interface to another when the pure shear stress condition was no longer maintained. The closer view (Fig. 12b) showed that separated nacreous tablets with intermittent spiral connections transited from one tablet to the next. The detail view (Fig. 12c) clearly demonstrated the sharp edges of broken tablets in the dry nacre, denoting that the nacreous tablets and their connections were removed rapidly by shear stresses during the crack propagation. In contrast, fractural surfaces of the hydrated nacre were rougher than those of the dry nacre. Instead of cutting through the entire cross section, a spiral fractural surface occurred along the longitudinal axis of the hydrated nacre with several smooth plateaus interspaced by tablet stairs (Fig. 12d, 12e). Near the surface, flat tablet surfaces appeared since the maximum shear stress cut through the interfaces of the external nacreous tablets (Fig. 12f, 12g). Crack growth on the cylindrical surface outlined the spiral edge of the fractural surface (Fig. 12d). As the fracture proceeded, the pure shear stress conditions were no longer maintained over the cross section. Hence, combined shear and normal stresses diverted the cracks from one layer to the other, exposing the tablet stairs step by step (Fig. 12h). The convergence of cracks eventually created a ragged cliff of nacreous tablets (Fig. 12i) that concluded the failure of the hydrated nacre. The power of pure shear stresses in torsion was clearly demonstrated by the streamlines on the fractural surfaces of the hydrated nacre (Fig. 12e). In this work, we tested large specimens (in mm) to obtain stress-

strain curves of the nanoscale interface between nacreous tablets. Although the exact position of the first failed tablet pair was undetermined, we knew that pair was the weakest at the cylindrical surface where maximum shear stress occurred before failure. Once the weakest interface failed, the entire nacreous specimen failed immediately due to the large stress gradient across the radius. Thus, even though SEM images of different fractural surfaces were acquired at microscale, they were the direct results from the distinguished nanoscale toughening mechanisms at the nacreous tablet interfaces on the cylindrical surface. Further understanding on how nanoscale toughening mechanisms in dry and hydrated nacre evolved relied on interpreting the increase segments of the detailed stress-strain curves.

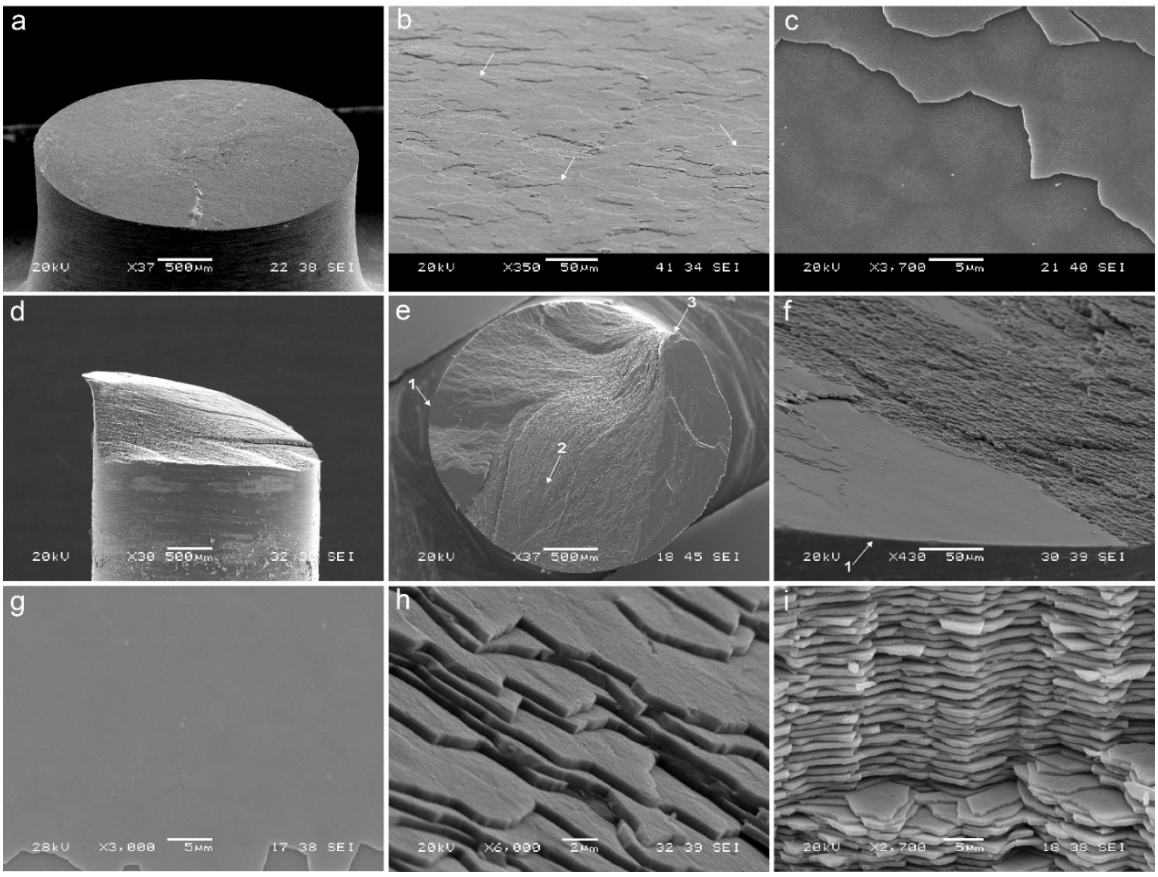

Figure 12: SEM images of the fractural surfaces of dry (a, b, c) and hydrated nacre specimens (d, e, f, g, h, i) under pure shear stresses of torsion. (*a*) An overview of the flat fractural surface of a dry nacre specimen. (b) A closer view of the separated nacreous tablets, in which details of spiral connections between nacreous tables are shown in Figure S5 and Alghamdi et al 2017. (c) A detail view of the broken tablets in dry nacre. (d) The side and (e) top views of the spiral fractural surfaces of a hydrated nacre specimen. Arrows point to different morphologies of the exposed nacreous tablets after fracture. (f) The transition from a flat tablet surface at the external edge to tablet stairs. (g) The flat tablet surface pointed by arrow 1, (h) the ramped tablet stairs pointed by arrow 2, and (i) the staggered tablet cliff pointed by arrow 3 are all observed on the fractural surfaces of the hydrated nacre.

The increase segments in stress-strain curves of the dry nacre specimens are linear, based on which the interactions of mineral bridges, nanoasperities and organic matrices were elucidated via modeling. Three-dimensional finite element models were created using ABAQUS (Simulia, Providence, RI) to simulate two aragonite tablets sliding over each other (Fig. 13a). Homogenous, isotropic, and linear elastic materials were assumed for different features, i.e., aragonite tablets, mineral bridges and nanoasperities (E=100 GPa, v=0.3) [63,72], as well as organic matrices (E=20 MPa, v=0.4) [44,49]. Aragonite tablets were modeled as hexagonal disks with edge lengths of 3 μm and thicknesses of 500 nm. The vertical distance between adjacent tablets was 30 nm. The mineral bridges were modeled as cylinders with diameters of 50 nm and heights of 30 nm connecting the two adjacent tablets. The nanoasperities were modeled as spherical domes with diameters of 50 nm and heights of 17.5 nm. Thus, the inception distance between a pair of top and bottom domes was 5 nm. This contact distance was selected because the contact stress (Fig. S2b) was close to the theoretical strength of aragonite (E/10~E/5=10~20 GPa) [105]. Nanoasperities with larger inception distances were assumed to break during the contact, and thus treated as mineral bridges. Nanoasperities were assumed aligned side by side across the tablets, and only 50% of them contacted their mates on the other half. Thus, a total of 50 nanoasperity pairs contacted each other during sliding. The organic matrices were modeled as cylinders with diameters of ~368 nm filled between adjacent tablets. The total surface area of organic matrices covered 5% of the hexagonal surface of one tablet. Each model was meshed using ~10 million tetrahedral elements. The bottom tablet was fixed, whereas the top tablet was constrained except for the sliding direction. No pressure

was applied over the tablet surface. Before loading, mineral bridges and organic matrices were undeformed, and nanoasperities were adjacent to their mates without contact. Upon sliding, the mineral bridges, nanoasperities and organic matrices worked together to resist the shearing. Monotonic sliding was applied to the top tablet until a total displacement of 20 nm was achieved, corresponding to the average sliding distance in the experimental measurements (Fig. 11d). A displacement step of 2 nm was selected in the quasi-static loading.

In general, stress concentrations occurred at locations of mineral bridges and nanoasperities (Fig. 13a). Because mineral bridges and nacreous tablets were substantially different in size but similar in moduli, stress concentrations occurred within the mineral bridges and degraded quickly inside the tablet. (Fig. S2c). Similar trends existed between organic matrices and nacreous tables (Fig. S2e). However, because the large differences of moduli between mineral bridges and organic matrices, the shear stresses in the mineral bridges (on the order of GPa) were much larger than those in the organic matrices (on the order of MPa). For nanoasperities, the contact area was flattened due to the compression between the asperity pair. High stress concentrations within the asperities (on the order of GPa) occurred symmetrically on both sides of the contact areas, and degraded quickly in the nacreous tablets (Fig. S2d). By tuning the number of different nanoscale features, the lower bound, upper bound and the average shear-stress strain curves were modeled accordingly (Fig. S2a). Results showed that the mineral bridge densities varied from 1.4 to 5.6/μm^2, and a bridge density of ~2.5/μm^2 was needed to resist an average surface shear stress of 45 MPa. By decoupling the contributions of individual nanoscale toughening

mechanisms, mineral bridges contributed dominantly (>90%) to the initial shear resistance, whereas nanoasperities and organic matrices contributed limitedly during this stage (Fig. 13b).

Because stress-strain curves of the hydrated nacre exhibited distinctive stages (Fig. 11e), data collected at the high temporal resolution was examined to elucidate the features of each stage. Wiener filter [110,111] was used to remove the noise at high frequencies in the stress-strain curves of hydrated nacre collected at 200,000 points per second. The power spectrum of surface shear stress in the frequency domain exhibits a linear scaling regime ($\sim\omega^{-2}$) up to ~1000 Hz (Fig. S3a), meaning that the collected data was not significantly affected by the noise in this regime. In Fig. 13c, the power spectrums of the raw and filtered data of surface shear stress rates were plotted in the frequency domain. It is shown that the filtered data maintained almost constant up to ~2 Hz before a scaling regime ($\sim\omega^{-2}$) occurred between 2 and 1000 Hz. After that, a large spectrum of noise spanned over the high frequencies. This trend agreed well with predictions from the mean field theory[112,113], proving that the wiener filter removed the noise data at high frequencies effectively. Based on the filtered data (Fig. 11f), statistical analyses were performed to characterize the bumpy stages in stress-strain curves of the hydrated nacre. Each stress bump was isolated from the main stress-strain curve based on the starting and ending points defined in Fig. 11f. Gaussian models well described the distributions of bump heights and bump distances in the hydrated nacre (Fig. S13b, S13c). When all bumps were overlapped with the same starting point (Fig. 13d), a common area covered all bump heights (0-0.8 MPa) and bump distances (0-5 nm). Similarities of the bump shapes were further illustrated

by the normalized curves in Fig. 13e. The increase and decrease segments almost evenly split the bump distances. A narrow band of slopes covered the increase segments of all bumps, whereas the decrease segments ended at various stress levels. These bumps in the stress-strain curves were primarily due to the dynamic interactions of nacreous tablets during initial sliding before the catastrophic failure. Combinations of the linear increase, the transition stage and a slightly elevated bumpy stage constituted the unique stress-strain curves of hydrated nacre during the initial sliding.

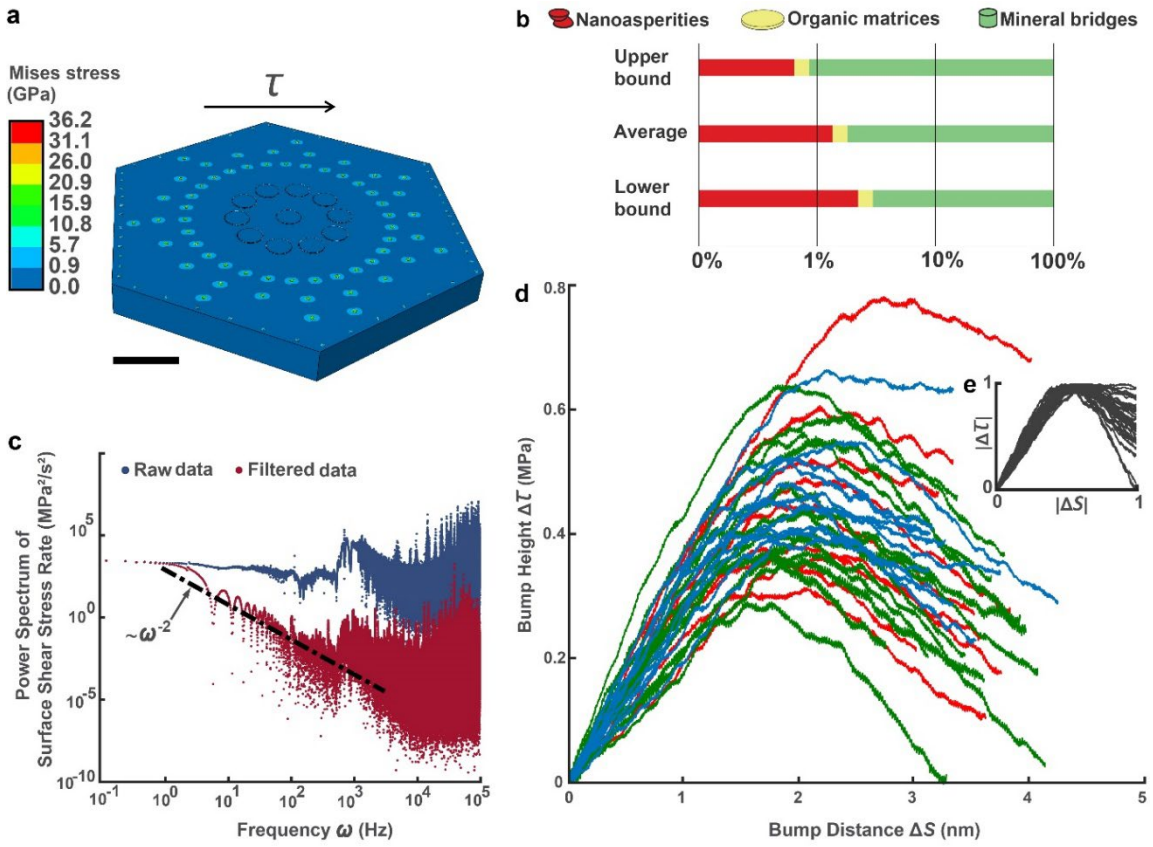

Figure 13: (a) An overview of stress contours on an exposed nacreous tablet surface; The scale bar is 1 μm. (b) Contributions of mineral bridges, nanoasperities and organic matrices

to the initial shear resistance of dry nacre. (c) The power spectrum of surface shear stress rate in the frequency domain (more than 1.5 million data points for each curve) included a scaling regime that is $\sim\omega^{-2}$, agreeing with the predictions from the mean field theory. (d) Overlapped bumps from all hydrated nacre specimens. (e) Normalized bumps with respect to bump heights and bump distances.

Stress-strain curves are fingerprints of microstructural interactions in the specimens during loading. In dry nacre, the shear stresses are resisted by mineral bridges, nanoasperities and organic matrices when the sliding starts (Fig. 14a). The shear-stress strain curve is linear until a sudden drop occurs at the proportional limit (Fig. 14b), during which the shear stress is primarily resisted by mineral bridges (Fig. 13b). In dry nacre, the breakage of multiple mineral bridges happens very quickly at the sliding distance of ~20 nm (Fig. 11d) because the failure of any mineral bridge increases stresses of the unbroken bridges via immediate stress redistributions. Therefore, a gap occurs between nacreous tablets on the cylindrical surface that enables cracks to propagate perpendicularly to the sliding direction due to the large stress gradient across the radius (Fig. 14b, 14c, S1). The microscale toughening mechanisms [2,102,103] are not triggered since there is little chance that nacreous tablets could interact with each other after the mineral bridges break. Thus, the dry nacre fails catastrophically under pure shear stresses of torsion (Fig. 14d).

In hydrated nacre, water changes the story before the catastrophic failure. Hydrogen bonds form between water molecules and the chitin fiber network, between water molecules and different proteins, or within themselves [54,55]. These extra connections stabilize the organic matrices between nacreous tablets [114] and the proteins between nanograins inside the tablets [2,64,115]. In the linear stage (stage 1), mineral bridges, nanoasperities and organic matrices provide the shear resistance (Fig. 14e), in which the

proportional limit occurs ~40 MPa at ~30 nm sliding. The increased sliding distance at the proportional limit compared with that of dry nacre (~20 nm) is probably due to the deformation (rotations and extensions) of nanograins inside nacreous tablets and intergrain proteins [114,116] which enables the extra sliding distance before mineral bridges break (Fig. 14e-14h). Because of water, stress redistributions in hydrated nacre become more complicated than those in dry nacre. For example, interactions between water molecules on tablet surfaces and the more stabilized organic matrices could provide temporal stress redistribution paths in hydrated nacre. When a mineral bridge breaks, it takes longer to redistribute shear stresses to other areas due to these time-dependent interactions. During this process, part of the shear stresses is transferred to the contacted nanoasperities as the tablet spacing decreases (Fig. 14f-14h). The redistribution continues until all mineral bridges break and the contacted nanoasperities take over all the shear resistance (Fig. 14f-14i). However, this unstable state could not last as the sliding continues. Therefore, the bumps in the shear stresses keep occurring as the tablets interact with each other intermittently during this dynamic stage (Fig. 14i, 14j). Once the sliding distance is large enough, the stress gradient enables cracks to propagate radially that eventually fail the hydrated nacre catastrophically (Fig. 14k). We should notice that both dry and hydrated nacre fail catastrophically in the end under pure shear stresses of torsion.

It is interesting to observe the fractural surfaces of dry and hydrated nacre under torsion. The dry nacre exhibited ~0° fractural surfaces with almost no plasticity, whereas the hydrated nacre exhibited ~45° (to the longitudinal axis) spiral fractural surface with extended plasticity. This is opposite to the fracture of isotropic materials under torsion, i.e.,

~0° flat surfaces in ductile materials and ~45° fractural surface in brittle materials. The laminated microstructure of nacre dictates these unusual fracture patterns (Fig. S4). In dry nacre, the crack propagation under torsion is fast enough to confine the fracture almost between adjacent nacreous tablets. However, when the interface of surface tablets failed in hydrated nacre, the retardation of stress distributions resulting from the hydrogen bonds promotes the kinking of cracks to neighbor interfaces due to the principle tensile stresses on the cylindrical surface. The competition between surface cracks and radial cracks leads to the spiral fracture inside the brick-and-mortar structure of hydrated nacre within a very short amount of time.

Usually, we test a nanoscale specimen to understand its mechanical behavior. We use the nanoscale geometry to isolate the specimen from other parts of the material. Thus, the specimen sizes and testing systems were strongly dependent on our fabrication capabilities. In this work, we use the intrinsic feature of torsional load to isolate a nanoscale interface from the rest of the material, in which the sliding behavior between nacreous tablets is revealed in a detailed manner. The usage of larger specimens may reduce the disturbance to the nanoscale specimens during fabrication. It could also test nanoscale features in natural materials that may not be easily reproduced through current technology, such as aragonite mineral bridges with diameters of ~50 nm. The proposed method could lead to further insights into the interfacial behavior of a variety of natural and artificial laminated nanomaterials, such as artificial nacres, thin films and batteries [117,118]. The methodology used in this study could be extended to other seashell [119,120] though which further understanding on the mechanical properties of natural materials could be obtained.

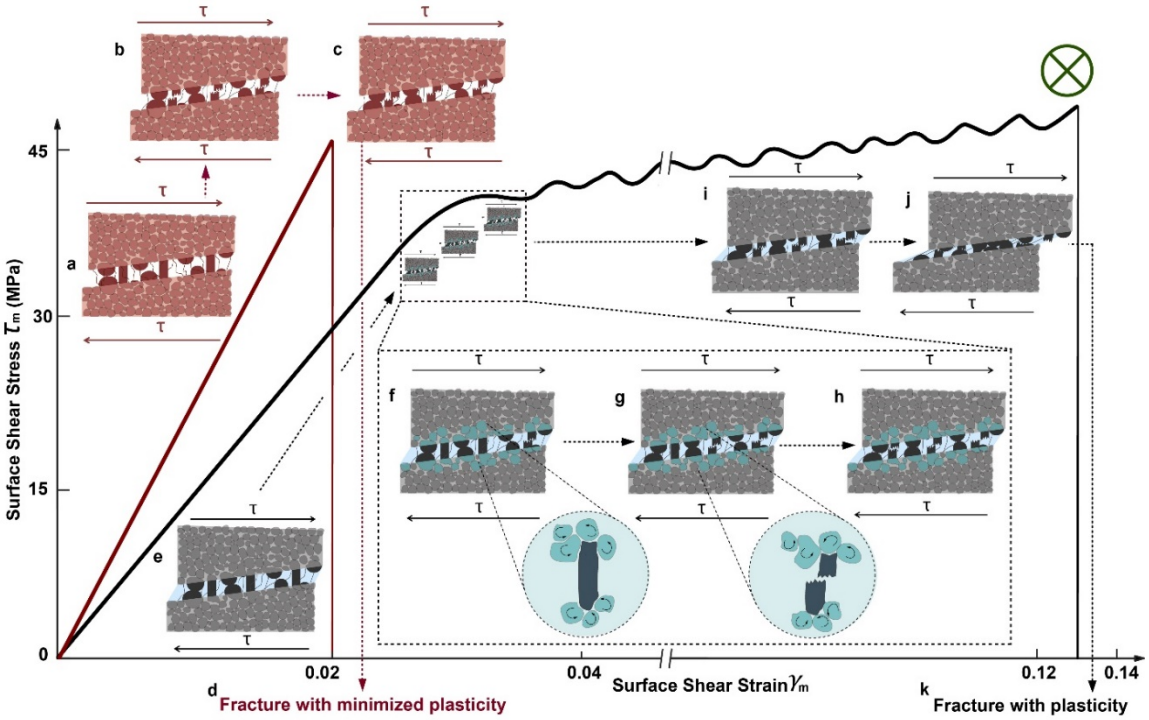

Figure 14: Evolution of nanoscale toughening mechanisms in dry (a-d) and hydrated (e-k) nacre. (a) The initial dry nacre contains intact mineral bridges, nanoasperities and organic matrices. (b) Mineral bridges break at the proportional limit. (c) Decrease in vertical spacing between nacreous tablets, and (d) catastrophic failure with minimized plasticity of the dry nacre. (e) The initial hydrated nacre contains intact mineral bridges, nanoasperities and organic matrices. The blue background denotes water. (f), (g) and (h) show the sequential breakage of mineral bridges in the transition stage ranging from the proportional limit to the beginning of the bumpy stage. The shear stresses are gradually transferred from mineral bridges to the contacted nanoasperities. Rotations and extensions of nanograins inside nacreous tablets and intergrain proteins enable the extra sliding distance before mineral bridges break. (i) Decrease in the vertical spacing between nacreous tablets. (j) The additional sliding induces intermittent interactions between adjacent tablet surfaces. (k) Catastrophic failure with plasticity of hydrated nacre. The circled cross denotes that the crack propagation direction is perpendicular to the sliding direction when catastrophic failures happen.

3.3 Conclusions

We present a study on the fracture of dry and hydrated nacre under pure shear stresses of torsion. In dry nacre, the specimens fail catastrophically at the proportional limit with minimized plasticity. This is because the cracks propagate perpendicularly to the

sliding direction once the mineral bridges break, during which the nacreous tablets have little chance to provide the shear resistance. In hydrated nacre, the deformation of nanograins inside nacreous tablets and intergrain proteins enable the extra sliding before mineral bridges break. The hydrogen bonds between water molecules and organic matrices, or within water molecules enable temporal paths for stress redistributions. The shear stresses are gradually transferred to contacted nanoasperities as mineral bridges break sequentially, after which the subsequent sliding induces intermittent, dynamic interactions between adjacent nacreous tablets. When the sliding is large enough, the large stress gradient propagates cracks radially and fail hydrated nacre catastrophically. Our study demonstrates the evolution of nanoscale toughening mechanisms in dry and hydrated nacre, in which water brings plasticity to the interface between nacreous tablets during the initial sliding. Both dry and hydrated nacre fail catastrophically under pure shear stresses of torsion eventually, during which the microscale toughening mechanisms are not triggered. Experimentally, we isolate a nanoscale interface between tablets from a large nacre specimen (mm in size) using torsion. The ultrahigh sampling rate details the microstructural interactions between nanolayers. This method could bring new insights into the interfacial behavior of various laminated materials.

Chapter 4: Tensile and Shear Behavior of Microscale Growth Layers between Nacre

Despite prior efforts, limited research exists to elucidate how growth layers between bulk nacre respond to shear and tensile stresses by orchestrating their structural components, or how microstructures of dry or hydrated growth layers change under different loadings. Lack of this knowledge may hinder us from further understanding the mechanical behavior of seashells, or creating high performance bioinspired materials and structures.

In this study, we focused on the mechanical behavior of the microscale growth layers between bulk nacreous sections. We used high temporal resolution experiments to study the tensile and shear behavior of these growth layers (Fig. 15). First, we created experimental systems to collect stress-strain curves using ultrahigh sampling rates. Then, we fabricated dog-bone shaped nacre specimens with microscale growth layers in both dry and hydrated conditions. Subsequently, we performed monotonic tension and torsion tests to examine the corresponding behavior of growth layers, in which the failure was detailed by stress evolutions of the high resolution stress-strain curves. After that, fractographic characterization was conducted to illustrate the different fractural patterns of growth layers under tensile and shear stresses. Finally, physical models were proposed to explain the failure of microscale growth layers under different loadings.

4.1 Materials and methods

4.1.1 Sample preparations

Specimens were prepared using nacre with growth layers of three red abalone (*H. Rufescens*) shells with diameters ranging from 160 to 210 mm (The Shell Shop, Inc. CA). The shells were first cut to cubes with lengths of ~7.6 mm. The ends were immersed in epoxy (Loctite Fixmaster, Rocky Hill, CT) to extend the gripping areas. Cylindrical dog-bone shaped specimens were machined with gauge lengths ranging from 2.3 to 3.0 mm for both torsion and tension tests. Detailed dimensions were listed in Table S3 in Supplementary Materials. The final composite specimens include growth layers and pure nacre section, in which the longitudinal axis of the gauge section is perpendicular to the layered growth layers and nacreous tablets. Representative nacre and composite specimens are shown in Fig. 16. The number of growth layers varied between 1 to 5 in composite specimens, most of which included one growth layer in the gauge section. Angles of the growth layers to the horizontal cross-sectional plane ranged from 0 to 7 degrees. Hydrated growth layer and pure nacre specimens were acquired by submerging the dry specimens in distilled water for four weeks before testing them out of water. At least three replicas were tested for each condition, including dry composite specimens under torsion, hydrated composite specimens under torsion, dry composite specimens under tension, and hydrated composite specimens under tension. As a comparison, cylindrical specimens created using nacre that were devoid of growth layers, i.e., pure nacre specimens, were tested in torsion. To test pure nacre specimen under tension, flat dog-bone shaped specimens were created because the epoxy ends were defective in tension sometimes. Flat surfaces of the transition areas ensured good contact between specimens and fixtures during the tension tests.

Dimensions of all samples studied in this work are tabulated in the supplemental document (See Table S3 in Supplementary Materials)

4.1.2 High temporal resolution torsional tests

One primary challenge to investigate the mechanical behavior of growth layers is to isolate their performance from that of pure nacre. The preparation of nano- or micro-scale specimens may introduce extra disturbance to the highly packed layered structures. We use relatively large specimens (mm in size) to measure the shear resistance of growth layers by matching the discretizational feature of torsion [98,108,121-123] with the laminated microstructure of growth layers and nacre. In torsion, two-dimensional planes of pure shear stresses are stacked along the longitudinal axis (Fig. 15). If the composite specimen is deemed transversely isotropic, shear stresses distribute linearly along the radius before failure (τ_b, Fig. 15b). The shear stress in torsion is described by

$$\tau = \frac{T \cdot \rho}{J} \tag{5}$$

Where τ is the shear stress on the horizontal plane of the gauge section, T is the torque, r is the gauge section radius, ρ is the distance between an arbitrary point on the cross section to the center varying from 0 to r, $J=0.5\pi r^4$ is the polar moment of inertia. Because of the mismatch between microstructures of growth layers and pure nacre, shear stresses between nacreous tablets are different from those between growth layers. Once the surface fails, the polar moment of inertia decreases substantially due to the stress gradients along the radius

(τ_a, Fig. 15b), leading to the rapid failure of the specimen. Therefore, the weakest region in the composite will serve as the source of failure (Fig. 15c).

A dual system was created to collect the high temporal torque-rotation curves by assembling two load cells (Fig. 15a). A 1.0 Nm load cell (Kistler, Winterthur, Switzerland) was mounted on top of an axial-torsional load cell with a maximum torque of 56.5 Nm and a maximum axial load of 4.5 kN (Admet, Norwood, MA). Torques from the large load cell were collected at 50 data points per second by MtestQuatro (Admet, Norwood, MA), whereas torques from the small load cell were collected at 200,000 data points per second by the U2531A data acquisition unit (Keysight Technologies, Santa Rosa, CA). The system was calibrated at the torque range between 0.0 and 1.0 Nm, from which a linear fitting value (R^2) of 1.0 was obtained. Surface shear strain was measured by analyzing the high-speed images collected at ~5k frames per second using the microlenses of the Chronos 1.4 camera (Kron Technologies Inc., BC, Canada). Fixtures with four-independent jaws were used to load the dog-bone specimens securely. Quasi-static, monotonic torsional tests were performed to fail the dry and hydrated specimens with the displacement rate of 90 degrees per minute. A pre-torque of ~0.023 Nm was applied, and a constant tensile force of ~0.22 N was applied during the torsional test. The resulting tensile stress of ~35 kPa was far below the tensile strength across pure nacre or growth layers.

4.1.3 High temporal resolution tension tests

The chain idea is also implemented to measure the tensile strength across the laminated growth layers and nacre (Fig. 15d). Under tension, uniform normal stresses stretch the growth layers and pure nacre along the longitudinal axis. Similarly, the weakest

point in the laminated composite initiates the failure (Fig. 15f). The tensile stress is given by:

$$\sigma = \frac{F}{A} \tag{6}$$

Where F is the applied tensile force, and A is the cross-sectional area of the gauge section in the specimen.

The other dual system was created to collect the high temporal load-displacement curves under tension tests (Fig. 15d). A 500 N load cell (Kistler, Winterthur, Switzerland) was mounted on top of the same axial-torsional load cell with a maximum torque of 56.5 Nm and a maximum axial load of 4.5 kN (Admet, Norwood, MA). Tensile forces from the large load cell were collected at 50 data points per second by MtestQuatro (Admet, Norwood, MA), whereas tensile forces from the small load cell were collected at 200,000 data points per second by the U2531A data acquisition unit (Keysight Technologies, Santa Rosa, CA). The system was calibrated at the tension range between 0 and 93.41 N, from which a linear fitting value (R^2) of 1.0 was obtained. Tensile strain was measured at local regions of gauge sections by analyzing high-speed images collected at ~5k frames per second using the microlense of Chronos 1.4 camera (Kron Technologies Inc., BC, Canada). Insert-type fixtures were used to hold dog-bone shaped specimens securely while maintaining good alignment during tension. With a pre-load of ~0.22N, quasi-static,

monotonic tension tests were performed to fail the dry and hydrated specimens with the displacement rate of 1.27 mm per minute.

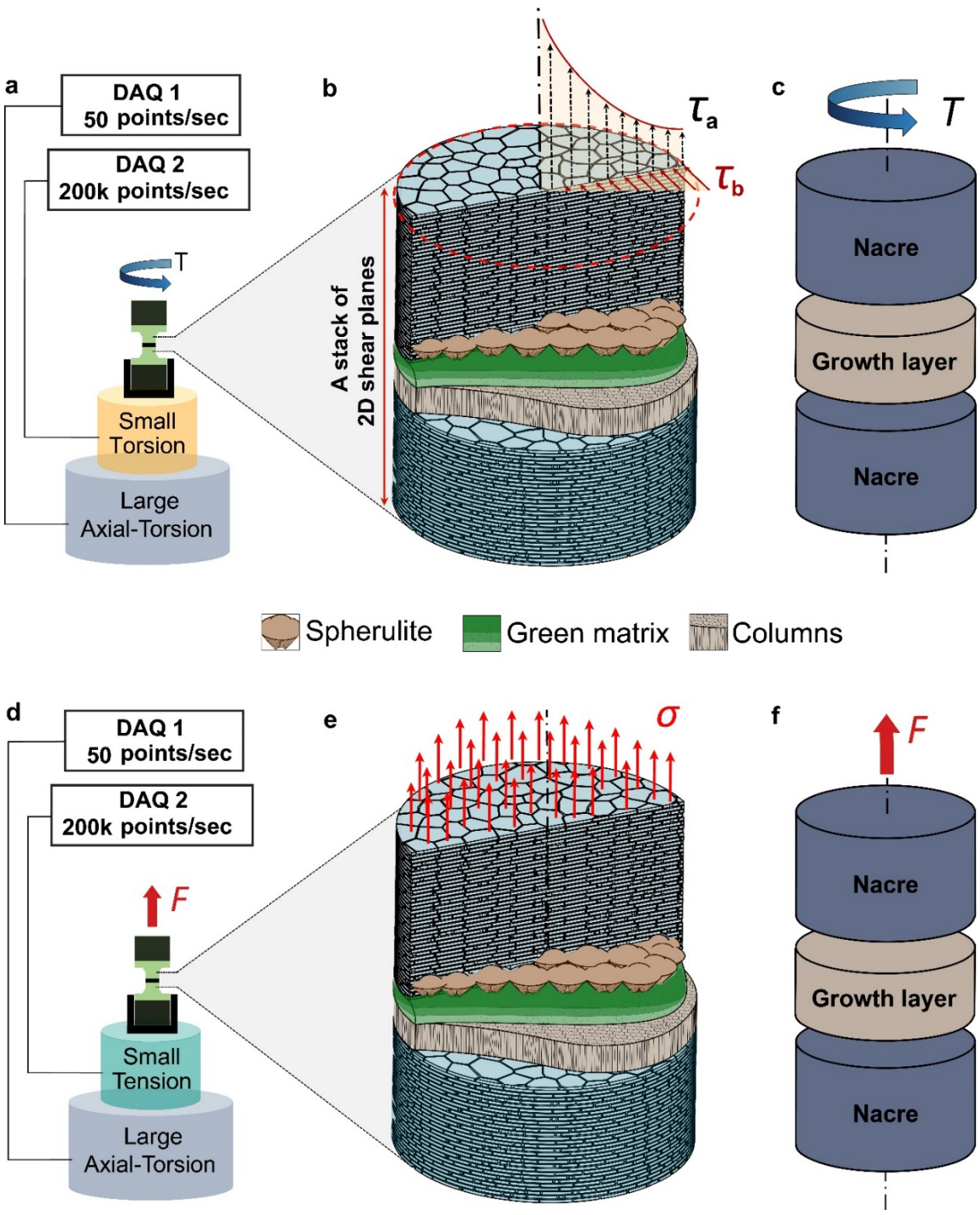

Figure 15: Schematic diagrams of the high temporal resolution experimental setups (a,b,c) Torsion tests. (d,e,f) Tension tests. (a) The dual system used in torsion tests. (b) The model of layered composites is subjected to a stack of two dimensional shear planes in torsion. τb and τa are the shear stress distributions before and after failure. (c) The conceptual model

shows the growth layers and nacre under torsion. (d) The dual system used in tension tests. (e) The model of layered composites is subjected to tensile stresses. (f) The conceptual model shows the growth layers and nacre under tension.

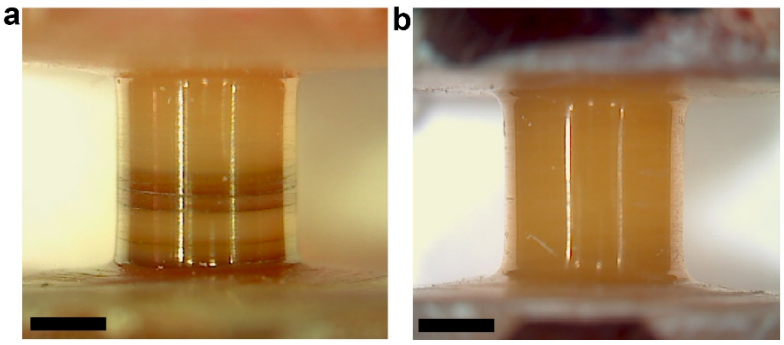

Figure 16: (a) A representative composite specimen includes both growth layers and pure nacre. (b) A representative pure nacre specimen is devoid of growth layers. The scale bars are 1 mm.

4.1.4 High temporal profile data processing

Wiener filter was used to reduce the noise generated at high frequency of the stress-strain curves collected at 200,000 points per second. The filter minimizes the differences between the observed and true signals by eliminating the noise in the frequency domain. The wiener deconvolution is given by:

$$V_T(\omega) = \frac{V_E(\omega)}{H(\omega)} \frac{|S(\omega)|^2}{|S(\omega)|^2 + |N(\omega)|^2}$$

where, $V_T(\omega)$ is the filtered signal, $V_E(\omega)$ is the recorded signal, $H(\omega)$ is the impulse response function of the experimental system, $S(\omega)$ is a theoretical prediction for the true

signal, and $N(\omega)$ is the noise [110,111]. Based on the Wiener filter, the stress-strain curves were processed, through which statistical analyses were performed to illustrate the microstructural evolution collected during torsion and tension tests.

4.1.5 Fractographic characterization

We used the JEOL 6060 scanning electron microscope (JEOL USA, Peabody, MA) to characterize the fractural surfaces of dry and hydrated nacre specimens. Fractured samples were sputter-coated with the gold/palladium film without polishing the surfaces, which were then examined at the beam voltages of ~20 kV. Fractural patterns of dry and hydrated composite specimens were compared at similar resolutions. Meanwhile, fractural patterns of pure nacre specimens were also analyzed and presented.

4.2 Results

4.2.1 Wiener filtered data

We used stress to trace the microstructural evolution during loading because stress probes the minute variations at nano- or micro-scale that may not be easily captured by other means [122,123]. A representative stress-strain curve of a dry composite specimen tested under monotonic tension is shown in Fig. 17b. The power spectrums of the raw and filtered data of surface shear stress rate were plotted in the frequency domain (Fig. 17a). It is shown that the filtered data maintained almost constant up to ~2 Hz before a scaling regime ($\sim\omega^{-2}$) occurred between 2 and 1000 Hz. After that, a large spectrum of noise spanned over the high frequencies. This trend agreed with the theoretical predictions [110,111], confirming that the wiener filter effectively removed the noise data at high

frequencies. Based on the filtered data (Fig. 17b), it shows that intermittent stress variations occurred on the primary stress-strain curve of a dry composite specimen under tension (Fig. 17c). Each stress bump was isolated from the main curve based on the starting and ending points defined in Fig. 17d. These stress variations were detected in the increase stages of composite and nacre specimens under tension in dry and hydrated conditions. However, limited stress variations were detected for composite specimens under torsion in dry and hydrated conditions. Detailed discussions on stress bumps are included in the following sections.

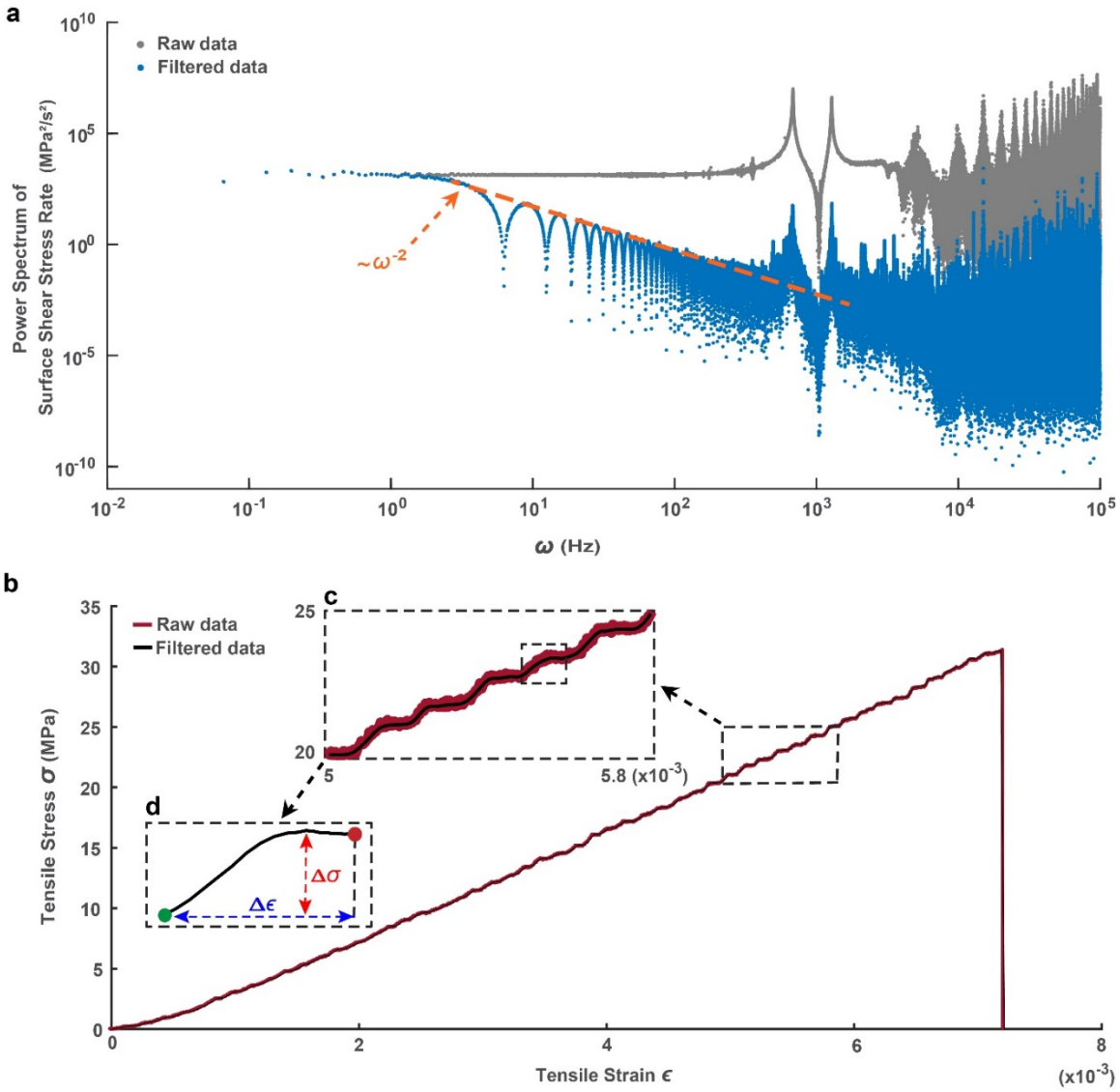

Figure 17: (a) The power spectrum of surface shear stress rate ($d\tau_m/dt$) in the frequency domain included a scaling regime that is $\sim\omega^{-2}$, agreeing with estimations from the theory [110,111]. (b) A representative stress-strain curve of a dry composite specimen under monotonic tension. The green and red dots are the starting and ending points of the stress bump, respectively, in which the bump height ($\Delta\boldsymbol{\sigma}$) and bump distance ($\Delta\varepsilon$) are defined accordingly. $\Delta\boldsymbol{\sigma}$ is the stress difference between the peak and the lowest point within the bump, whereas $\Delta\varepsilon$ is the strain difference between the starting and ending points.

4.2.2 Stress-strain curves of composite and nacre specimens under torsion

Dry and hydrated composite specimens separated into halves under monotonic torsional tests. The dry composite exhibited shear strengths of 37.2 ± 5.4 MPa at 10.9 ± 1.0% shear strain, whereas the hydrated composite exhibited shear strengths of 23.8 ± 3.4 MPa and 21.4 ± 5.0% shear strain at failure. The stress-strain curves of composite specimens include increase and decrease segments (Fig. 18a, Fig. S6). No significant stress variations were observed in the increase stages of dry and hydrated composite specimens. Although both types of specimens split into halves, the decrease segments of hydrated composite specimens were not as straight as those of dry composite specimens, confirming that the presence of water changed the failure pattern. The hydrated composite specimens also exhibited larger shear strain at failure and lower shear strength than the dry ones (Fig. 18b).

Dry pure nacre exhibited shear strengths of 45.2 ± 16.0 MPa at 2.0 ± 0.8% shear strain. Dry pure nacre exhibited a linear increase and a sharp decrease leading to the catastrophic failure of the specimens. No substantial stress variations were observed in the increase segments, confirming that the microstructures of dry nacre deformed evenly with limited fluctuations before the final fracture [122]. The hydrated nacre exhibited a linear increase, a transition stage and a slightly elevated stage with intermittent bumps before the sudden drop [123]. The yielding shear strengths of the hydrated nacre were 39.0 ± 4.0 MPa at 3.8 ± 0.67% shear strain, whereas the ultimate shear strengths were 54.8 ± 6.5 MPa at 12.7 ± 2.0% shear strain. For both dry and hydrated specimens, catastrophic failures occurred at the end of monotonic torsional tests.

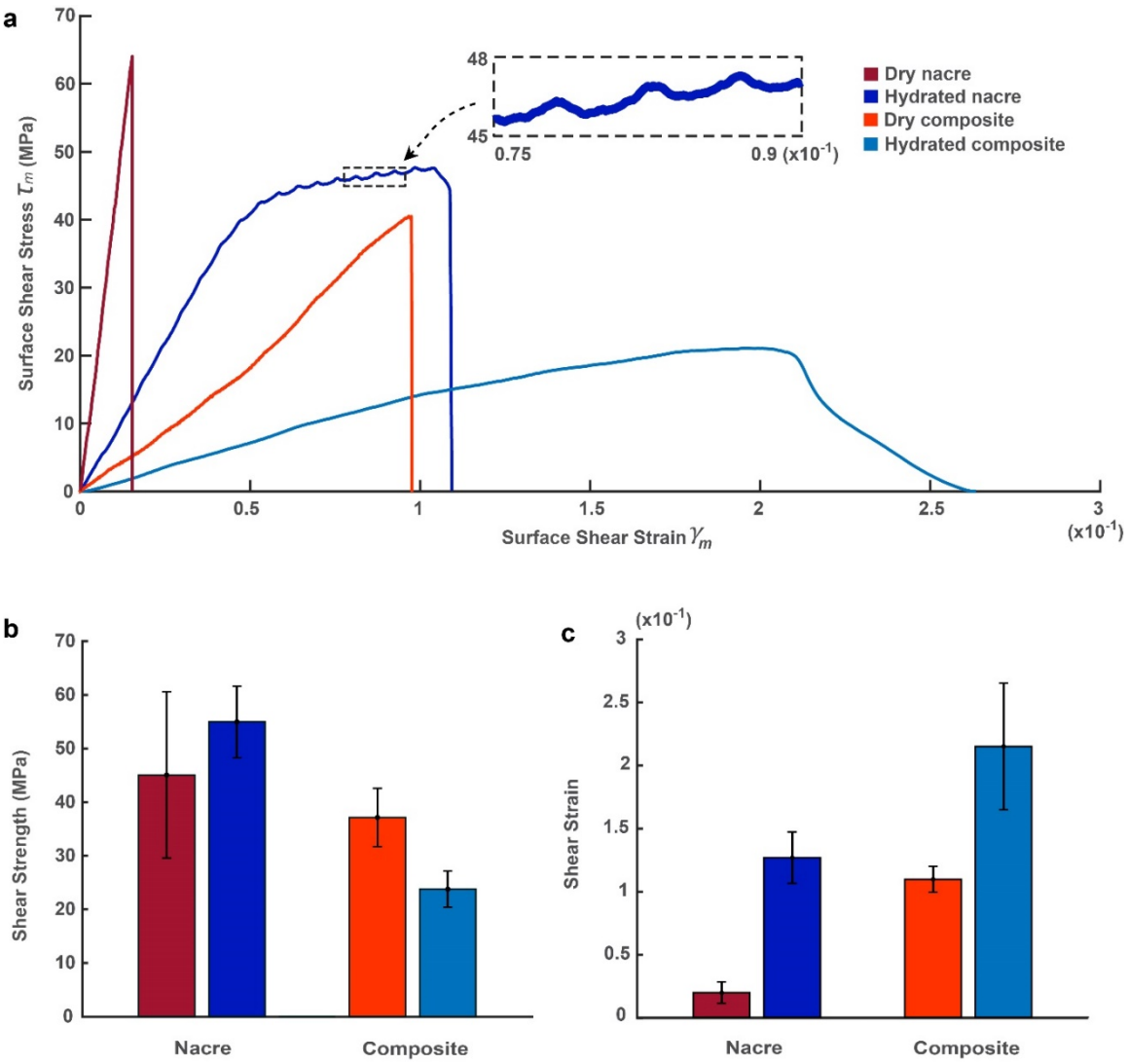

Figure 18: (a) Filtered representative surface shear stress versus surface shear strain curves of dry and hydrated specimens under monotonic torsion tests. Statistical values of (b) shear strength, and (c) shear strain at failure, of composite and nacre specimens, respectively.

4.2.3 Stress-strain curves of composite and nacre specimens under tension

Under monotonic tension tests, the composite and nacre specimens also separated into halves. Dry composite specimens exhibited tensile strengths of 8.4 ± 2.1 MPa at 2.8 ± 0.4% tensile strain, whereas hydrated composite specimens exhibited tensile strengths of

6.0 ± 1.5 MPa at 7.7 ± 1.0 tensile strain. Both dry and hydrated composite specimens included an increase and a sharp decrease (Fig. 19, Fig. S7). In the increase stage, stress variations occurred for both dry and hydrated composite specimens under tension. Hydrated composite specimens exhibited larger tensile strain at failure and lower tensile strength than dry composites.

Dry nacre specimens exhibited tensile strengths of 29.8 ± 3.2 MPa at 0.6 ± 0.1% tensile strain, whereas hydrated nacre specimens exhibited tensile strengths of 22.8 ± 2.3 MPa at 1.4 ± 0.0 tensile strain. Similar to composite specimens under tension, dry and hydrated nacre specimens include a ramped increase and a sharp decrease concluding the failure. Stress variations were also observed in the increase stages of both dry and hydrated nacre specimens. In general, the hydrated nacre exhibited larger tensile strain at failure and lower tensile strength than dry nacre.

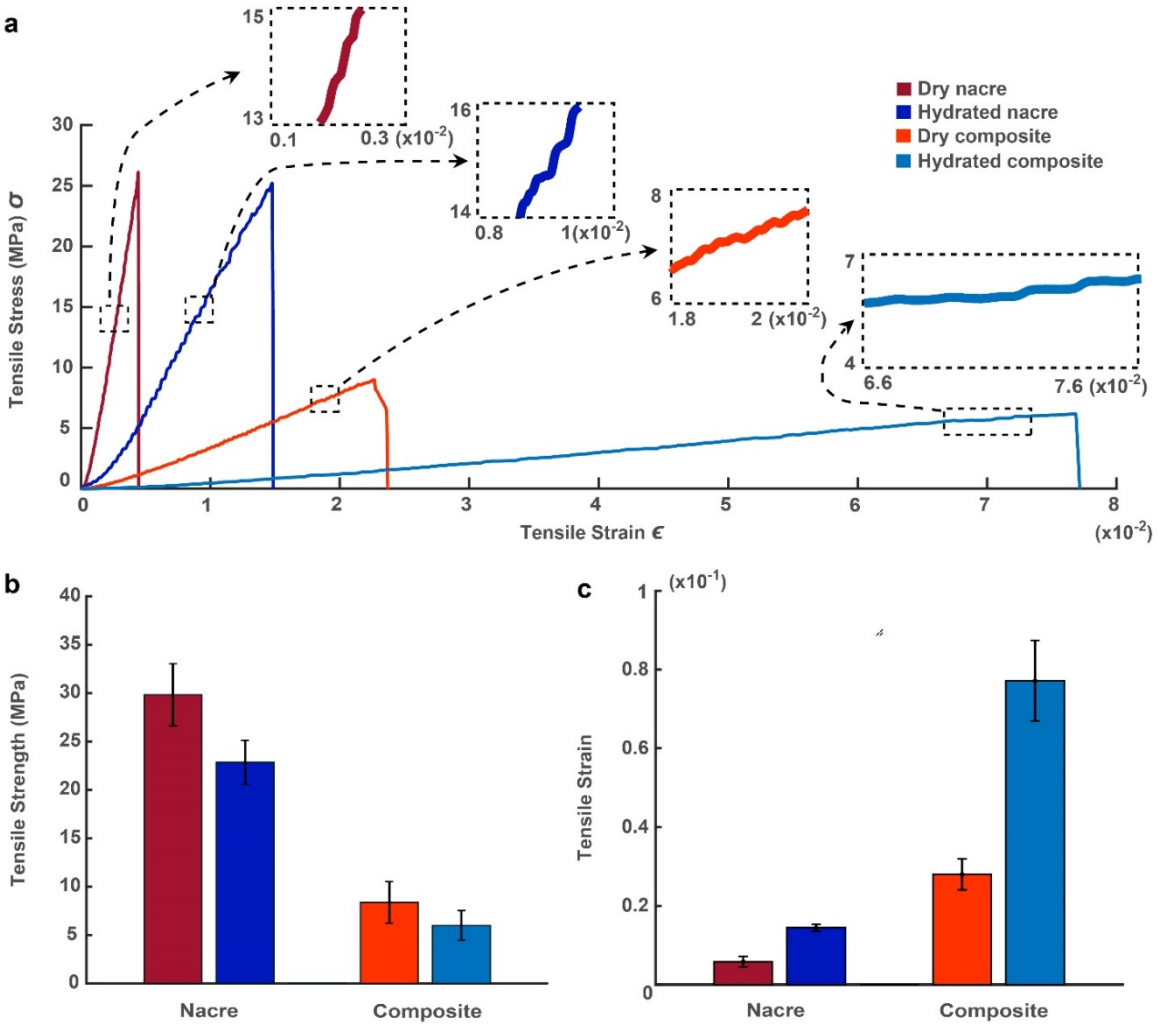

Figure 19: (a) Filtered representative tensile stress-strain curves of dry and hydrated specimens under monotonic tension. Statistical values of (b) tensile strength, and (c) tensile strain at failure, of composite and nacre specimens, respectively.

4.2.4 Fractural surfaces of composite specimens under torsion

Under torsion, both dry and hydrated composite specimens fractured across the cross section of the gauge sections. For dry composite specimens, a small fraction of the fractural surface was covered by growth layers, whereas the rest was covered by pure nacre sections from the circumferential edge to the circular center (Fig. 20a). A stair of nacreous

tablets gradually transited from the pure nacre section to the fractured growth layers (Figs. S8b, S8c and S8d), from which different components were detected, such as the green matrix (Figs. S8c and S8d) and spherulites (Fig. 20c). Most spherulites in dry growth layers were cleaved after fracture, exhibiting broken pieces over the areas. Because cracks propagated very fast once the cylindrical surface failed due to the stress gradient, open spaces inside the spherulitic aragonite were preserved and exposed after the catastrophic fracture.

Hydrated composite specimens exhibited substantially different fractural surfaces than those of dry specimens under torsion. Flipped skins from the broken spherulites pervaded most of the cross section (Fig. 20d). Although the flipped skins varied in sizes, the presence of a dominant flipping direction indicated the fast crack propagation from the outer surface to center (Fig. 20d, Fig. S9b). Detailed views exhibited the sheaths of broken spherulites in hydrated growth layers (Fig. 20f, Fig. S4c), which were very different from the cleaved spherulites in dry growth layers (Fig. 20c). “Open eyes” were formed by crystal clusters at the central bottom of spherulites and the broken conical walls along with the dominant orientation in response to cracks. In contrast to dry composites, limited pure nacre sections were found on the fractural surfaces of hydrated composites under torsion, indicating that hydrated growth layers were more effective in confining cracks within themselves.

It is interesting to examine the fractural surfaces of dry and hydrated nacre specimens under torsion. For dry nacre specimens, flat fractural surfaces covered most of the cross-section except small plateaus that spanned over a few nacreous tablets (Fig.21a,

Fig. S10b). This is because cracks propagated very quickly when the catastrophic failure happened [122]. For hydrated nacre specimens, spiral fractural surfaces occurred at ~36° to the longitudinal axis across the gauge section (Fig. 21c). Flat tablet surface appeared at the circumferential edge of the gauge section (Fig. S11b), whereas nacreous tablets were exposed step by step as cracks propagated until highly packed tablet cliffs formed in the end (Fig. 21d, Figs. S11c-S11f). The competition between the radial crack driven by the radial stress gradient and the surface crack induced by the principal tensile stress created the spiral fractural surface of hydrated nacre specimens under torsion [123]. It is clear that the presence of growth layers significantly changed the crack patterns of the laminated nacre and growth layer structure under torsional loading.

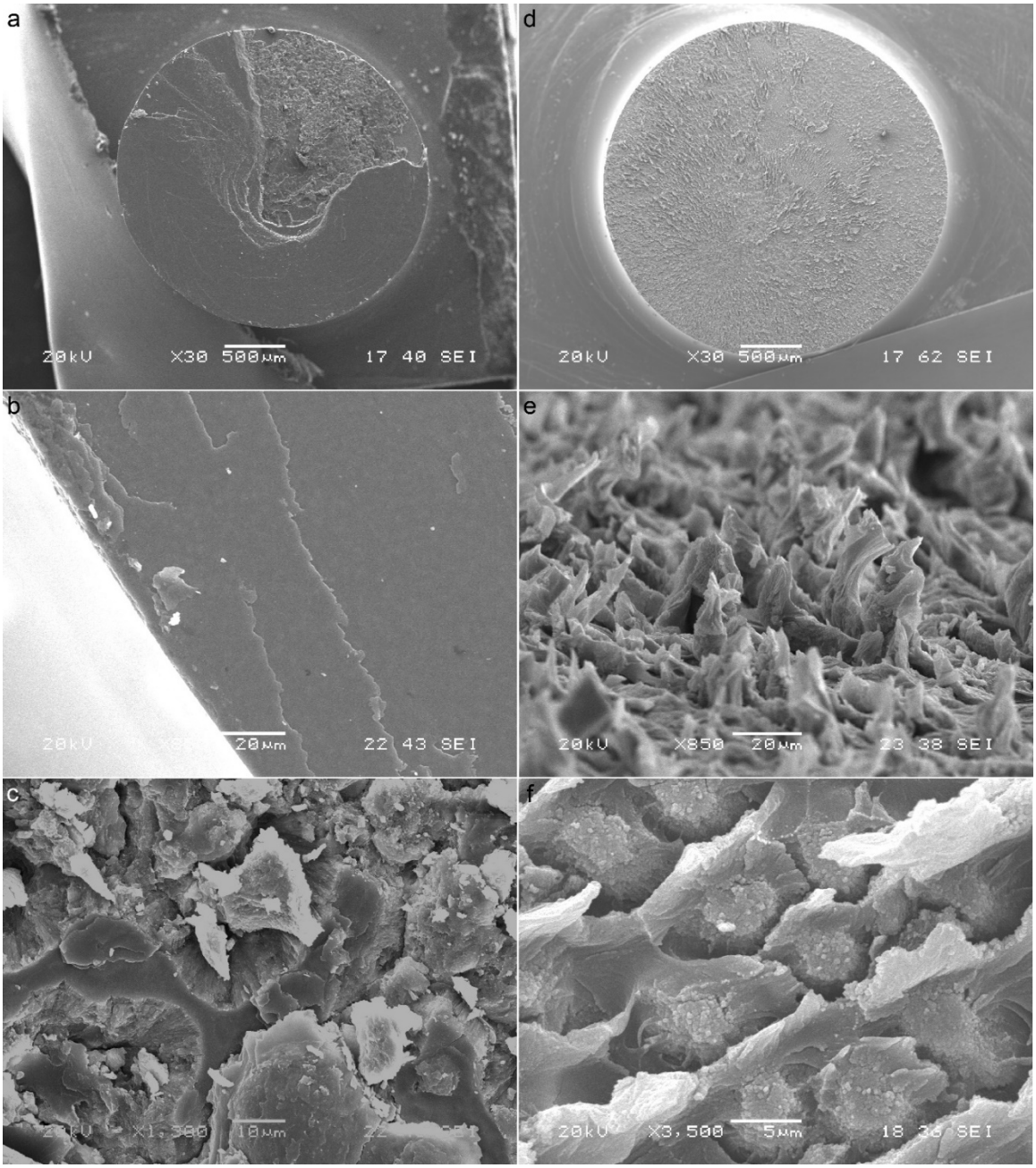

Figure 20: Fractural surfaces of dry and hydrated composite specimens under monotonic torsion. (a) Overview of the fractural surface of a dry composite specimen showed the exposed nacre and growth layers. (b) Pure nacre regions were close to the circumferential edge of the circular cross section. (c) Cleaved spherulites on part of the exposed growth layers of the dry composite specimen. (d) Overview of the fractured hydrated composite specimen. (e) Side view showed the flipped sheaths of spherulites in the hydrated

composite specimen. (f) Top view of the sheared spherulites exhibited open spaces in between in the hydrated composite specimen.

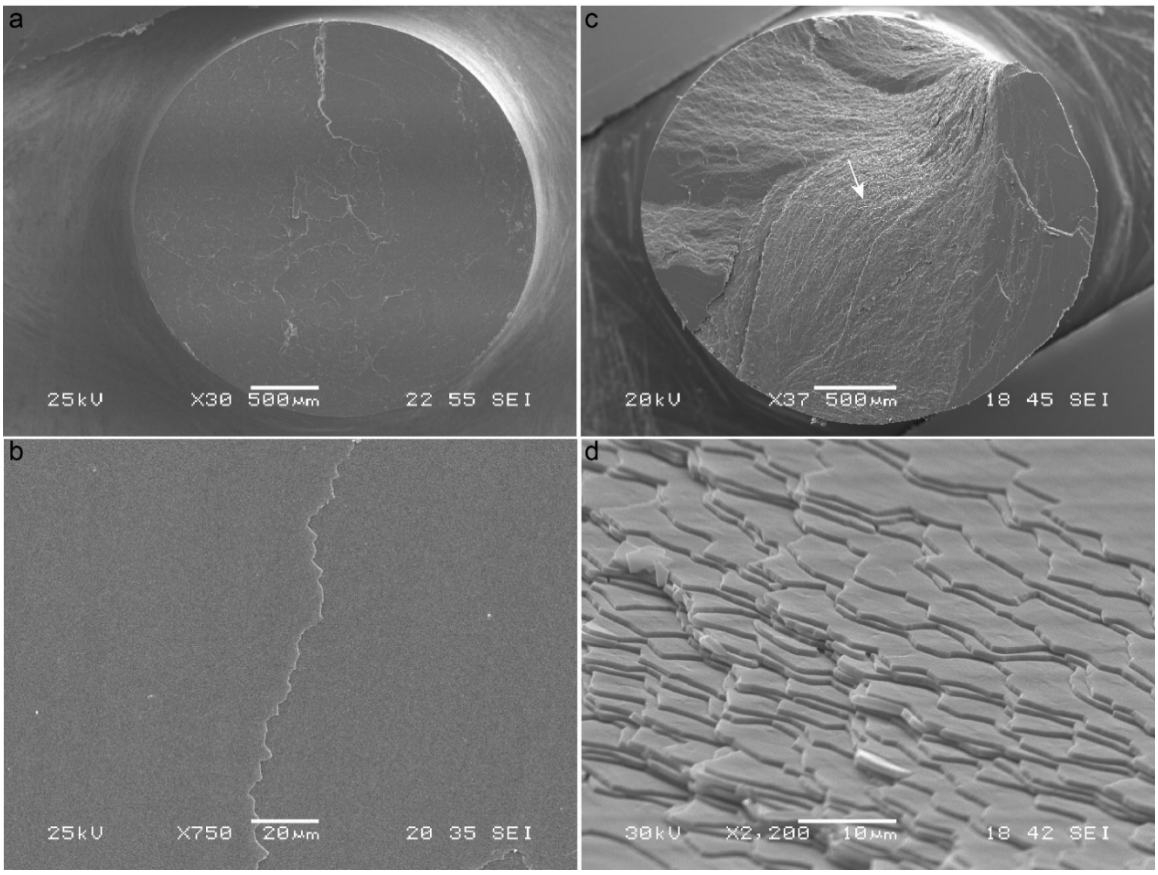

Figure 21: Fractural surfaces of dry and hydrated nacre specimens under torsion. (a) Overview of the fractured dry nacre specimen. (b) Detailed view showed that exposed nacreous layers spanned over the cross-section with a small plateau of nacreous tablets. (c) Overview of the fractured hydrated nacre specimen exhibited the spiral stair of nacreous tablets adapted from [25]. (d) Detailed view showed that step-by-step nacreous stairs on part of the fractural surface pointed by the white arrow.

4.2.5 Fractural surfaces of composite specimens under tension

Dry and hydrated composite specimens also separated into halves under tension, however very different fractural patterns were detected. In the dry composite specimen, the fractural surfaces included a combination of growth layers and nacre (Fig. 22a, Fig. S12b,

Fig. S12c). The hackle lines on the larger area of pure nacreous sections indicated fast crack propagation during failure. By tracing the lines, it was found that a fraction of the interfacial region between green matrix and spherulites was exposed around the source of cracks pointed by arrow 1. Another spherulite-green matrix interface could be found on a region close to the circumferential edge pointed by arrow 2 (Fig. 22c). Similar areas were also detected on other dry composite specimens under tension. The fractural surfaces also included pulled-out conical spherulites (Fig. 23a). Some broken spherulites included nucleated crystals on the vertices, while others did not. This was further proved by examining the mate fractural surfaces on the other half of the specimens (Fig. 23b). Some nucleated cores remained within the walls of spherulites, whereas others were removed leaving only empty holes in the place. These results showed that cracks initiated at the interface between spherulites and the green matrix in tension. However, they could kink into different parts, such as nacre or spherulites, during the propagation in dry composite specimens.

On the fractural surface of the hydrated composite specimen, most of the exposed fractural surface were covered by the green matrix. It is interesting to see that the different layers of green matrix were exposed in a stair-like way on the fractural surface (Fig. 22e, Fig. S12b, Fig. S12c), agreeing with the observation of the multilayered green matrix [92]. The flipped layer the green matrix suggested that the delamination of different layers happened very quickly due to fast cracks. Energy dispersive spectroscopic analysis was performed to examine the exposed layers in the green matrix. Distributions of different elements were captured (Fig. 24), including calcium, sodium, carbon and oxygen. Despite

the flipped area, similar distributions were acquired between different parts, i.e., areas 1, 2 and 3, for sodium, carbon and oxygen, whereas different calcium distributions were found between these areas, confirming that delaminations happened between different layers of the green matrix. At certain regions, the green matrix started to merge with isolated spherulites (Fig. 22f), consistent with the findings that the top layer of green matrix fosters the formation of spherulitic aragonites [92]. The pulled-out cones (Fig. 23c) exhibited that the delamination between the spherulites and green matrix in the hydrated composite specimen, which were further evidenced by the holes on the mate fractural surface (Fig. 23d). It should be noted that the conical vertices of the pulled-out spherulites in hydrated specimens were blunter and larger than those of dry specimens (Fig. 23a and 23c). However, no exposed nacreous sections were found on the fractural surfaces of hydrated specimens.

It is interesting to compare the performance of pure nacre under tension with those of composite specimens. The fractured dry nacre under tension exhibited a tilted surface with angles of 11.4 ± 0.5 degrees to the horizontal cross section (Fig. S14 and Table S5). Many broken pieces of nacreous tablets were found on the split halves, leaving small tablet islands on the fractural surfaces (Fig. 25a). Closer view of the broken tablets exhibited sharp edges, confirming the fast crack propagation during failure (Fig. 25b). Tablet stairs with the short tread distances occurred, from which the primary sliding direction were discerned. In contrast, the fractured hydrated nacre under tension exhibited a much flatter fractural surface with no significant tilting angle of 2.3 ± 0.2 degrees (Fig. S14 and Table S5). Fractured hydrated nacre specimens exhibited nacreous tablets with continuous

broken edges, and much less broken tablets were detected (Figs. 25c and 25d). Tablet stairs exhibited large steps with long tread distances, from which the primary sliding direction was also observed along the descending stairs.

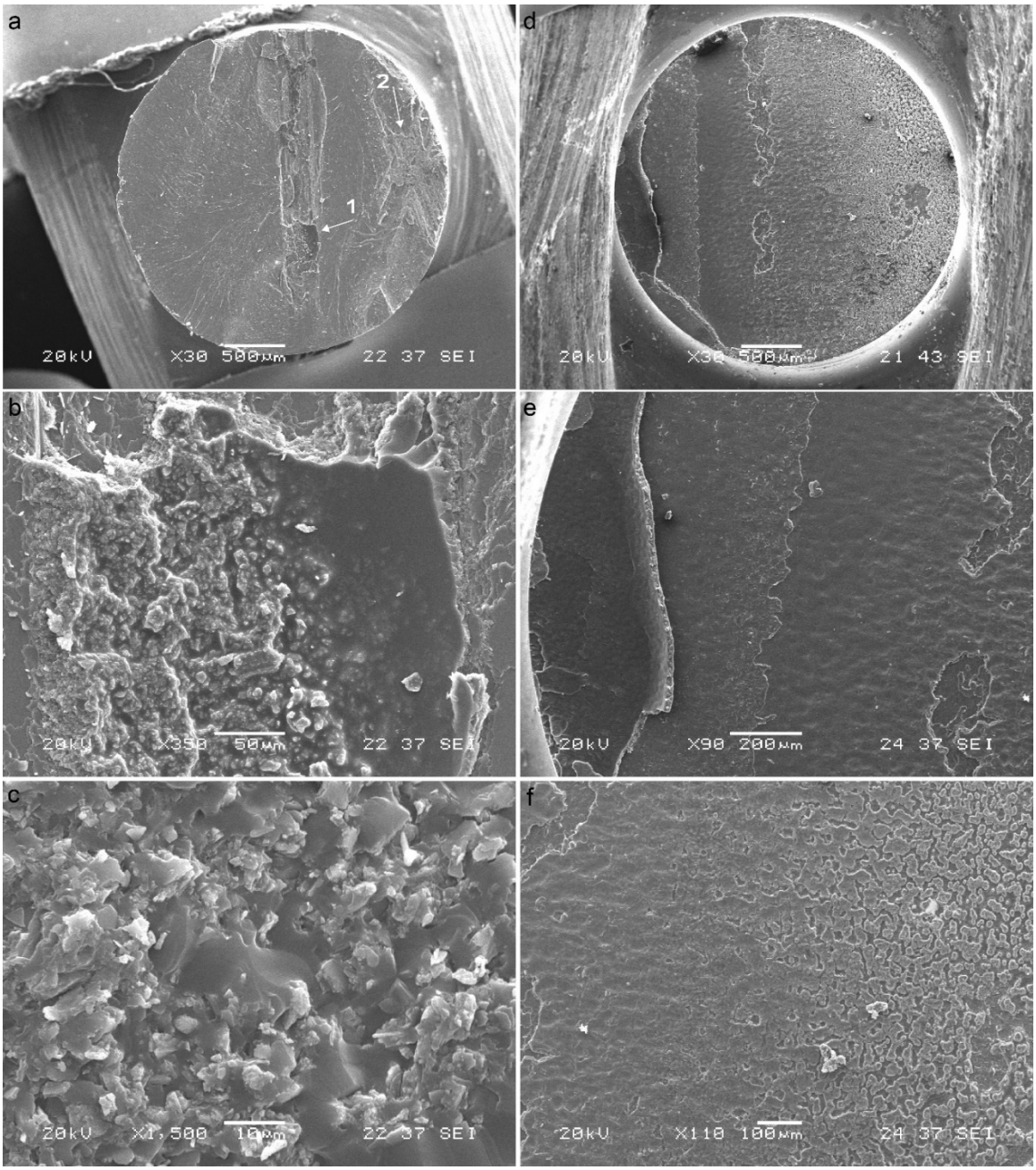

Figure 22: Fractural surfaces of dry and hydrated composite specimens under tension. (a) Overview of the fractured dry composite specimen exhibited a combination of nacre and growth layers. (b) The interface between spherulites and green matrix was found in the beginning of cracks pointed by arrow 1. (c) Delaminated spherulites and green matrix exhibited a rough surface pointed by arrow 2. (d) Overview of the fractured hydrated composite specimen exhibited multi-layers of the green matrix and exposed spherulites, but no pure nacre. (e) Detailed view showed that some layers in the green matrix was

flipped due to the fast crack propagation. (f) The transition between the green matrix to spherulites.

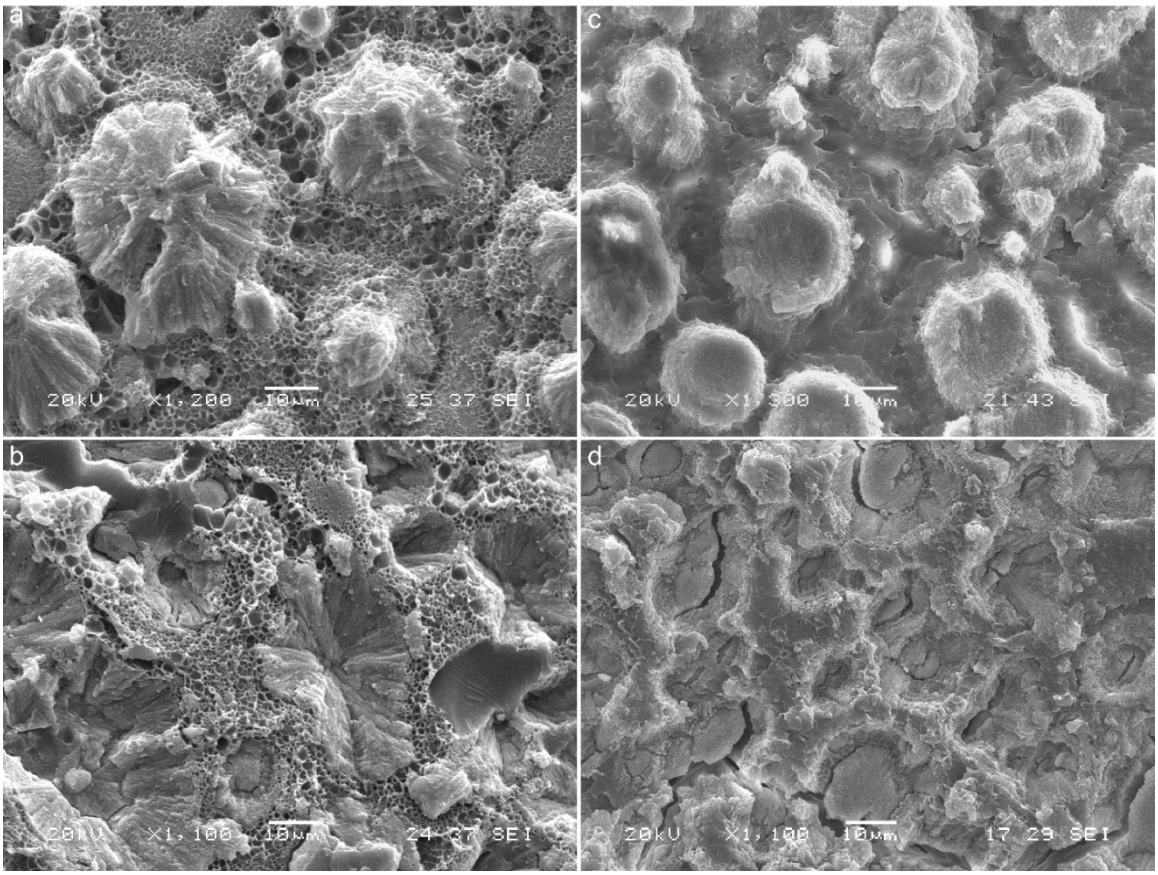

Figure 23: The broken spherulites of dry (a, b) and hydrated (c, d) composite specimens under tension (a) In dry composite specimens, some pulled-out spherulites had nucleated crystals on the conical vertices, whereas others did not. (b) On the mate fractural surface, some vacant spherulites had nucleated cores at the central bottom, while others only had empty holes. (c) In hydrated composite specimens, the pulled-out spherulites had larger and blunter plateaus on the vertices. (d) On the mate fractural surface, larger holes were created when the spherulites were pulled out.

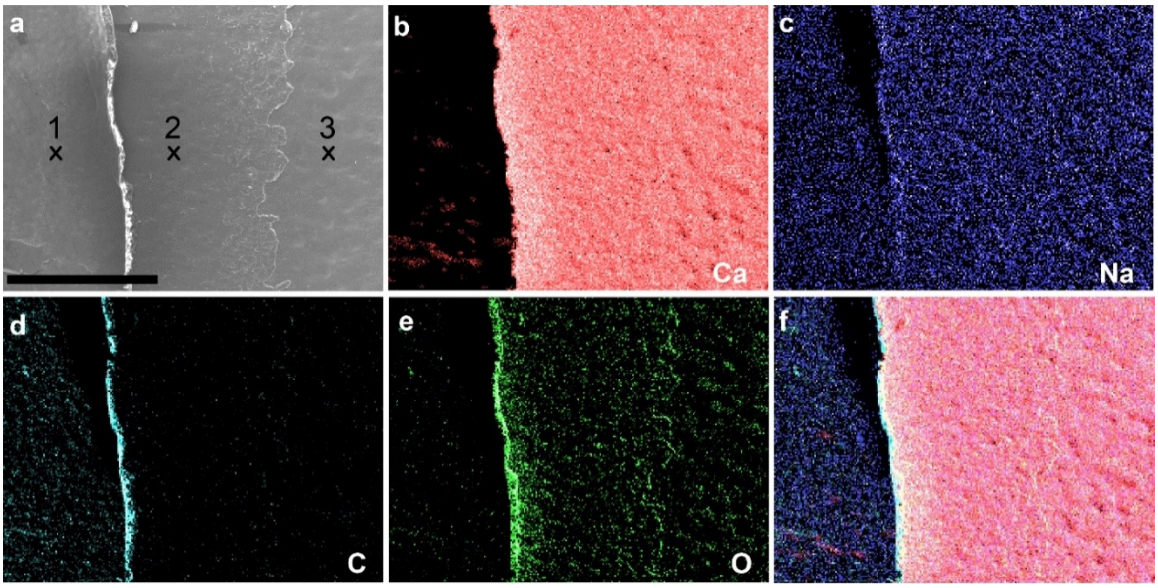

Figure 24: Energy-dispersive X-ray spectroscopy (EDS) mapping of chemical elements on the fractural surface of a tension-fractured hydrated composite. (a) An SEM image showed the target area. The elements included (b) Calcium, (c) Sodium, (d) Carbon, and (e) Oxygen. (f) An overlap of all elements is created. Scale bar in a is 300 μm. EDS of individual locations 1,2, and 3 in (a) are included in Fig. S15 in the Supplementary Materials.

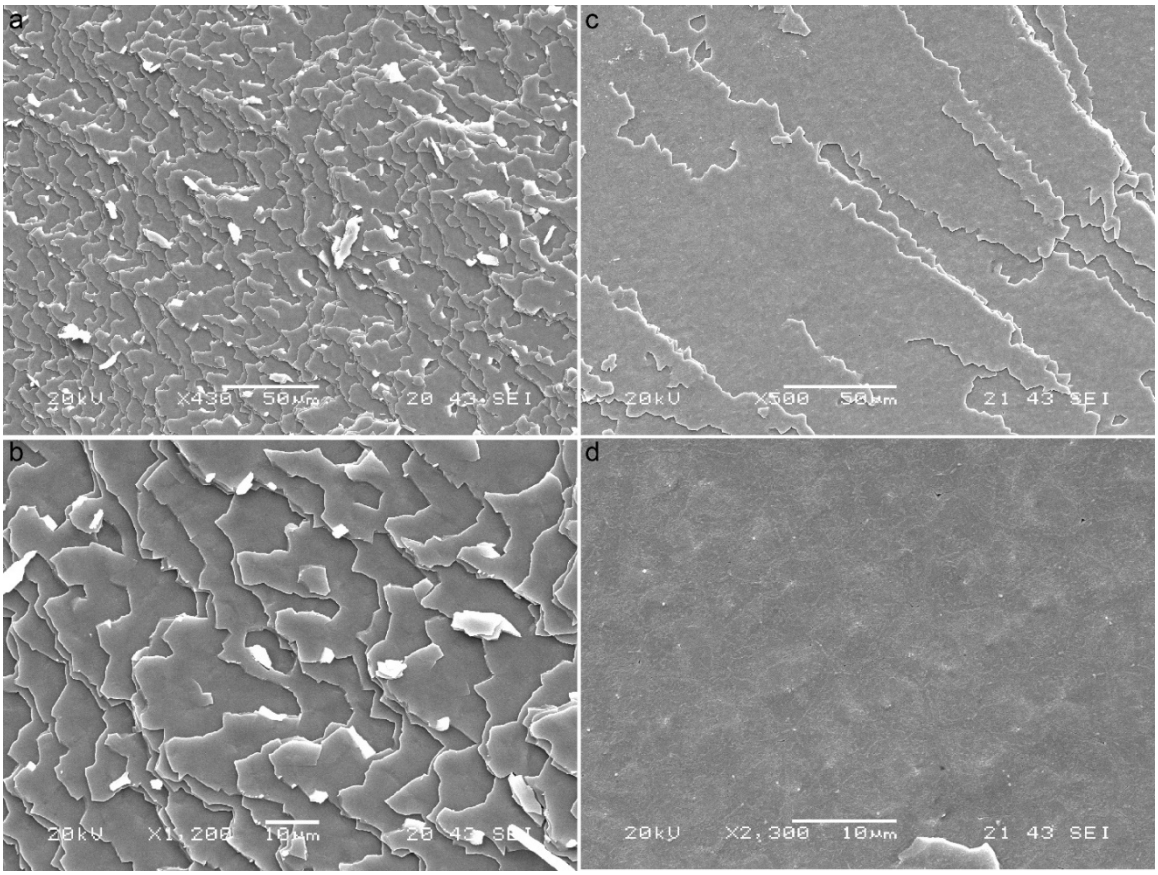

Figure 25: Fractural surfaces of dry and hydrated nacre specimens under tension. (a) Broken tablets of dry nacre scattered over the fractural surfaces. (b) Detailed view of the broken nacreous tablets exhibited the sharp edges. (c) Fractural surfaces of hydrated nacre specimens exhibited nacreous tablets with continuous broken edges. (d) Detailed view of the surface of hydrated nacre.

4.2.6 Bump statistics under torsion

The high temporal resolution stress-strain curves disclosed the minute variations of microstructures during loading. Stress variations were detected on the increase stages of surface shear stress-surface shear strain curves of hydrated nacre specimens under monotonic torsion. Each stress bump isolated from the main curve was measured by two features, i.e., bump height and bump distance (Fig. 17b). Bump height is the stress

difference between the peak and minimum stress points, whereas bump distance is the strain difference between the starting and ending points. The complementary cumulative distribution function (CCDF) of bump heights collected from the hydrated nacre specimens under torsion is shown in Fig. S16. Similarities were found among different stress bumps when they were overlapped from the same starting point (Fig. 26). The stress bumps of the hydrated nacre specimens spanned over bump heights of 0.8 MPa and bump distances of 2.2e-3. However, no variations of surface shear stresses were detected on the increase stages of the dry nacre specimens under monotonic torsion. Also, very limited stress variations were detected on the increase stages of dry and hydrated composite specimens under monotonic torsion.

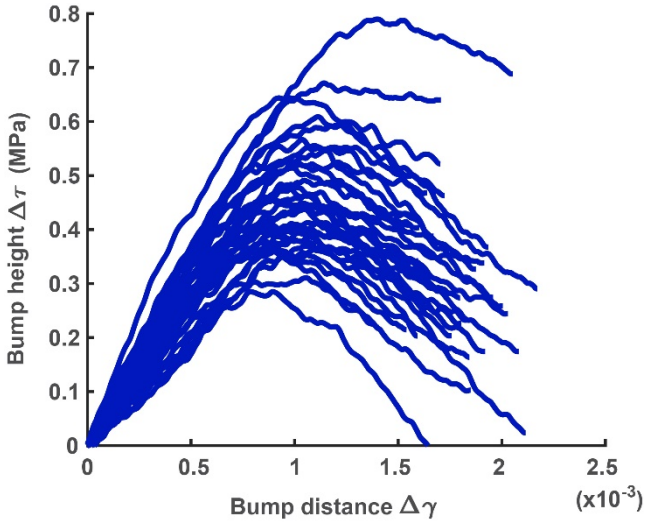

Figure 26: Overlapped stress bumps of hydrated nacre specimens under monotonic torsion.

4.2.7 Bump statistics under tension

Stress variations were detected on the tensile stress-strain curves of dry and hydrated composite specimens. CCDFs of bump heights collected from the dry and

hydrated composite specimens under tension are shown in Fig. 27d. When overlapped on the same starting point, the stress bumps of dry composite specimens spanned over bump heights of 0.36 MPa and bump distances of 3.0e-4, whereas the stress bumps of hydrated composite specimens spanned over bump heights of 0.25 MPa and bump distances of 1.7e-3. DBSCAN [124] clustering algorithm was used to further compare the stress bumps of dry and hydrated composite specimens under tension. Even though some overlapping occurred, two clusters with distinctive features were evident (Fig. 27c). The same analyses were performed to investigate the stress variations on the tensile stress-strain curves of dry and hydrated nacre specimens (Fig. S17). Stress bumps of dry nacre specimens under tension spanned over bump heights of 1.1 MPa and bump distances of 1.5e-4, whereas stress bumps of hydrated nacre specimens under tension spanned over bump heights of 1.2 MPa and bump distances of 4.5e-4 (Fig. S17). Dry and hydrated clusters for pure nacre were also confirmed using the DBSCAN method. The results showed that stress bumps of composite specimens under tension were different from those of pure nacre specimens (Fig. 27 and Fig. S17). In general, tensile stress bumps in composite specimens exhibited less heights and larger distances than those in nacre specimens (Figs. 27e, 27f). Both composite and nacre specimens exhibited slightly larger bump heights and smaller bump distances in the dry condition than in the hydrated condition.

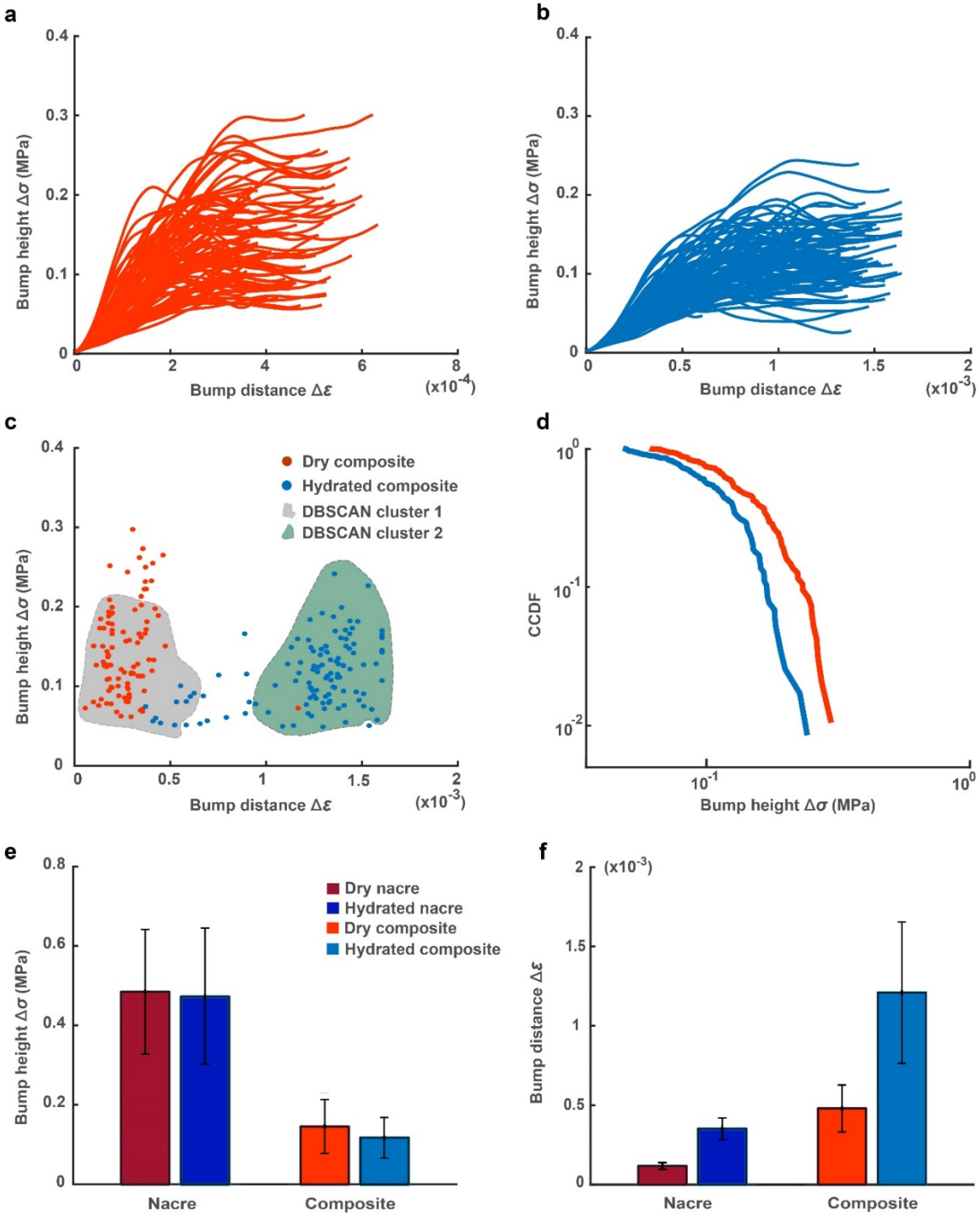

Figure 27: (a) Overlapped stress bumps of dry composite under monotonic tension. (b) Overlapped stress bumps of hydrated composite under monotonic tension. (c) Two clusters were obtained from the DBSCAN clustering algorithm based on stress bump heights and

distances. (d) Complementary Cumulative Distribution Functions (CCDFs) of bump heights for hydrated nacre specimens under monotonic tension. Statistical values of (e) bump heights and (f) bump distances of both composite and nacre specimens under tension.

4.3 Discussions

These results provided essential clues to reveal the toughening mechanisms of growth layers under tensile and shear loadings, which are further elucidated by comparing the performance of pure nacre and growth layers in the corresponding conditions.

4.3.1 Shear resistance of the growth layers

Under torsion, two-dimensional shear stress planes are stacked along the longitudinal axis of the cylindrical specimens (Fig. 15). Due to the mismatch between laminated layers, the weakest link in the composite system is failed by the surface shear stress of torsion, i.e., the maximum shear stresses on the two-dimensional plane. The destruction of the local surface region (either growth layers or nacre) led to the catastrophic failure of the specimen because of the fast cracks generated by the large stress gradient along the radius.

The dry nacre under torsion exhibited the shear strengths of 45.2 ± 16.0 MPa at 2.0 ± 0.8% shear strain. The stress-strain curves exhibited a linear increase and a sharp decrease with limited plasticity. Flat fractural surface covered the entire cross section with only a small plateau of nacreous tablets. This was because once the mineral bridge on the surface tablet failed, stresses of the unbroken bridges increased so that they also broke immediately. Therefore, a gap between nacreous tablets on the cylindrical surface enabled cracks to propagate perpendicularly to the sliding direction due to the large stress gradient

across the radius (Figs. 28e-28h). The crack propagation was fast enough to confine the fracture almost between adjacent nacre tablets, during which the microscale toughening mechanisms were not triggered since there was limited chance for the interaction of nacreous tablets [122].

The hydrated nacre exhibited the shear strengths of 54.8 ± 6.5 MPa at the shear strain of 12.7 ± 2.0%. The stress-strain curves exhibited a linear increase, a transitional stage and an extended bumpy stage before the sharp decrease. The presence of water changed the story because hydrogen bonds formed between water molecules and the chitin fiber network, between water molecules and proteins, or within themselves. In the linear increase stage, mineral bridges, nanoasperities and organic matrices worked together to resist the shear. Because of water, stress redistributions in hydrated nacre became more complicated than those in dry nacre because temporal stress redistribution paths could be established due to the interactions between water molecules on tablet surfaces and the more stabilized organic matrices. When a mineral bridge broke, it took longer to redistribute shear stresses to other areas due to these time-dependent interactions. During this process, part of the shear stresses was transferred to the contacted nanoasperities as the tablet spacing decreased. The redistribution continued until all mineral bridges broke and the contacted nanoasperities took over the shear resistance. The shear stress variations kept occurring intermittently as the tablets slid over each other (Figs. 28l-28o). Once the critical sliding distance was achieved, the stress gradient enabled cracks to propagate radially that led to the catastrophic failure of hydrated nacre [123].

The dry composite specimens exhibited the shear strengths of 37.2 ± 5.4 MPa at 10.9 ± 1.0% shear strain. On the fractural surfaces of dry composite specimens, pure nacre sections existed on the circumferential edges, and growth layers with sheared spherulites were exposed (Fig. 20). This was because cracks initiated from the nacreous sections on the surface, then kinked into growth layers when the pure shear stress condition was not maintained during the crack propagation. It should be noted that the shear strengths of dry composite specimens and dry nacre were very close to each other (Fig. 18b), and cracks both initiated from nacreous section on the cylindrical surface. This was because extremely high stress concentrations occurred at the nanoscale mineral bridges (~50 nm in diameter) between the surface tablets, which tended to break first under torsional load (Fig. 28). Dry composite specimens exhibited larger shear strain at failure than dry nacre specimen because the growth layers provided the extra deformation under shear.

The hydrated composite specimens exhibited the shear strengths of 23.8 ± 3.4 MPa and 21.4 ± 5.0% shear strain at failure. Due to the presence of water, hydrogen bonds provided that extra connections that helped distribute stresses more evenly to different parts of the composite. Thus, stress concentrations at the mineral bridges were significantly alleviated. A substantially lower shear strength occurred because the spherulites with porous structures became the weakest link in the entire system. On the fractural surface, crack propagated almost entirely across the hydrated spherulites, which was evidenced by the flipped skins of broken spherulites (Figs. 20d-20f), through which a primary direction was discerned by their collective response to the crack. The presence of water also produced larger shear strain at failure because the growth layer reinforced by hydrogen

bonds provided the extra deformation under shear. In general, the hydrated growth layers successfully confined the shear cracks within themselves.

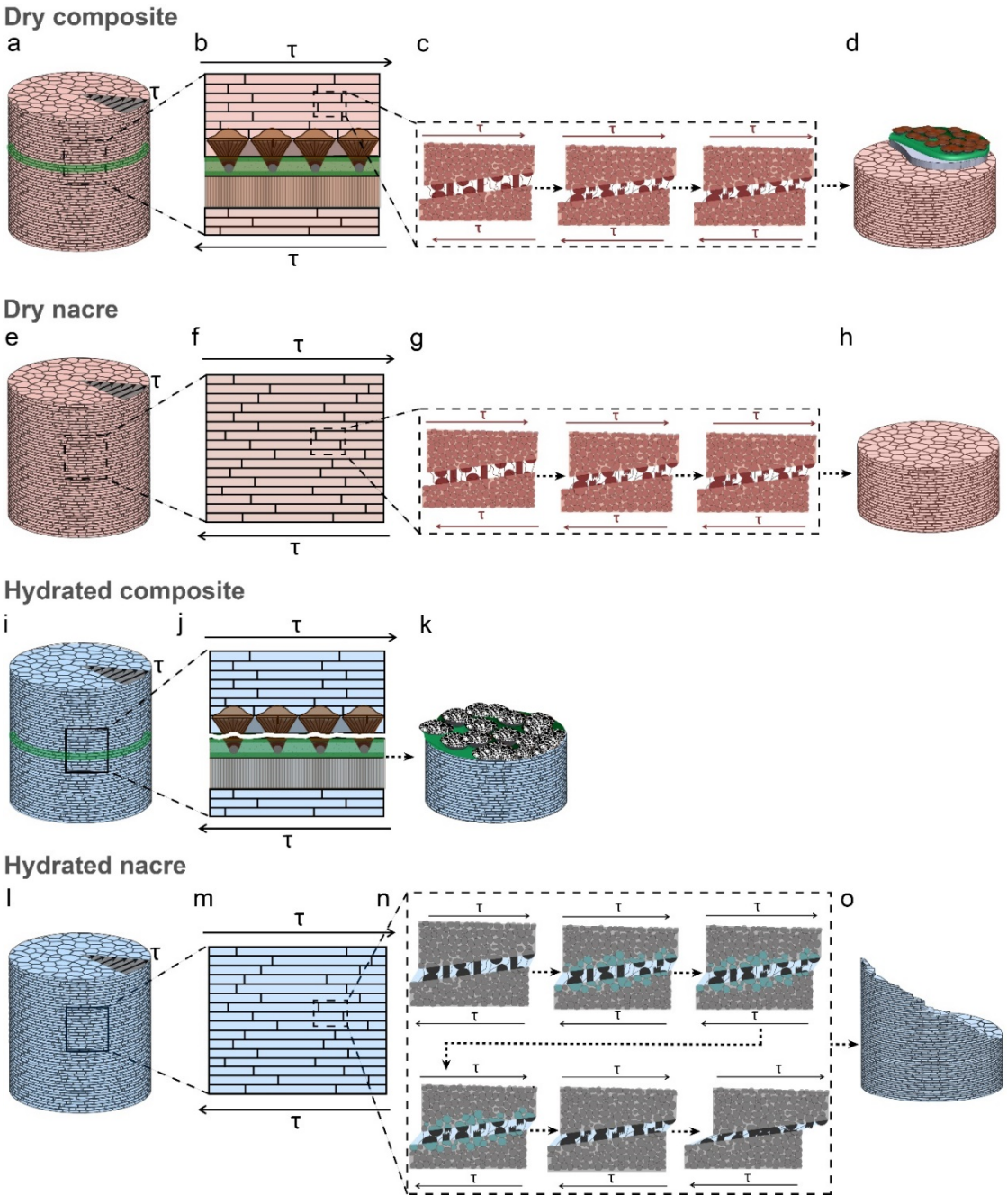

Figure 28: Schematic diagrams of toughening mechanisms to resist shear under torsion are constructed for composite and nacre specimens. (a, b, c, d) In dry composite, cracks initiate from mineral bridges in pure nacre due to high stress concentrations, and kink into growth

layers during propagation. (e, f, g, h) In dry nacre, cracks initiate from mineral bridges in pure nacre, and propagate almost between adjacent nacreous layers at failure. (i, j, k) In hydrated composite specimens, crack initiate and propagate within spherulites with porous structures. (l, m, n, o) In hydrated nacre, cracks initiate between nacreous tablets. A spiral fractural surface is created due to the competition between principal tensile stresses on the surface and the graded stress along the radius. (c), (g) and (n) are adapted from Alghamdi et al. 2018 [123].

4.3.2 Tensile resistance of the growth layers

Under tension, stresses varied along the longitudinal axis because of the different laminated layers in the composite. The destruction of the weakest link, i.e., layers or interfaces [125-131], resulted in the failure of the entire composite.

Dry nacre exhibited tensile strengths of 29.8 ± 3.2 MPa at 0.6 ± 0.1% tensile strain. The stress-strain curves included a linear increase and a sharp decrease with limited plasticity. The flat fractural surface exhibited inclined angles of 11.4 ± 0.5 degrees relative to the horizontal cross section. Many small and broken tablets were found, and a primary sliding direction could be discerned by the short descending steps. This was because nacreous tablets broke at multiple locations when they slide over each other, or the spiral connections [100,122] between different nacreous tablets broke under tension. The intermittent breakage was evidenced by the recurring stress bumps of the stress-strain curves under tension. Substantial sliding occurred upon failure under combined normal and shear stresses. When the critical point was achieved, a catastrophic slide occurred to conclude the failure of dry nacre under tension (Figs. 29d, 29e).

Hydrated nacre exhibited tensile strengths of 22.8 ± 2.3 MPa at 1.4 ± 0.0 tensile strain. The stress-strain curves also included a linear increase and a sharp decrease with limited plasticity, but the flat fractural surface showed limited tilting. In contrast to dry

nacre, the fractural surfaces of hydrated nacre included nacreous tablets with continuous broken edges and much less isolated broken tablets, which was also evidenced by the distinctive stress bumps of the stress-strain curves (Figs. 27e, 27f). The tablet stairs of hydrated nacre had larger steps compared to those of dry nacre, from which the primary sliding direction were also observed. This was because the presence of water provided the extra lubrication to tablet sliding. Thus, fewer breakage of nacreous tablets was needed to create the essential sliding path, on which a lower tensile strength was acquired. Again, the failure strain of hydrated nacre was larger than that of dry nacre because water promoted the extra deformation (Figs. 29i, 29j).

The dry composite specimens exhibited tensile strengths of 8.4 ± 2.1 MPa at 2.8 ± 0.4% tensile strain. The fractural surfaces included exposed interfacial regions between spherulites and the green matrix as well as pure nacre sections. This was because the connection between spherulites and green matrix was the weakest link of the composite system. Under tension, debonding between the spherulites and the green matrix initiated the cracks. This was confirmed by the pulled-out conical spherulites on the fractural surfaces, and by the stress variations of stress-strain curves of dry composite specimens under tension. The local failure kept occurring until the critical threshold was achieved, after which cracks propagated quickly into different parts of the composite system, such as the nacreous sections. These cracks eventually led to the catastrophic failure of the dry composite specimens (Figs. 29a-29c).

The hydrated composite specimens exhibited tensile strengths of 6.0 ± 1.5 MPa at 7.7 ± 1.0 tensile strain. The fractural surfaces included exposed spherulite-green matrix

interfaces and multiple delaminated layers of the green matrix. Similar to the dry composite specimens, spherulites with conical walls were pulled-out from the green matrix, confirming that the interface between spherulites and green matrix was still the weakest link. Due to the presence of water, stress bumps of the stress-strain curves in hydrated composite specimens exhibited smaller heights and larger distances than those of the dry composite specimens (Figs. 27e, 27f). Meanwhile, larger and flatter plateaus were found in the pulled-out conical spherulites of hydrated composite specimens than those in dry composite specimens. These results showed that hydrogen bonds helped alleviate the sudden stress drops by holding different parts more tightly. In hydrated composite specimens, stresses were redistributed more effectively to different parts in the composite due to hydrogen bonds. Thus, the relatively soft green matrix absorbed most of the energy during crack propagation, leading to the delamination of multiple layers at failure. The failure strain of hydrated composite specimens was larger than those of dry composite specimens because extra deformation was provided by water. Again, the hydrated growth layers successfully confined and deflected cracks within themselves under tension (Figs. 29f-29h).

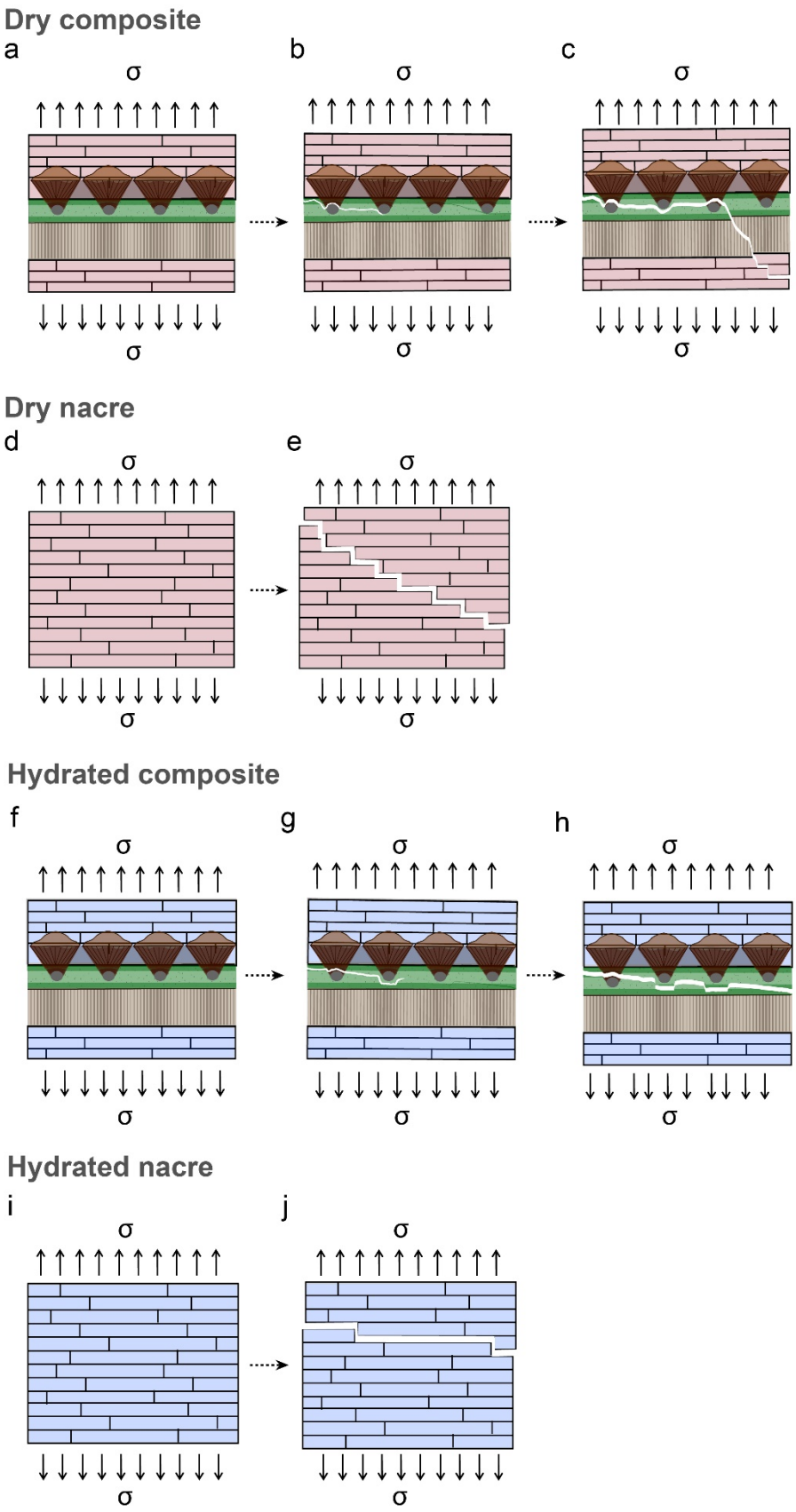
Dry composite
a
σ
σ
b
σ
σ
c
σ
σ
Dry nacre
d
σ
σ
e
σ
σ
Hydrated composite
f
σ
σ
g
σ
σ
h
σ
σ
Hydrated nacre
i
σ
σ
j
σ
σ

Figure 29: Schematic diagrams of toughening mechanisms to resist tension are constructed for composite and nacre specimens. (a,b,c) In dry composites, cracks initiate from interfaces between spherulites and the green matrix, and kink into different parts of the composite during propagation. (d,e) In dry nacre, sliding occurs over short tablet stairs with broken tablets. (f,g,h) In hydrated composites, cracks initiate from interfaces between spherulites and the green matrix, and propagate within different layers of the green matrix. (i, j) In hydrated nacre, sliding occurs over large tablet stairs with continuous broken edges.

4.4 Conclusions

In this work, we studied the tensile and shear behavior of growth layers between bulk nacre in red abalone. Dog-bone shaped specimens were prepared by making the laminated nacre and growth layers perpendicular to the longitudinal axis. By coupling different load cells, experimental systems were created to collect the high temporal resolution stress-strain curves under monotonic torsion and tension tests. Data collected at ultrahigh sampling rates detailed the minute microstructural variations under dry and hydrated conditions. As a comparison, pure nacre specimens were tested to elucidate the characteristic behavior of growth layers.

Under monotonic torsion, dry nacre exhibited a flat fractural surface over the gauge section with only small tablet plateaus. No substantial stress variations were detected in the increase stages based on the high sampling rate data, confirming that the mineral bridges deformed evenly before breakage. When mineral bridges between the surface nacreous tablets broke, cracks propagated rapidly due to the large stress gradient along the radius, resulting in the catastrophic failure of dry nacre with limited plasticity. The microscale toughening mechanisms were not triggered since there was little chance for nacreous tablets to interact after the mineral bridges broke. In hydrated nacre, the presence of water induced plasticity before the catastrophic failure. The organic matrices reinforced by

hydrogen bonds provided temporal paths of stress redistributions. As mineral bridges broke, shear stresses were transferred gradually to the contacted nanoasperities. The redistribution continued until all mineral bridges broke and the contacted nanoasperities took over the shear resistance. The unstable state could not last as the sliding continued during which the shear stress variations kept occurring since the tablets interacted with each other intermittently. When the sliding distance was large enough, cracks propagated to form the spiral fractural surface as a result of the competition between stress gradient along the radius and the principal stresses on the cylindrical surface.

Under monotonic torsion, the fractural surfaces of dry composite specimens included nacreous sections and exposed growth layers. Because of the high stress concentrations, the breakage of nanoscale mineral bridges on the surface tablets initiated the cracks. The fast cracks driven by the large stress gradient along the radius propagated into different parts of the composite, including the sheared spherulites. However, the fractural surface of hydrated composite specimens were primarily the sheared spherulites. This was because the hydrogen bonds helped redistribute stresses more effectively between different composite parts, which substantially alleviated the stress concentrations around mineral bridges between nacreous tablets. Thus, the spherulites with porous microstructures became the weakest link, and localized most cracks upon failure. Therefore, dry composite specimens exhibited the similar shear strengths to that of dry nacre, which were higher than the shear strengths of hydrated composite specimens. Meanwhile, hydrated composite specimens exhibited larger shear strain at failure than dry

specimens because the composites reinforced by hydrogen bonds produced extra deformation.

Under monotonic tension, the fractural surfaces of dry nacre included tilted nacre stairs with small steps and short tread distances, on which many small broken tablets were scattered. This was because nacreous tablets broke at multiple locations when nacreous tablets slide over each other, or the spiral connections between different nacreous tablets broke under tension. The intermittent breakage was evidenced by the stress bumps in the increase stages of stress-strain curves. After that, a catastrophic failure occurred. In contrast to dry nacre, the fractural surfaces of hydrated nacre included continuous tablet stairs with large steps and long tread distances, on which much less broken tablets were detected. The stress bumps of hydrate nacre exhibited smaller heights and larger distances than those of dry nacre. This was because the presence of water provided the extra lubrication so that the essential sliding paths were achieved with less broken tablets. Therefore, hydrated nacre exhibited lower tensile strength and higher tensile strain at failure than dry nacre.

Under monotonic tension, the fractural surfaces of dry composite specimens included nacreous sections and exposed growth layers. Crack initiated from the debonding between spherulites and green matrix, during which conical spherulites were pulled out from the green matrix. This was also evidenced by stress bumps in the stress-strain curves. Once the critical point was achieved, cracks kinked abruptly into different parts of the composite system that led to the failure of the dry specimen. In contrast, the fractural surfaces of hydrated composite specimens included the exposed interfaces between spherulites and the green matrix and multiple delaminated layers of the green matrix.

Similar to dry composites, cracks initiated from the spherulite-green matrix interfaces in hydrated composites. Stress bumps in hydrated composite specimens were smaller in heights and larger in distances than those of dry composite specimens because hydrogen bonds helped alleviate the sudden stress drops by holding different parts together. Because stress distributed more evenly in hydrated composite, the relatively soft green matrix localized most propagated cracks, resulting in the delaminated layers of the green matrix upon failure. The hydrated composites exhibited slightly smaller tensile strengths but substantially larger failure strain at failure than those of dry composites.

In general, hydrated composites exhibit lower strengths but larger strain at failure than hydrated nacre under tension and shear loadings. Growth layers are weaker in tensile and shear resistance than pure nacre, but they also successfully confine and deflect cracks when failure happens. The proposed work generated novel understandings on how the seashell tune the microstructures of microscale growth layers to resist tension and shear. In addition to the side view characterization of pure nacre and micro-growth layers [31,61,102,132], the fractural patterns of growth layers and nacre under tension and shear were elucidated from the top view in this work. By successfully separating the adjacent nano-/micro-layers in pure nacre or growth layers using torsion and tension tests, we present the first observations of the flipped spherulite skins under shear of torsion, the pulled-out spheruites from the green matrix under tension, and the delamination of the multiple layers in the green matrix. The introduction of growth layers substantially increases the composite deformation compared to that of pure nacre in corresponding loading conditions. These direct evidences exhibit how alternating soft and hard materials

are used to achieve the extraordinary mechanical behavior of seashells. These findings could provide essential clues for the creation of high performance composites (or artificial nacre). For example, material selections could be conducted based on the contrast between morphology and elastic moduli of pure nacre and growth layers, where the interfacial strengths of tension and shear between soft and hard layers could be tailored by learning connections between spherulites and growth layers. The hierarchical morphology and mechanical properties could localize the damage of artificial composites made by conventional synthetic methods or additive manufacturing, which thereby protects other parts of the composites effectively. Meanwhile, the hydrophobicity of constituents could be tuned to promote the composite performance under different humidity conditions through which fractural patterns are well controlled.

Experimentally, we isolate the performance of microscale growth layers from that of pure nacre using relatively large specimens (mm in size) under torsion and tension. It is challenging to use nano-/micro-scale specimens to test the mechanical behavior of materials, such as nacre or growth layer composites, because the fabrication process may affect the representative unit that contains the intricate microstructures. We match the discretizational features of torsion and tension to laminated composites consisting of nano-/micro-scale layers, which helps reduce the influence from the specimen fabrications. In torsion, once the surface fails, the tests end immediately because cracks propagate very fast across the radius due to the large stress gradient. The interfacial behavior between adjacent layers is isolated from that of the entire system. Thus, this method could test nano-/micro-scale features of natural materials that are not easily reproduced by current technology. In

tension, the weakest link of the layered composites is exposed by successfully aligning the loading direction perpendicular to the layers. Meanwhile, the application of ultrahigh sampling rate details the microstructural evolution of pure nacre or growth layer composites under different loadings. The large amount of data on stress and strain quantify the characteristic microstructural interactions at different loading or hydrated conditions. Our study could lead to further insights into the mechanical behavior of various artificial and natural materials, such as the interfacial behavior of nano-/micro-scale laminated materials under different conditions, and thereby inspire the creation of high performance hierarchical composites.

Chapter 5: Conclusions and Future Work

By applying pure shear stresses of torsion on small dog-bone samples of dry pure nacre, we reveal dry nacre's torsional linear response during the initial tablets sliding. Due to torsion, specimens failed catastrophically at the proportional limit with minimized plasticity. This is because the cracks propagate perpendicularly to the sliding direction once the mineral bridges break, during which the nacreous tablets have little chance to provide the shear resistance. In addition, the brittle fracture observed between dry nacreous tablets interfaces due to torsion is a convincing proof that microscale toughening mechanisms were not triggered to promote a ductile behavior. Numerical modeling of the two nacreous tablets and their interface suggests that mineral bridges contribute dominantly to the sliding resistance, while nanoasperity contact and protein chains contribute limitedly in this stage. Nevertheless, when hydrated nacre is subjected to torsional loads, the deformation of nanograins inside nacreous tablets and intergrain proteins allow for extra sliding before the breakage of mineral bridges. The presence of hydrogen bonds between water molecules and organic matrices, or within water molecules enable temporal paths for stress redistributions. During sliding of hydrated nacreous tablets, the shear stresses are gradually transferred to contacted nanoasperities as mineral bridges break sequentially, after which the subsequent sliding induces intermittent, dynamic interactions between adjacent nacreous tablets. When the sliding is large enough, the large stress gradient propagates cracks radially and fail hydrated nacre catastrophically. The evolution of nanoscale toughening mechanisms in dry and hydrated nacre were demonstrated, in which water brings plasticity to the interface between nacreous tablets during the initial sliding. We

also showed that both dry and hydrated nacre fail catastrophically under pure shear stresses of torsion, before the microscale toughening mechanisms are triggered. Experimentally, we isolated a nanoscale interface between tablets from a large nacre specimen (mm in size) using torsion. It is challenging to use nano-/micro-scale specimens to test the mechanical behavior of materials, such as nacre or growth layer composites, because the fabrication process may affect the representative unit that contains the intricate microstructures. We match the discretizational features of torsion and tension to laminated composites consisting of nano-/micro-scale layers, which helps reduce the influence from the specimen fabrications. In torsion, once the surface fails, the tests end immediately because cracks propagate very fast across the radius due to the large stress gradient. The interfacial behavior between adjacent layers is isolated from that of the entire system. Thus, this method could test nano-/micro-scale features of natural materials that are not easily reproduced by current technology. The ultrahigh sampling rate enabled the acquisition of highly detailed microstructural interactions between nanolayers. Findings from this study open an exciting perspective into studying mechanical properties of natural and artificial layered materials using pure shear stresses of torsion.

The abalone shells don't only contain nacre in their structures, but also growth layers. We showed that hydrated samples with growth layers "hydrated composites" exhibit lower strengths but larger strains at failure than hydrated nacre under tension and shear loadings. Growth layers are shown to be weaker in tensile and shear resistance than pure nacre, however, they successfully confine and deflect cracks when failure occurs. Novel understandings on how the seashell tune the microstructures of microscale growth

layers to resist tension and shear were generated. Beside the side view characterization of pure nacre and micro-growth layers, the fractural patterns of growth layers and nacre under tension and shear were revealed from the top view. By successfully separating the adjacent nano-/micro-layers in pure nacre or growth layers using torsion and tension tests, the first observations of the flipped spherulite skins under shear of torsion, the pulled-out spheruites from the green matrix under tension, and the delamination of the multiple layers in the green matrix were presented.

The introduction of growth layers substantially increased the composite's deformation compared to that of pure nacre in corresponding loading conditions. These direct evidences showed how alternating soft and hard materials are used to achieve the extraordinary mechanical behavior of seashells. These findings could aid the creation of high performance composites (or artificial nacre). For instance, selection of materials could be determined based on the contrast between morphology and elastic moduli of pure nacre and growth layers, where the interfacial strengths of tension and shear between soft and hard layers could be learned and tailored from the connections between spherulites and growth layers. Finidngs from thses studies reinforce the fact that hierarchy of morphology and mechanical properties could help with damage localization. Meanwhile, the hydrophobicity of constituents could be also tuned to promote the composite performance under different humidity conditions where fracture patterns can also be predicted.

References

[1] Dunlop, J. W. C., & Fratzl, P. (2010). Biological composites. *Annual Review of Materials Research, 40*, 1-24. doi:10.1146/annurev-matsci-070909-104421

[2] Wegst, U. G., Bai, H., Saiz, E., Tomsia, A. P., & Ritchie, R. O. (2015). Bioinspired structural materials. *Nature Materials, 14*(1), 23-36.

[3] Sebastian Lee, P. D. Z., Alejandro Strachan. (2014). Bio composite simulator. Retrieved from https://nanohub.org/resources/nacresimulator

[4] Wang, S.-N., Zhu, X.-Q., Yan, X.-H., Deng, J.-F., Wang, R., & Wang, X.-X. (2015). Nanostructured individual nacre tablet: A subtle designed organic–inorganic composite. *Crystal Engineering Communications, 17*(15), 2964-2968.

[5] Jackson, A. P., Vincent, J. F. V., & Turner, R. M. (1988). The mechanical design of nacre. *Proceedings of the Royal Society Series B-Biological Sciences, 234*(1277), 415-440. doi:10.1098/rspb.1988.0056

[6] Wise Jr, S. W. (1970). Microarchitecture and mode of formation of nacre (mother of pearl) in pelecypods, gastropods and cephalopods. *Eclogae Geologicae Helvetiae, 63*, 775-797.

[7] Currey, J. (1977). Mechanical properties of mother of pearl in tension. *Proceedings of the Royal Society of London B: Biological Sciences, 196*(1125), 443-463.

[8] Sarikaya, M., Gunnison, K., Yasrebi, M., & Aksay, I. (1989). Mechanical property-microstructural relationships in abalone shell. *MRS Online Proceedings Library Archive, 174*.

[9] Currey, J. D., Zioupos, P., Davies, P., & Casino, A. (2001). Mechanical properties of nacre and highly mineralized bone. *Proceedings of the Royal Society of London B: Biological Sciences, 268*(1462), 107-111. doi:10.1098/rspb.2000.1337

[10] Gao, H., Ji, B., Jäger, I. L., Arzt, E., & Fratzl, P. (2003). Materials become insensitive to flaws at nanoscale: Lessons from nature. *Proceedings of the National Academy of Sciences, 100*(10), 5597-5600.

[11] Li, X. D., Chang, W. C., Chao, Y. J., Wang, R. Z., & Chang, M. (2004). Nanoscale structural and mechanical characterization of a natural nanocomposite material: The shell of red abalone. *Nano Letters, 4*(4), 613-617. doi:10.1021/nl049962k

[12] Li, X., Xu, Z.-H., & Wang, R. (2006). In situ observation of nanograin rotation and deformation in nacre. *Nano Letters, 6*(10), 2301-2304.

[13] Meyers, M. A., Lin, A. Y.-M., Chen, P.-Y., & Muyco, J. (2008). Mechanical strength of abalone nacre: Role of the soft organic layer. *Journal of the Mechanical Behavior of Biomedical Materials, 1*(1), 76-85.

[14] Ortiz, C., & Boyce, M. C. (2008). Bioinspired structural materials. *Science, 319*(5866), 1053-1054.

[15] Zhang, Z., Zhang, Y. W., & Gao, H. (2011). On optimal hierarchy of load-bearing biological materials. *Proceedings of the Royal Society of London B: Biological Sciences, 278*(1705), 519-525. doi:10.1098/rspb.2010.1093

[16] Liu, X., Li, J., Xiang, L., Sun, J., Zheng, G., Zhang, G., Wang, H., Xie, L., & Zhang, R. (2012). The role of matrix proteins in the control of nacreous layer deposition during pearl formation. *Proceedings of the Royal Society of London B: Biological Sciences, 279*(1730), 1000-1007. doi:10.1098/rspb.2011.1661

[17] Xu, L. P., Peng, J., Liu, Y., Wen, Y., Zhang, X., Jiang, L., & Wang, S. (2013). Nacre-inspired design of mechanical stable coating with underwater superoleophobicity. *ACS Nano, 7*(6), 5077-5083. doi:10.1021/nn400650f

[18] Shao, Y., Zhao, H. P., & Feng, X. Q. (2014). On flaw tolerance of nacre: A theoretical study. *Journal of the Royal Society Interface, 11*(92), 20131016. doi:10.1098/rsif.2013.1016

[19] Askarinejad, S., & Rahbar, N. (2015). Toughening mechanisms in bioinspired multilayered materials. *Journal of the Royal Society Interface, 12*(102), 20140855. doi:10.1098/rsif.2014.0855

[20] Barthelat, F., Yin, Z., & Buehler, M. J. (2016). Structure and mechanics of interfaces in biological materials. *Nature Reviews Materials, 1*, 16007.

[21] Gu, G. X., Libonati, F., Wettermark, S. D., & Buehler, M. J. (2017). Printing nature: Unraveling the role of nacre's mineral bridges. *Journal of the Mechanical Behavior of Biomedical Materials, 76*, 135-144. doi:10.1016/j.jmbbm.2017.05.007

[22] California, T. U. o. (2018, October 30, 2018). Haliotis rufescens. Retrieved from https://www.eeb.ucsc.edu/pacificrockyintertidal/target/target-species-haliotis-rufescens.html

[23] Life, E. o. Haliotis rufescens. Retrieved from https://eol.org/pages/620396

[24] Smith, B. L., Schaffer, T. E., Viani, M., Thompson, J. B., Frederick, N. A., Kindt, J., Belcher, A., Stucky, G. D., Morse, D. E., & Hansma, P. K. (1999). Molecular mechanistic origin of the toughness of natural adhesives, fibres and composites. *Nature, 399*(6738), 761-763. doi:10.1038/21607

[25] Song, F., Soh, A., & Bai, Y. (2003). Structural and mechanical properties of the organic matrix layers of nacre. *Biomaterials, 24*(20), 3623-3631.

[26] Meyers, M. A., Chen, P.-Y., Lin, A. Y.-M., & Seki, Y. (2008). Biological materials: Structure and mechanical properties. *Progress in Materials Science, 53*(1), 1-206.

[27] System, I. T. I. (2019). Haliotis rufescens-taxonomy and nomenclature. Retrieved from https://www.itis.gov/servlet/SingleRpt/SingleRpt?search_topic=TSN&search_value=69497

[28] Bevelander, G., & Nakahara, H. (1969). An electron microscope study of the formation of the nacreous layer in the shell of certain bivalve molluscs. *Calcified Tissue Research, 3*(1), 84-92.

[29] Schaffer, T. E., IonescuZanetti, C., Proksch, R., Fritz, M., Walters, D. A., Almqvist, N., Zaremba, C. M., Belcher, A. M., Smith, B. L., Stucky, G. D., Morse, D. E., & Hansma, P. K. (1997). Does abalone nacre form by heteroepitaxial nucleation or by growth through mineral bridges? *Chemistry of Materials, 9*(8), 1731-1740. doi:10.1021/cm960429i

[30] Zhang, A. (2017). The investigation of haliotis rufescens (red abalone): Mesolayer growth & mechanical behavior. *PhD Dissertation*.

[31] Su, X., Belcher, A. M., Zaremba, C. M., Morse, D. E., Stucky, G. D., & Heuer, A. H. (2002). Structural and microstructural characterization of the growth lines and prismatic microarchitecture in red abalone shell and the microstructures of abalone "flat pearls". *Chemistry of Materials, 14*(7), 3106-3117.

[32] Lin, A. Y., Chen, P. Y., & Meyers, M. A. (2008). The growth of nacre in the abalone shell. *Acta Biomaterialia, 4*(1), 131-138. doi:10.1016/j.actbio.2007.05.005

[33] Sumitomo, T., Kakisawa, H., & Kagawa, Y. (2011). Nanoscale structure and mechanical behavior of growth lines in shell of abalone haliotis gigantea. *Journal of Structural Biology, 174*(1), 31-36. doi:10.1016/j.jsb.2011.01.001

[34] Pomeroy, D. (2019). Abalone. Retrieved from https://eol.org/pages/620396/media

[35] Deville, S., Saiz, E., & Tomsia, A. P. (2007). Using ice to mimic nacre: From structural applications to artificial bone. *Handbook of Biomineralization:. Biomimetic bioinspired chemistry, 2*.

[36] Mineralogy-Mindat, H. I. o. (2019). Minerals. Retrieved from https://www.mindat.org/min-307.html

[37] Jackson, A., Vincent, J., & Turner, R. (1988). The mechanical design of nacre. *Proceedings of the Royal Society of London B: Biological Sciences, 234*(1277), 415-440.

[38] Ji, B. H., & Gao, H. J. (2004). Mechanical properties of nanostructure of biological materials. *Journal of the Mechanics and Physics of Solids, 52*(9), 1963-1990. doi:10.1016/j.jmps.2004.03.006

[39] Barthelat, F., & Espinosa, H. (2007). An experimental investigation of deformation and fracture of nacre–mother of pearl. *Experimental Mechanics, 47*(3), 311-324. doi:10.1007/s11340-007-9040-1

[40] Lin, A., & Meyers, M. A. (2005). Growth and structure in abalone shell. *Materials Science and Engineering a-Structural Materials Properties Microstructure and Processing, 390*(1-2), 27-41. doi:10.1016/j.msea.2004.06.072

[41] Barthelat, F., Tang, H., Zavattieri, P., Li, C.-M., & Espinosa, H. (2007). On the mechanics of mother-of-pearl: A key feature in the material hierarchical structure. *Journal of the Mechanics and Physics of Solids, 55*(2), 306-337.

[42] Wang, R. Z., Suo, Z., Evans, A. G., Yao, N., & Aksay, I. A. (2001). Deformation mechanisms in nacre. *Journal of Materials Research, 16*(9), 2485-2493. doi:Doi 10.1557/Jmr.2001.0340

[43] Evans, A., Suo, Z., Wang, R., Aksay, I., He, M., & Hutchinson, J. (2001). Model for the robust mechanical behavior of nacre. *Journal of Materials Research, 16*(09), 2475-2484.

[44] Barthelat, F., Li, C. M., Comi, C., & Espinosa, H. D. (2006). Mechanical properties of nacre constituents and their impact on mechanical performance. *Journal of Materials Research, 21*(8), 1977-1986. doi:10.1557/Jmr.2006.0239

[45] Fan, S., & Yilong, B. (2001). Mineral bridges of nacre and its effects. *Acta Mechanica Sinica, 17*(3), 251.

[46] Song, F., Zhang, X., & Bai, Y. (2002). Microstructure and characteristics in the organic matrix layers of nacre. *Journal of Materials Research, 17*(7), 1567-1570.

[47] Gunnison, K. E., Sarikaya, M., Liu, J., & Aksay, I. A. (1991). Structure-mechanical property relationships in a biological ceramic-polymer composite: Nacre. *MRS Online Proceedings Library Archive, 255*.

[48] Barthelat, F., Tang, H., Zavattieri, P. D., Li, C. M., & Espinosa, H. D. (2007). On the mechanics of mother-of-pearl: A key feature in the material hierarchical structure. *Journal of the Mechanics and Physics of Solids, 55*(2), 306-337. doi:10.1016/j.jmps.2006.07.007

[49] Okumura, K., & De Gennes, P.-G. (2001). Why is nacre strong? Elastic theory and fracture mechanics for biocomposites with stratified structures. *The European Physical Journal E, 4*(1), 121-127.

[50] Bruet, B., Qi, H., Boyce, M., Panas, R., Tai, K., Frick, L., & Ortiz, C. (2005). Nanoscale morphology and indentation of individual nacre tablets from the gastropod mollusc trochus niloticus. *Journal of Materials Research, 20*(09), 2400-2419.

[51] Katti, K. S., Katti, D. R., Pradhan, S. M., & Bhosle, A. (2005). Platelet interlocks are the key to toughness and strength in nacre. *Journal of Materials Research, 20*(5), 1097-1100.

[52] Zentz, F., Bedouet, L., Almeida, M. J., Milet, C., Lopez, E., & Giraud, M. (2001). Characterization and quantification of chitosan extracted from nacre of the abalone haliotis tuberculata and the oyster pinctada maxima. *Marine Biotechnology, 3*(1), 36-44. doi:10.1007/s101260000042

[53] Dubey, D. K., & Tomar, V. (2010). Role of molecular level interfacial forces in hard biomaterial mechanics: A review. *Annals of Biomedical Engineering, 38*(6), 2040-2055. doi:10.1007/s10439-010-9988-3

[54] Launspach, M., Rückmann, K., Gummich, M., Rademaker, H., Doschke, H., Radmacher, M., & Fritz, M. (2012). Immobilisation and characterisation of the demineralised, fully hydrated organic matrix of nacre–an atomic force microscopy study. *Micron, 43*(12), 1351-1363. doi:10.1016/j.micron.2012.03.014

[55] Verma, D., Katti, K., & Katti, D. (2007). Nature of water in nacre: A 2d fourier transform infrared spectroscopic study. *Spectrochimica Acta Part A: Molecular and Biomolecular Spectroscopy, 67*(3-4), 784-788. doi:10.1016/j.saa.2006.08.033

[56] Shen, X., Belcher, A. M., Hansma, P. K., Stucky, G. D., & Morse, D. E. (1997). Molecular cloning and characterization of lustrin a, a matrix protein from shell and pearl nacre of haliotis rufescens. *Journal of Biological Chemistry, 272*(51), 32472-32481.

[57] Sumitomo, T., Kakisawa, H., Owaki, Y., & Kagawa, Y. (2008). In situ transmission electron microscopy observation of reversible deformation in nacre organic matrix. *Journal of Materials Research, 23*(5), 1466-1471.

[58] Ghosh, P., Katti, D. R., & Katti, K. S. (2007). Mineral proximity influences mechanical response of proteins in biological mineral-protein hybrid systems. *Biomacromolecules, 8*(3), 851-856. doi:10.1021/bm060942h

[59] Barthelat, F., Li, C.-M., Comi, C., & Espinosa, H. D. (2006). Mechanical properties of nacre constituents and their impact on mechanical performance. *Journal of Materials Research, 21*(08), 1977-1986.

[60] Wang, R., Suo, Z., Evans, A., Yao, N., & Aksay, I. (2001). Deformation mechanisms in nacre. *Journal of Materials Research, 16*(09), 2485-2493.

[61] Meyers, M. A., Lin, A. Y., Chen, P. Y., & Muyco, J. (2008). Mechanical strength of abalone nacre: Role of the soft organic layer. *Journal of the Mechanical Behavior of Biomedical Materials, 1*(1), 76-85. doi:10.1016/j.jmbbm.2007.03.001

[62] Checa, A. G., Cartwright, J. H., & Willinger, M. G. (2011). Mineral bridges in nacre. *Journal of Structural Biology, 176*(3), 330-339. doi:10.1016/j.jsb.2011.09.011

[63] Song, F., Zhou, J., Xu, X., Xu, Y., & Bai, Y. (2008). Effect of a negative poisson ratio in the tension of ceramics. *Physical Review Letters, 100*(24), 245502.

[64] Verho, T., Karppinen, P., Groschel, A. H., & Ikkala, O. (2018). Imaging inelastic fracture processes in biomimetic nanocomposites and nacre by laser speckle for better toughness. *Advanced Sciences, 5*(1), 1700635. doi:10.1002/advs.201700635

[65] Menig, R., Meyers, M. H., Meyers, M. A., & Vecchio, K. S. (2000). Quasi-static and dynamic mechanical response of haliotis rufescens (abalone) shells. *Acta Materialia, 48*(9), 2383-2398. doi:Doi 10.1016/S1359-6454(99)00443-7

[66] Lin, A. Y.-M., & Meyers, M. A. (2009). Interfacial shear strength in abalone nacre. *Journal of the Mechanical Behavior of Biomedical Materials, 2*(6), 607-612.

[67] Menig, R., Meyers, M., Meyers, M., & Vecchio, K. (2000). Quasi-static and dynamic mechanical response of haliotis rufescens (abalone) shells. *Acta Materialia, 48*(9), 2383-2398.

[68] Richter, B. I., Kellner, S., Menzel, H., Behrens, P., Denkena, B., Ostermeier, S., & Hurschler, C. (2011). Mechanical characterization of nacre as an ideal-model for innovative new endoprosthesis materials. *Archives of Orthopaedic and Trauma Surgery, 131*(2), 191-196. doi:10.1007/s00402-010-1118-z

[69] Kotha, S., Li, Y., & Guzelsu, N. (2001). Micromechanical model of nacre tested in tension. *Journal of Materials Science, 36*(8).

[70] Bertoldi, K., Bigoni, D., & Drugan, W. (2008). Nacre: An orthotropic and bimodular elastic material. *Composites Science and Technology, 68*(6), 1363-1375.

[71] Katti, D. R., Katti, K. S., Sopp, J. M., & Sarikaya, M. (2001). 3d finite element modeling of mechanical response in nacre-based hybrid nanocomposites. *Computational and Theoretical Polymer Science, 11*(5), 397-404. doi:Doi 10.1016/S1089-3156(01)00012-5

[72] Dashkovskiy, S., Suhr, B., Tushtev, K., & Grathwohl, G. (2007). Nacre properties in the elastic range: Influence of matrix incompressibility. *Computational Materials Science, 41*(1), 96-106.

[73] Lin, A. Y.-M., Chen, P.-Y., & Meyers, M. A. (2008). The growth of nacre in the abalone shell. *Acta Biomaterialia, 4*(1), 131-138.

[74] Weiner, S., & Traub, W. (1984). Macromolecules in mollusc shells and their functions in biomineralization. *Philosophical Transactions of the Royal Society B, 304*(1121), 425-434.

[75] Belcher, A. M., Wu, X. H., Christensen, R. J., Hansma, P. K., Stucky, G. D., & Morse, D. E. (1996). Control of crystal phase switching and orientation by soluble mollusc-shell proteins. *Nature, 381*(6577), 56-58. doi:DOI 10.1038/381056a0

[76] Feng, Q. L., Pu, G., Pei, Y., Cui, F. Z., Li, H. D., & Kim, T. N. (2000). Polymorph and morphology of calcium carbonate crystals induced by proteins extracted from mollusk shell. *Journal of Crystal Growth, 216*(1-4), 459-465. doi:Doi 10.1016/S0022-0248(00)00396-1

[77] Thompson, J. B., Paloczi, G. T., Kindt, J. H., Michenfelder, M., Smith, B. L., Stucky, G., Morse, D. E., & Hansma, P. K. (2000). Direct observation of the transition from calcite to aragonite growth as induced by abalone shell proteins. *Biophysical Journal, 79*(6), 3307-3312. doi:Doi 10.1016/S0006-3495(00)76562-3

[78] Addadi, L., Joester, D., Nudelman, F., & Weiner, S. (2006). Mollusk shell formation: A source of new concepts for understanding biomineralization processes. *Chemistry, 12*(4), 980-987. doi:10.1002/chem.200500980

[79] Nudelman, F., Gotliv, B. A., Addadi, L., & Weiner, S. (2006). Mollusk shell formation: Mapping the distribution of organic matrix components underlying a single aragonitic tablet in nacre. *Journal of Structural Biology, 153*(2), 176-187. doi:10.1016/j.jsb.2005.09.009

[80] Cartwright, J. H., & Checa, A. G. (2007). The dynamics of nacre self-assembly. *Journal of the Royal Society Interface, 4*(14), 491-504. doi:10.1098/rsif.2006.0188

[81] Gilbert, P. U., Metzler, R. A., Zhou, D., Scholl, A., Doran, A., Young, A., Kunz, M., Tamura, N., & Coppersmith, S. N. (2008). Gradual ordering in red abalone nacre. *Journal of the American Chemical Society, 130*(51), 17519-17527. doi:10.1021/ja8065495

[82] Suzuki, M., Saruwatari, K., Kogure, T., Yamamoto, Y., Nishimura, T., Kato, T., & Nagasawa, H. (2009). An acidic matrix protein, pif, is a key macromolecule for nacre formation. *Science, 325*(5946), 1388-1390. doi:10.1126/science.1173793

[83] Nudelman, F. (2015). *Nacre biomineralisation: A review on the mechanisms of crystal nucleation.* Paper presented at the Seminars in Cell & Developmental Biology.

[84] Checa, A. G., & Rodriguez-Navarro, A. B. (2005). Self-organisation of nacre in the shells of pterioida (bivalvia: Mollusca). *Biomaterials, 26*(9), 1071-1079. doi:10.1016/j.biomaterials.2004.04.007

[85] Dauphin, Y., Ball, A. D., Cotte, M., Cuif, J.-P., Meibom, A., Salomé, M., Susini, J., & Williams, C. T. (2008). Structure and composition of the nacre–prisms transition in the shell of pinctada margaritifera (mollusca, bivalvia). *Analytical and Bioanalytical Chemistry, 390*(6), 1659-1669.

[86] Griesshaber, E., Schmahl, W. W., Ubhi, H. S., Huber, J., Nindiyasari, F., Maier, B., & Ziegler, A. (2013). Homoepitaxial meso- and microscale crystal co-orientation and organic matrix network structure in mytilus edulis nacre and calcite. *Acta Biomaterialia, 9*(12), 9492-9502. doi:10.1016/j.actbio.2013.07.020

[87] Hovden, R., Wolf, S. E., Holtz, M. E., Marin, F., Muller, D. A., & Estroff, L. A. (2015). Nanoscale assembly processes revealed in the nacroprismatic transition zone of pinna nobilis mollusc shells. *Nature Communications, 6*, 10097. doi:10.1038/ncomms10097

[88] Metzler, R. A., Abrecht, M., Olabisi, R. M., Ariosa, D., Johnson, C. J., Frazer, B. H., Coppersmith, S. N., & Gilbert, P. U. (2007). Architecture of columnar nacre, and implications for its formation mechanism. *Physical Review Letters, 98*(26), 268102. doi:10.1103/PhysRevLett.98.268102

[89] Freer, A., Greenwood, D., Chung, P., Pannell, C. L., & Cusack, M. (2009). Aragonite prism− nacre interface in freshwater mussels anodonta anatina (linnaeus, 1758) and anodonta cygnea (l. 1758). *Crystal Growth & Design, 10*(1), 344-347.

[90] Erasmus, J., Cook, P. A., & Sweijd, N. (1994). Internal shell structure and growth lines in the shell of the abalone, haliotis-midae. *Journal of Shellfish Research, 13*(2), 493-501.

[91] Shepherd, S. A., Alwahaibi, D., & Alazri, A. R. (1995). Shell growth checks and growth of the omani abalone haliotis-mariae. *Marine and Freshwater Research, 46*(3), 575-582. doi:Doi 10.1071/Mf9950575

[92] Falini, G., Sartor, G., Fabbri, D., Vergni, P., Fermani, S., Belcher, A. M., Stucky, G. D., & Morse, D. E. (2011). The interstitial crystal-nucleating sheet in molluscan haliotis rufescens shell: A bio-polymeric composite. *Journal of Structural Biology, 173*(1), 128-137. doi:10.1016/j.jsb.2010.08.002

[93] Lopez, M., Chen, P., McKittrick, J., & Meyers, M. (2011). Growth of nacre in abalone: Seasonal and feeding effects. *Materials Science and Engineering: C, 31*(2), 238-245.

[94] Sullivan, M., & Prorok, B. C. (2014). New insight into the toughening mechanisms of nacre. In *Mechanics of biological systems and materials, volume 4* (pp. 93-98): Springer.

[95] Lopez, M. I., Meza Martinez, P. E., & Meyers, M. A. (2014). Organic interlamellar layers, mesolayers and mineral nanobridges: Contribution to

strength in abalone (haliotis rufescence) nacre. *Acta Biomaterialia, 10*(5), 2056-2064. doi:10.1016/j.actbio.2013.12.016

[96] Katti, D., Katti, K., Sopp, J., & Sarikaya, M. (2001). 3d finite element modeling of mechanical response in nacre-based hybrid nanocomposites. *Computational and Theoretical Polymer Science, 11*(5), 397-404.

[97] Wang, J., Liu, K., & Joshi, G. (2002). *Using torsion bar testing to determine fracture toughness of ceramic materials.* Paper presented at the ASME 2002 Engineering Technology Conference on Energy.

[98] Tan, T., Ren, F., Wang, J. J. A., Lara-Curzio, E., Agastra, P., Mandell, J., Bertelsen, W. D., & LaFrance, C. M. (2013). Investigating fracture behavior of polymer and polymeric composite materials using spiral notch torsion test. *Engineering Fracture Mechanics, 101*, 109-128. doi:10.1016/j.engfracmech.2012.07.007

[99] Radmacherf, M., Waltersf, D. A., Hansmaf, P. K., & Stucky, G. D. (1994). Flat pearls from biofabrication of organized composites on inorganic substrates. *Nature, 371*, 1.

[100] Yao, N., Epstein, A. K., Liu, W. W., Sauer, F., & Yang, N. (2009). Organic–inorganic interfaces and spiral growth in nacre. *Journal of the Royal Society Interface, 6*(33), 367-376.

[101] Hendry, J. P., Perkins, W. T., & Bane, T. (2001). Short-term environmental change in a jurassic lagoon deduced from geochemical trends in aragonite bivalve shells. *Geological Society of America Bulletin, 113*(6), 790-798.

[102] Espinosa, H. D., Juster, A. L., Latourte, F. J., Loh, O. Y., Gregoire, D., & Zavattieri, P. D. (2011). Tablet-level origin of toughening in abalone shells and translation to synthetic composite materials. *Nature Communications, 2*, 173.

[103] Shao, Y., Zhao, H. P., Feng, X. Q., & Gao, H. J. (2012). Discontinuous crack-bridging model for fracture toughness analysis of nacre. *Journal of the Mechanics and Physics of Solids, 60*(8), 1400-1419. doi:10.1016/j.jmps.2012.04.011

[104] Huang, Z., Li, H., Pan, Z., Wei, Q., Chao, Y. J., & Li, X. (2011). Uncovering high-strain rate protection mechanism in nacre. *Scientific Reports, 1*, 148.

[105] Wachtman, J. B., Cannon, W. R., & Matthewson, M. J. (2009). *Mechanical properties of ceramics*: John Wiley & Sons.

[106] Fanshawe, S., Vanblaricom, G. R., & Shelly, A. A. (2003). Restored top carnivores as detriments to the performance of marine protected areas intended for fishery sustainability: A case study with red abalones and sea otters. *Conservation Biology, 17*(1), 273-283.

[107] Tan, T., Ren, F., Wang, J. J.-A., Lara-Curzio, E., Agastra, P., Mandell, J., Bertelsen, W. D., & LaFrance, C. M. (2013). Investigating fracture behavior of polymer and polymeric composite materials using spiral notch torsion test. *Engineering Fracture Mechanics, 101*, 109-128.

[108] Wang, J. J.-A., Ren, F., Tan, T., & Liu, K. (2015). The development of in situ fracture toughness evaluation techniques in hydrogen environment. *International Journal of Hydrogen Energy, 40*(4), 2013-2024. doi:10.1016/j.ijhydene.2014.11.147

[109] Zhou, H., Li, X., Wang, Y., Liu, Z., Yang, W., & Gao, H. (2015). Torsional detwinning domino in nanotwinned one-dimensional nanostructures. *Nano Letters, 15*(9), 6082-6087. doi:10.1021/acs.nanolett.5b02330

[110] Gershenfeld, N. A. (1999). *The nature of mathematical modeling*: Cambridge university press.

[111] Antonaglia, J., Wright, W. J., Gu, X., Byer, R. R., Hufnagel, T. C., LeBlanc, M., Uhl, J. T., & Dahmen, K. A. (2014). Bulk metallic glasses deform via slip avalanches. *Physical Review Letters, 112*(15), 155501.

[112] Alghamdi, S., Du, F., Yang, J., Tan, T., (2018). The role of water in the initial sliding of nacreous tablets: Findings from the torsional fracture of dry and hydrated nacre. *Journal of Mechanical Behavior of Biomedical Materials*, 88, 322-329.

[113] Alghamdi, S., Tan, T., Hale-Sills, C., Vilmont, F., Xia, T., Yang, J., Huston, D., Dewoolkar, M., (2017). Catastrophic failure of nacre under pure shear stresses of torsion. *Scientfic Reports*, 7, 13123.

[114] Alghamdi, S.J., (2016). A Preliminary Study on the interfacial strength of red abalone. *Master's thesis*. University of Vermont.

Appendix A

The experimental system

A schematic diagram of the experimental system used in the study is shown below. It includes the coupled load cells, data acquisition systems, and specimens.

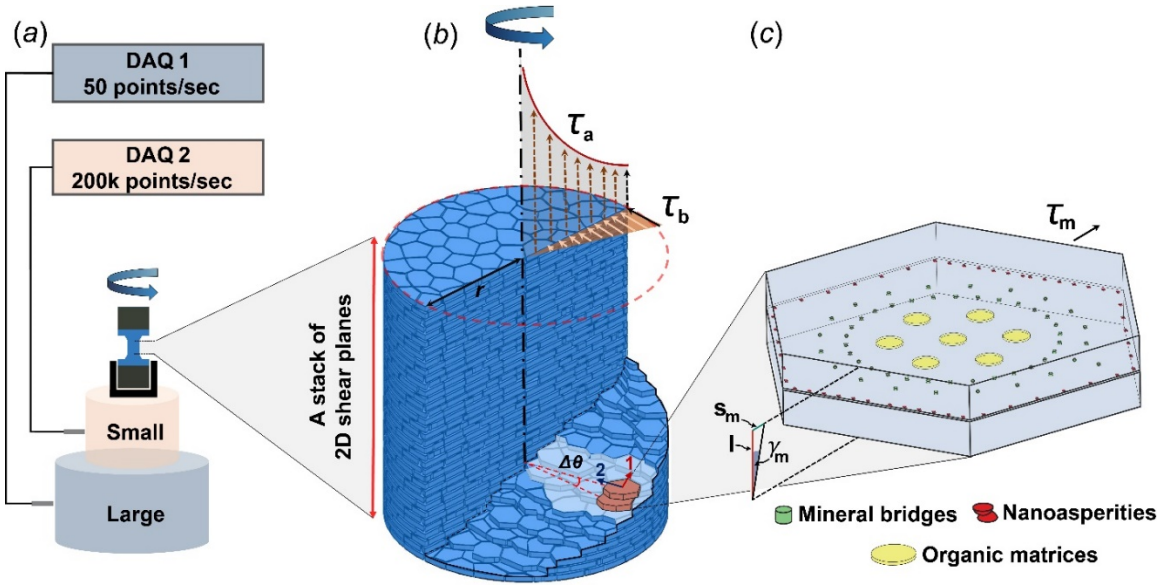

Figure S1. Illustration of the experimental system. (a) the coupled system with a large axial-torsional load cell (50 data points per second) and a small torsional load cell (200,000 data points per second). (b) A schematic diagram of the pure shear stresses of torsion before (τ_b) and after (τ_a) the failure of nacre specimens. s_m, γ_m and l are the surface sliding distance, surface shear strain, and the height of adjacent tablets, respectively. The blue background of the nacreous gauge section denotes a hydrated nacre specimen. Arrows 1 and 2 denote the sliding and crack directions, respectively. (c) A detail view of two nacreous tablets on the cylindrical surface sliding over each other under the surface shear stress (τ_m).

Rotations of the gauge section

The rotation of the gauge section was calculated by subtracting rotations from the fillets and the small load cell from the total rotation measured, which is given by

$$\theta_g = \theta_{mear} - \left(\theta_s + 2\theta_f\right) \tag{S1}$$

$$\theta_f = \frac{2T}{\pi G} \int_0^{\varphi_0} R_f \cdot \cos\varphi \cdot \left(R_f + r - R_f \cdot \cos\varphi\right)^{-4} d\varphi \tag{S2}$$

Where θ_g is the rotation angle of the gauge section, θ_{mear} is the total rotation angle measured, θ_s is the rotation angle of the small load cell, θ_f is the rotation angle of the fillet, T is torque, G is the shear modulus, φ_0 is the angle of the fillet, r is the gauge section radius, and R_f is the fillet radius. Equation S2 is obtained from the references (Liu, 2004; Song et al., 2017). By applying the same series of torque ranging from 0 to 0.8 Nm, twisting angles in the elastic range of an aluminum sample with a 12.7 mm-diameter gauge section were measured using the large load cell only, and then using both the small and large load cells. The rotation differences were used to establish the torque-rotation relation of the small load cell. Results show that the twisting angle of the gauge section is ~92% of the total rotation measured.

Wiener filtering of the high sampling rate data

Wiener deconvolution filter was used to remove the noise of the stress-strain curves collected at 200,000 points per second. The filter minimizes the differences between the observed and the true signals (Gershenfeld, 1999). In the frequency domain, the wiener deconvolution is given by:

$$V_T(\omega) = \frac{V_E(\omega)}{H(\omega)} \frac{|S(\omega)|^2}{|S(\omega)|^2 + |N(\omega)|^2}$$

(S3)

where, $V_T(\omega)$ is the filtered signal, $V_E(\omega)$ is the recorded signal, $H(\omega)$ is the impulse response function of the experimental system, $S(\omega)$ is a theoretical prediction for the true signal, and $N(\omega)$ is the noise.(Antonaglia et al., 2014)

Mathematical modeling of stress-strain curves in dry nacre

Results from the finite element modeling are shown below, including the comparison between model predictions and experimental measurements, and the stress contours of mineral bridges, nanoasperities and organic matrices.

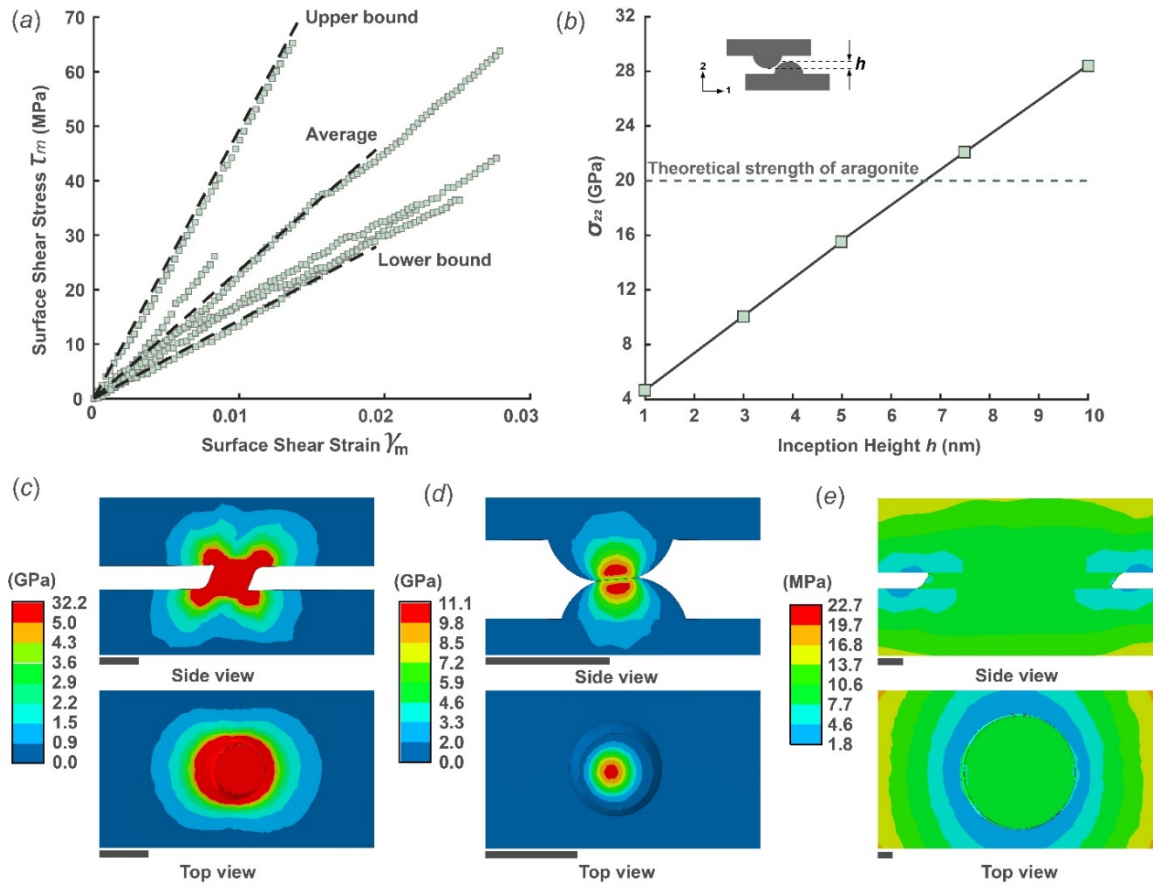

Figure S2: (a) Shear stress-strain curves of dry nacre specimens and estimations from the finite element models. (b) Inception height *h* and the contact stresses. Side and top views of stress contours in (c) A mineral bridge. (d) A pair of contacted nanoasperities. (e) An organic matrix cylinder. Scale bars are 50 nm in c, d and e.

Statistics of bumps in the hydrated nacre

The raw data of a representative hydrated specimen collected at 200,000 data points per second was illustrated in the frequency domain. Complementary cumulative distribution functions of bump sizes and distances were shown for all hydrated nacre specimens.

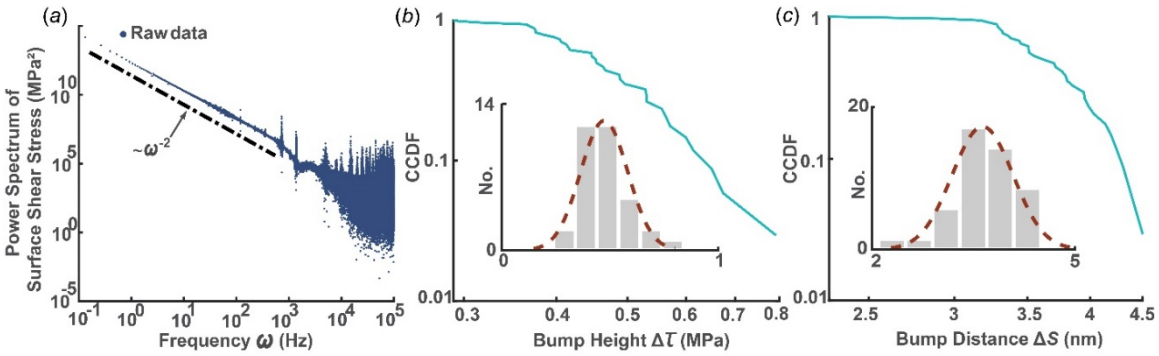

Figure S3: (a) The power spectrum of surface shear stress (τ_m) in the frequency domain included a scaling regime that is $\sim\omega^{-2}$. Complementary cumulative distribution functions (CCDF) of (b) bump heights and (c) bump distances for all hydrated nacre specimens.

Fractural patterns of dry and hydrated nacre

A summary of the fractural pattern of different materials is listed in Table S1. Fracture of isotropic materials under torsion exhibit ~0° flat surfaces in ductile materials and ~45° fractural surface in brittle materials. In this study, the direction of the torsional load is perpendicular to the layers of nacreous tablets. Dry nacre exhibits ~0° flat surfaces with minimized plasticity, whereas hydrated nacre exhibits ~45° flat surfaces with substantial plasticity.

Table S1: A summary of the fractural patterns in different materials under torsion.

	Isotropic, *ductile*	Isotropic, *brittle*	Dry Nacre, *brittle*, Transversely isotropic	Hydrated Nacre, *ductile*, Transversely isotropic
Torsion	~0°	~45°	~0°	~45°

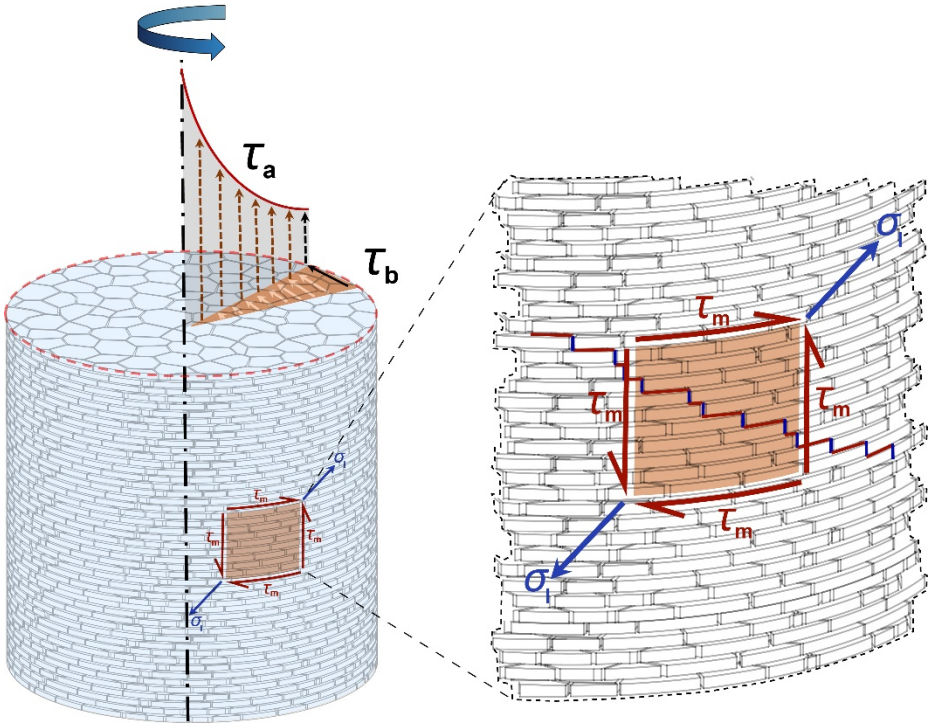

Figure S4: A schematic diagram of the fracture pattern of hydrated nacre. When the interface of surface tablets fails, the retardation of stress distributions resulting from the hydrogen bonds promotes the kinking of cracks to neighbor interfaces due to the principle tensile stresses $\boldsymbol{\sigma_I}$ on the surface. The competition between surface cracks and radial cracks leads to the spiral fracture inside the brick-and-mortar structure of hydrated nacre.

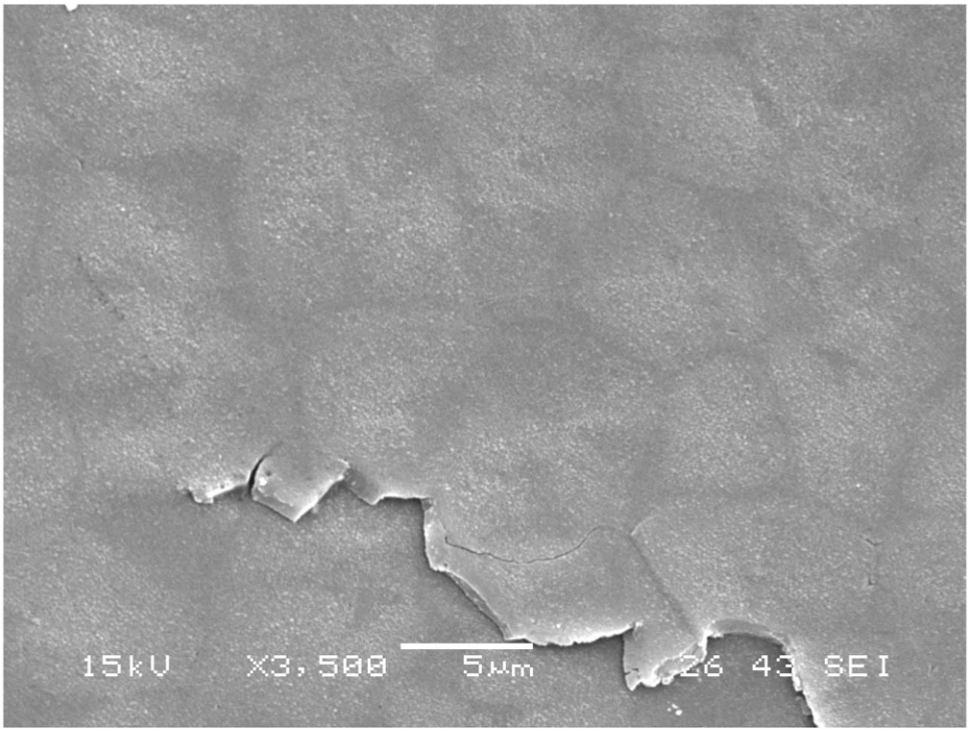

Figure S5: Spiral connections between nacreous tablets on the fracture surface of a dry nacre specimen.

Appendix A. References

[1] Antonaglia, J., Wright, W.J., Gu, X., Byer, R.R., Hufnagel, T.C., LeBlanc, M., Uhl, J.T., Dahmen, K.A., (2014). Bulk metallic glasses deform via slip avalanches. *Physical Reveiw Letters 112*, 155501.

[2] Gershenfeld, N.A., 1999. The nature of mathematical modeling. Cambridge university press.

[3] Liu, S.M., (2004). Multiaxial Fatigue of LY12 and LC4 Aluminum Alloy and Cyclic Deformation of Equal-channel Angular Pressed 8090 Al-Li Alloy. *Institute of Metal Research Chinese Academy of Science.*

[4] Song, Z.-Q., Ma, E., Xu, J., (2017). Failure of Zr 61 Ti 2 Cu 25 Al 12 bulk metallic glass under torsional loading. *Intermetallics 86*, 25-32.

Appendix B

Table S2: Dimensions of torsional and tensile samples. Units are in millimeter.

Cylindrical cross sections (Diameter: mm)				
	Composite		Pure nacre	
	Dry	Hydrated	Dry	Hydrated
Torsion	2.3 ± 0.1	3.0 ± 0.4	3.0 ± 0.0	2.6 ± 0.2
Tension	2.5 ± 0.4	2. 7 ± 0.1		

Rectangular cross sections (Width and Thickness: mm)			
		Pure nacre	
Tension	Width	1.9 ± 0.2	1.7 ± 0.4
	Thickness	1.4 ± 0.2	0.9 ± 0.0

Table S3: Replica numbers in each test.

	Composite		Pure nacre	
	Dry	Hydrated	Dry	Hydrated
Torsion	3	3	6	3
Tension	3	3	3	3

Table S4: The presence of bumps in stress-strain curves.

	Composite		Pure nacre	
	Dry	Wet	Dry	Wet
Torsion	No	No	No	Yes
Tension	Yes	Yes	Yes	Yes

Table S5: Summary of fracture surfaces relative to the cross-sectional plane.

	Composite		Pure nacre	
	Dry	Hydrated	Dry	Hydrated
Torsion	~0°	~0°	~0°	~36.0 ± 3.8°
Tension	~0°	~0°	11.4 ± 0.5°	2.3 ± 0.2°

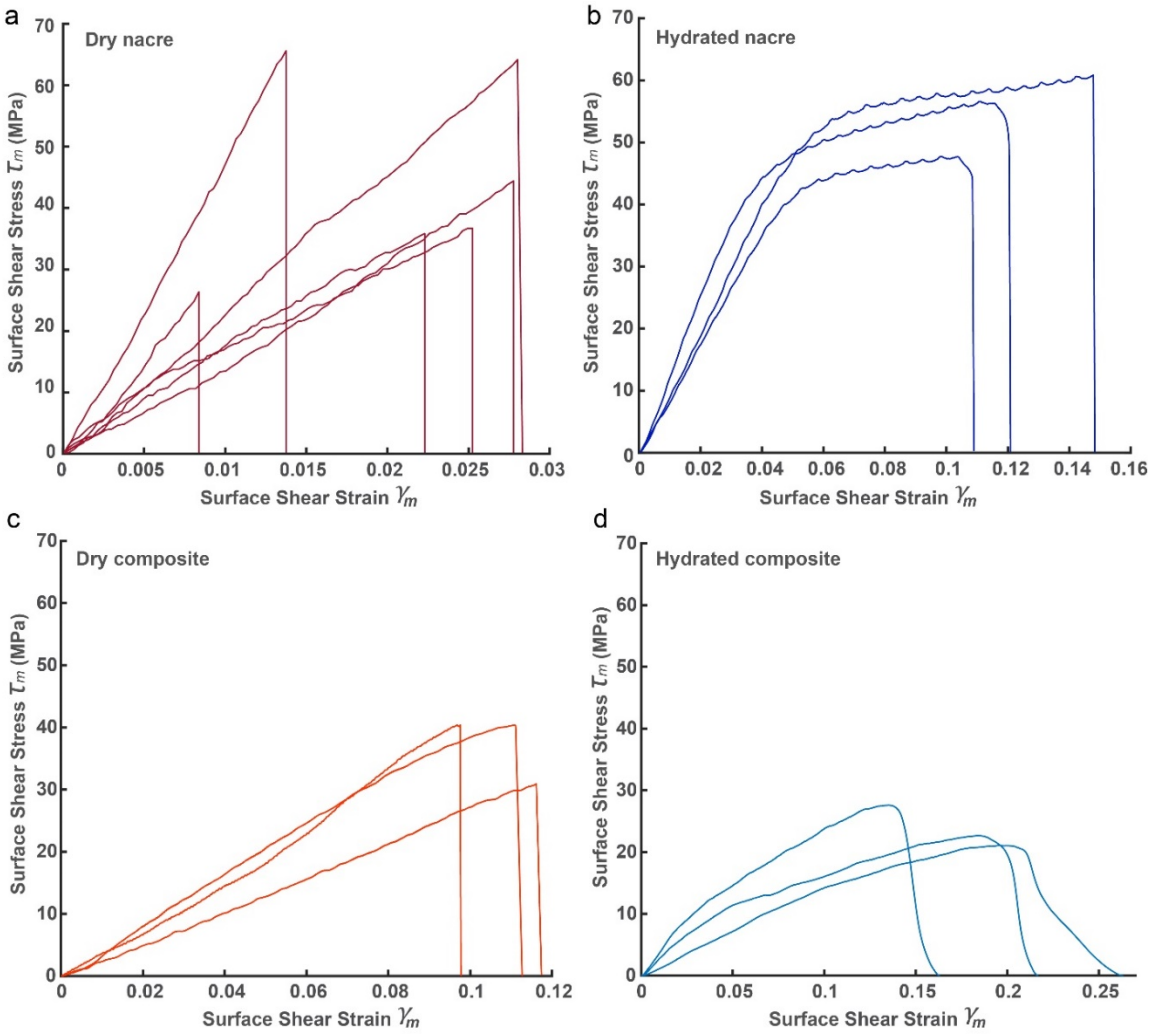

Figure S6: Filtered surface shear stress - surface shear strain curves for nacre and composite samples under dry and hydrated conditions.

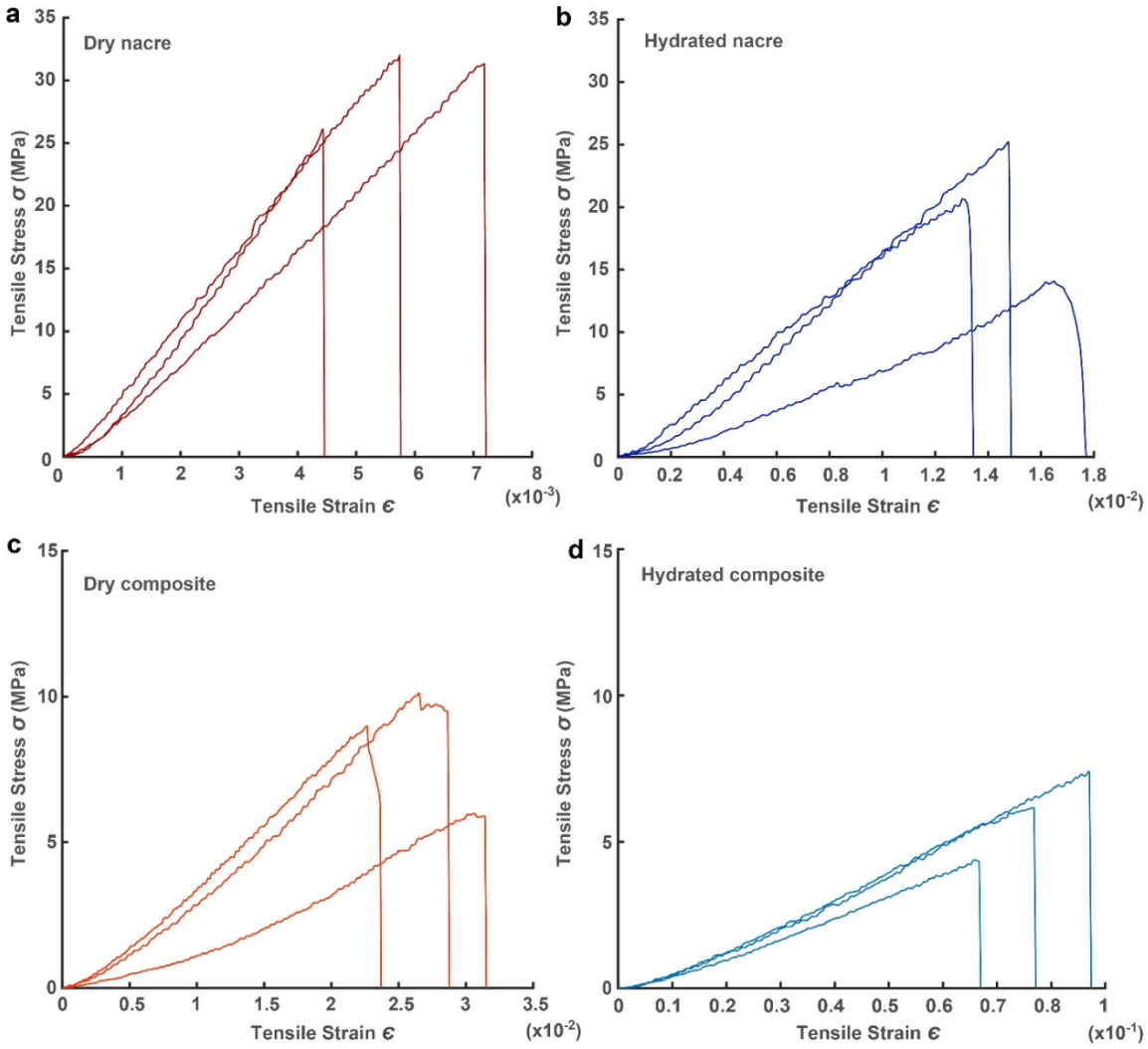

Figure S7: Filtered tensile stress-strain curves nacre and composite samples under dry and hydrated conditions.

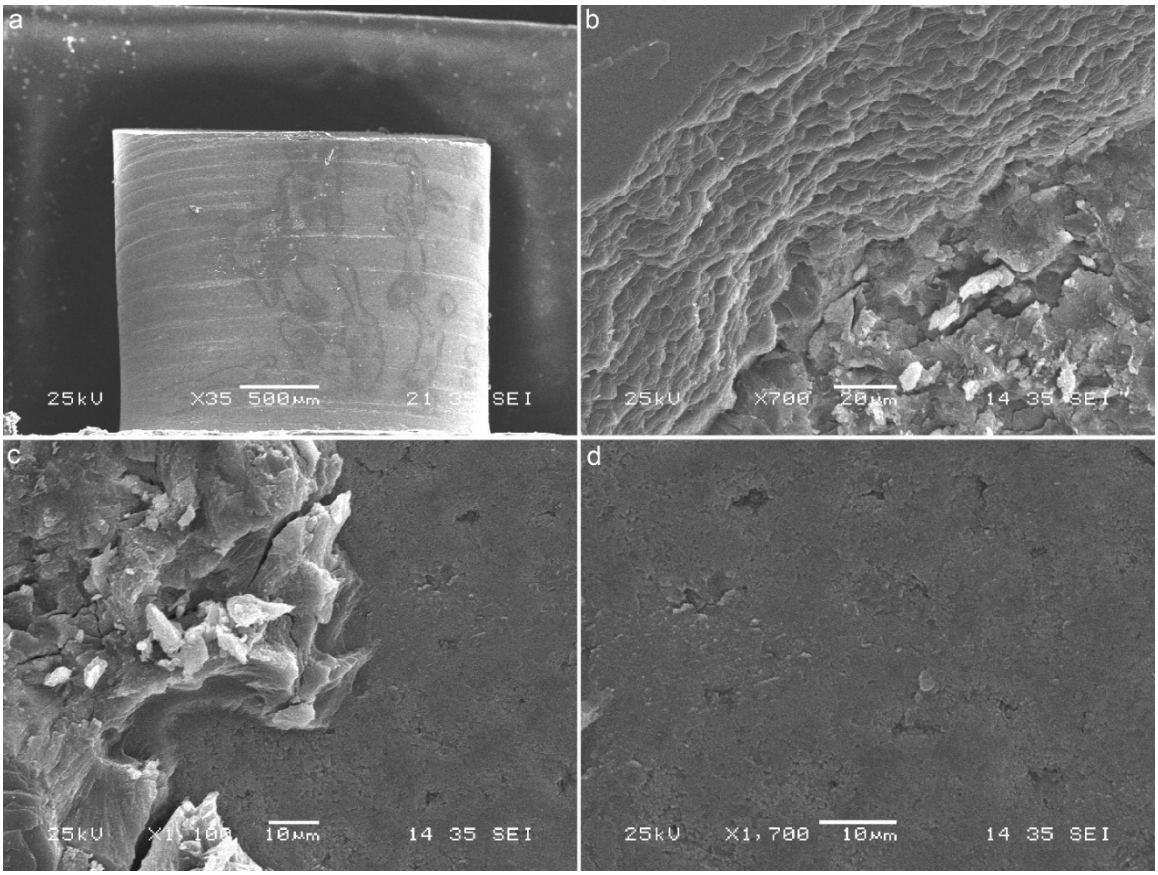

Figure S8: Fractural surfaces of dry composite specimen under monotonic torsion. (a) Side view of the fractured sample. (b) Transition from nacre to broken spherulites. (c) Transition from broken spherulites to green matrix. (d) a close view of the green matrix.

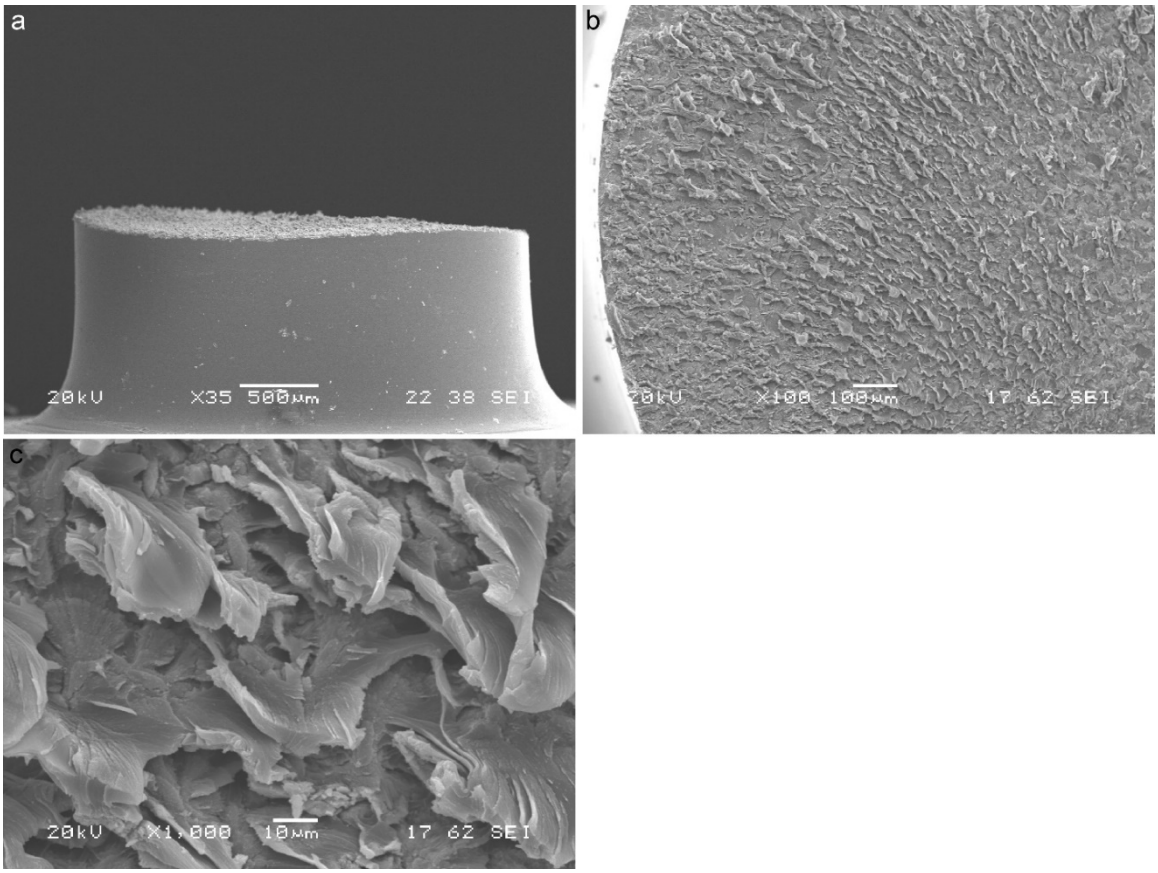

Figure S9: Fractural surfaces of hydrated composite specimen under monotonic torsion. (a) Side view of the fractured sample. (b) Sheared spherulites indicate the crack propagation direction. (c) Top view of the sheared spherulites in the fractured hydrated composite specimen.

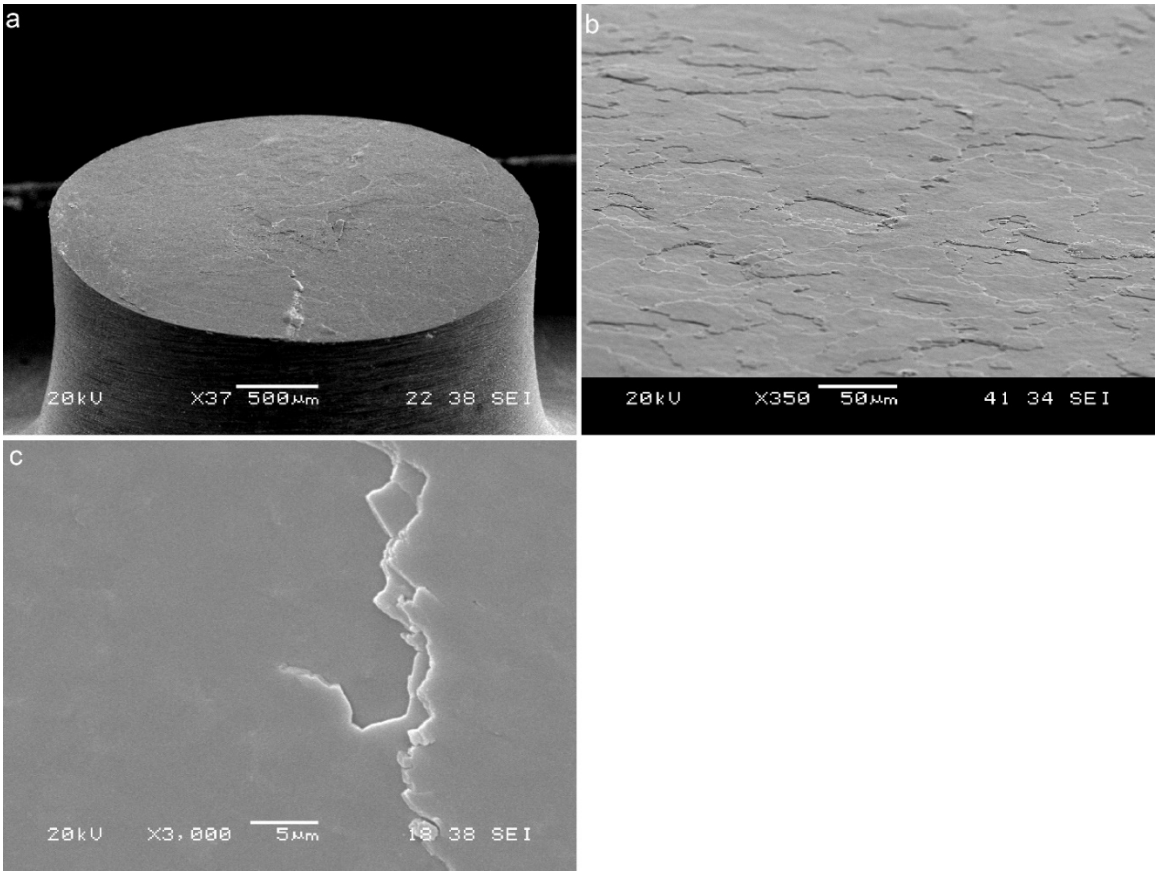

Figure S10: Fractural surfaces of dry pure nacre samples under monotonic torsion. (a) Side view of the fractured sample. (b) An aerial view of the fracture surface showing the flat fracture surface relative to the cylindrical axis. (c) A detailed view exhibited the spiral connections between successive layers on the flat fractural surface. (a) and (b) were adapted from Alghamdi et al. 2018 [1]

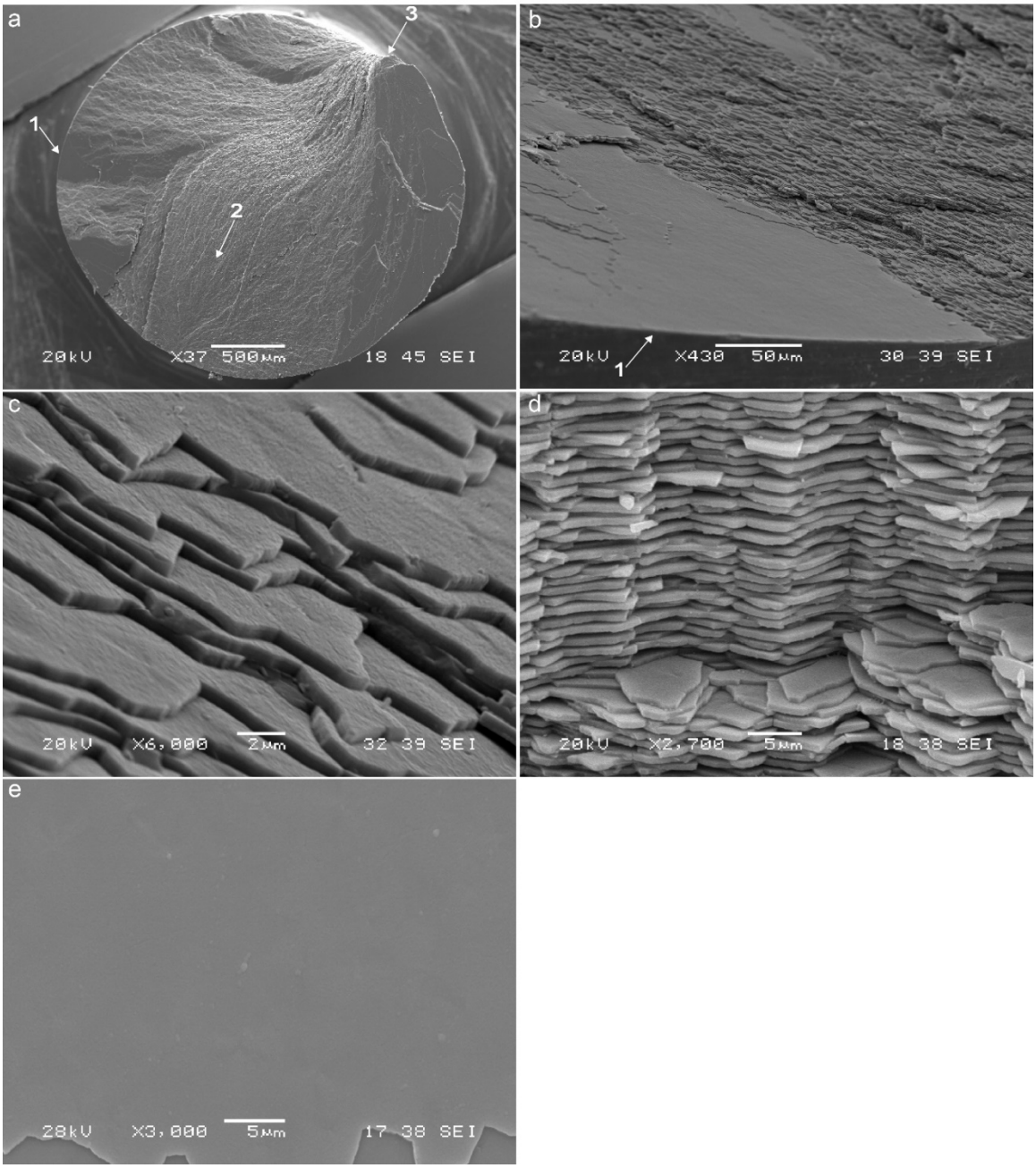

Figure S11: Fractural surfaces of hydrated pure nacre under monotonic torsion. (a) Top view of the spiral fractural surfaces of a hydrated nacre specimen. Arrows point to different morphologies of the exposed nacreous tablets after fracture. (b) The transition from a flat tablet surface at the external edge to tablet stair, (c) the ramped tablet stairs pointed by arrow 2. (d) The staggered tablet cliff pointed by arrow 3 are all observed on the fractural surfaces of the hydrated nacre. (e) A closer look at the flat tablet surface pointed by arrow 1. Adapted from Alghamdi et al. 2018 [1].

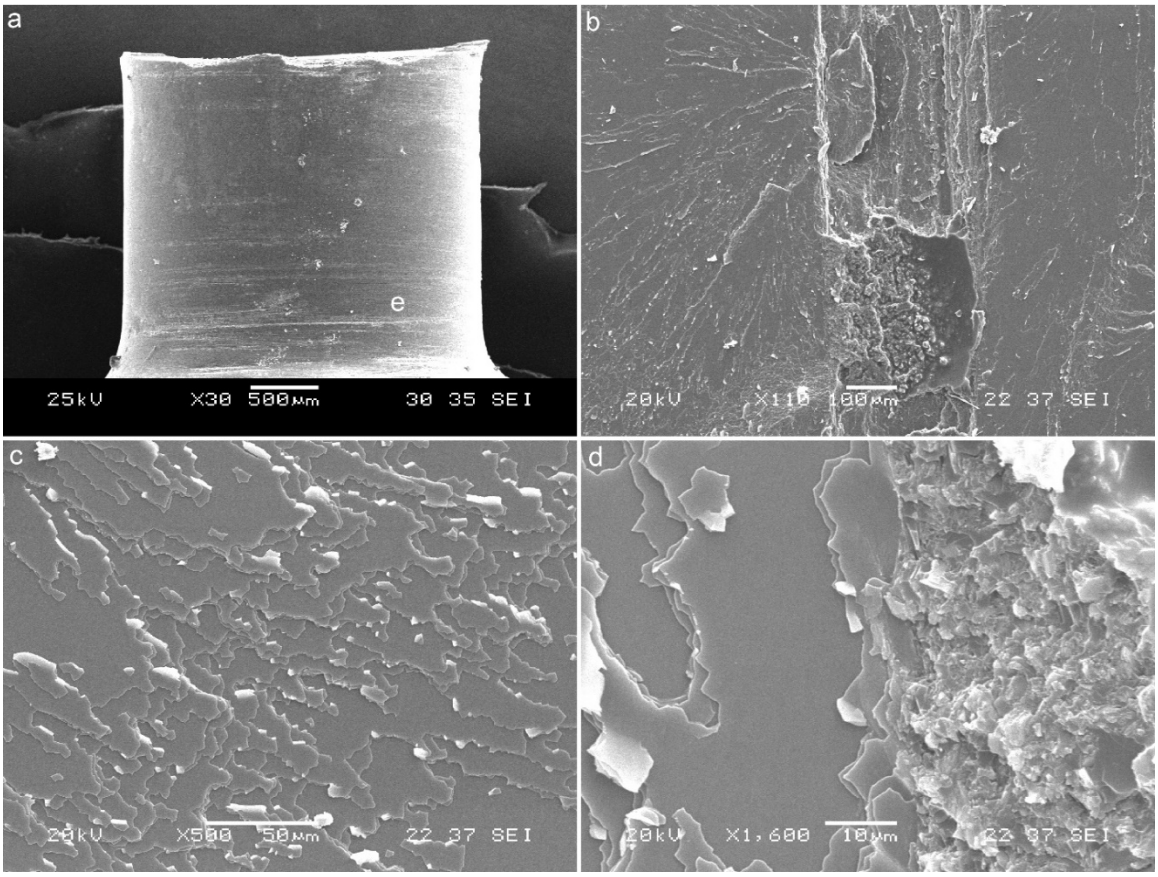

Figure S12: Fractural surfaces of the dry composite specimen under tension. (a) Side view of the fractured sample. (b) The aftermath separation between green matrix and spherulites. (c) Some areas are only occupied by nacre. (d) The transition from growth layers to nacre.

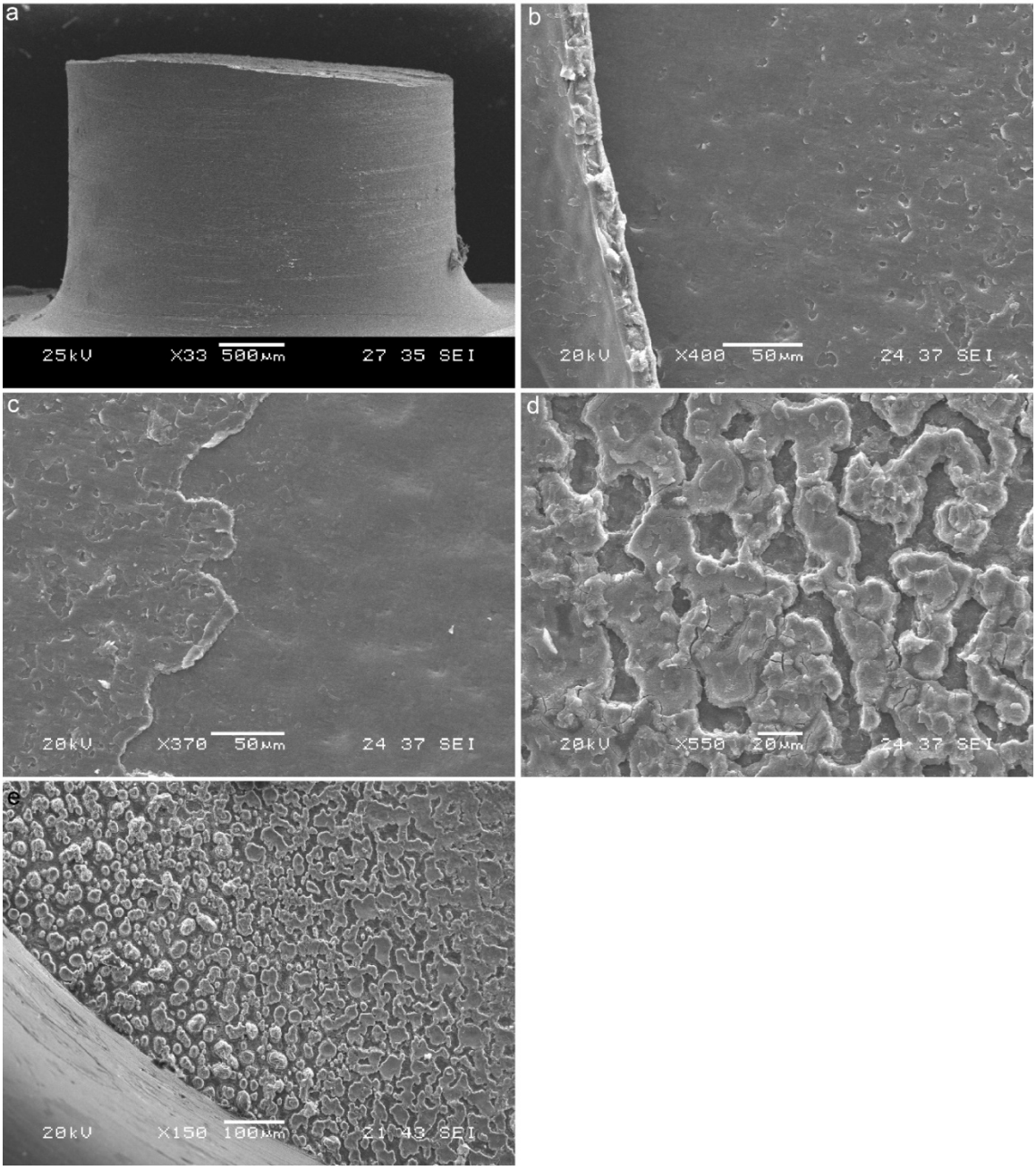

Figure S13: Fractural surfaces of hydrated composite specimen under tension. (a) Side view of the fractured sample. (b) layers of green matrix. (c) Delaminated layers in the green matrix. (d) Delaminated spherulites on the green matrix. (e) An aerial view of delaminated spherulites.

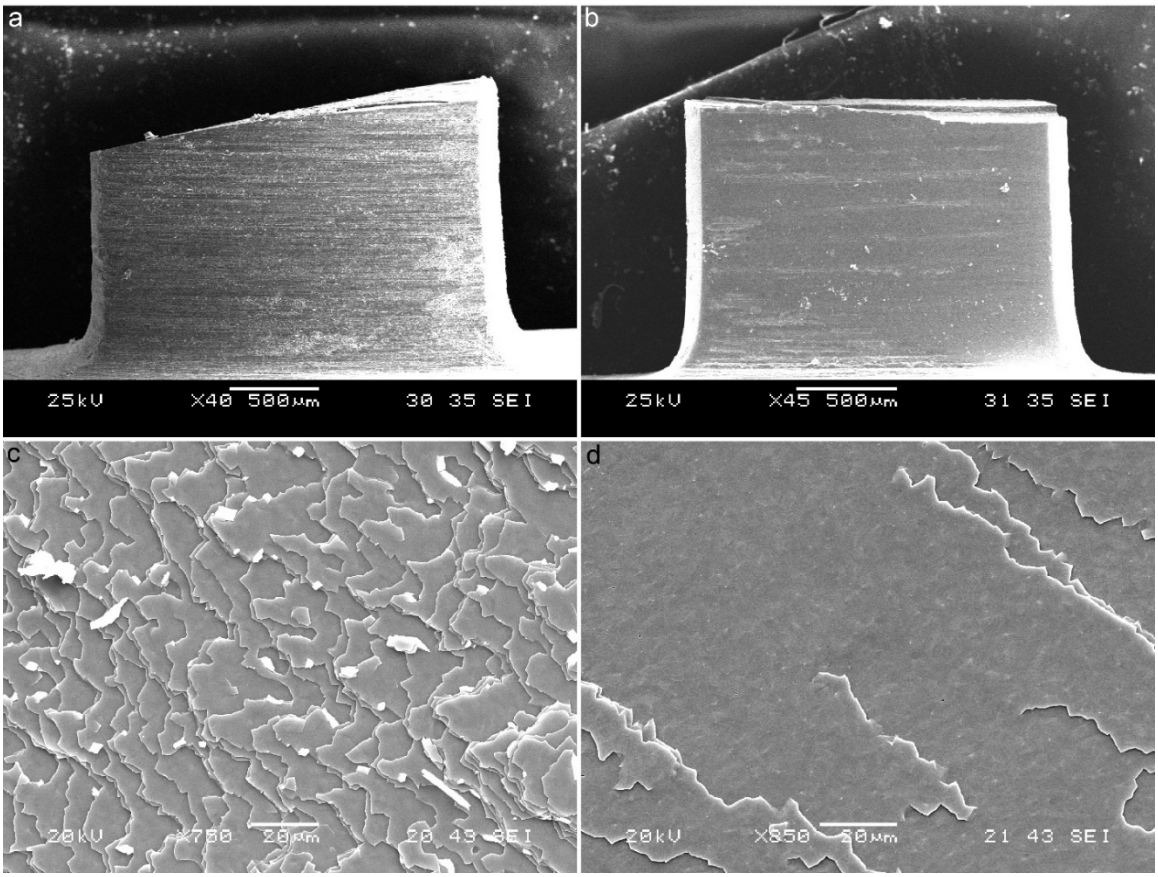

Figure S14: Fractural surfaces of dry (a, b) and hydrated (c, d) nacre specimens under tension. (a) Side view of the fractured dry nacre sample. (b) A close view showed the broken nacreous tablets due to tension. (c) Side view of the fractured hydrated nacre sample. (d) A close view showed the fractural surface.

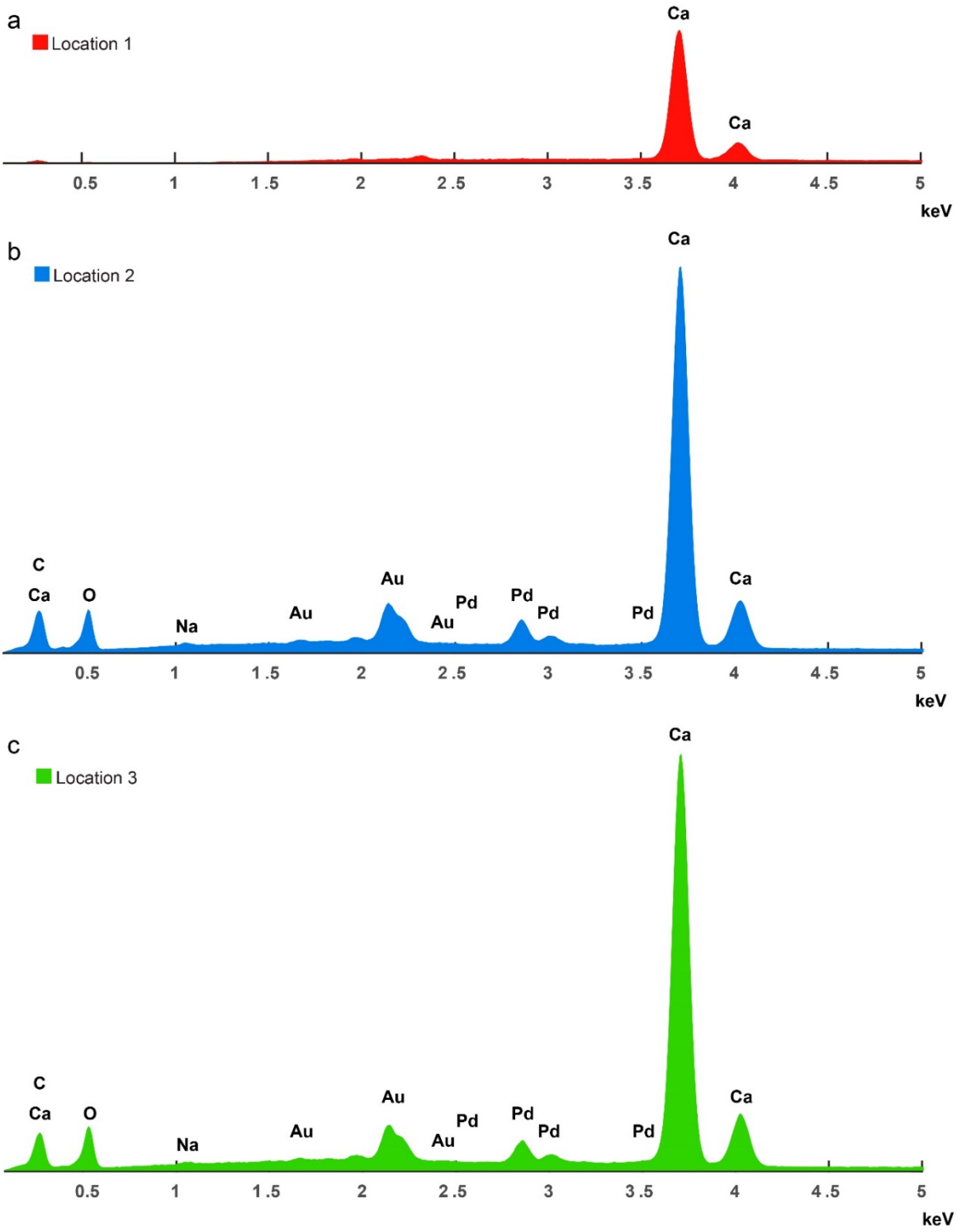

Figure S15: Pointwise EDS analysis of a tension-fractured hydrated composite. (a) point 1, (b) point 2 and (c) point 3 in Figure 10a of the main text.

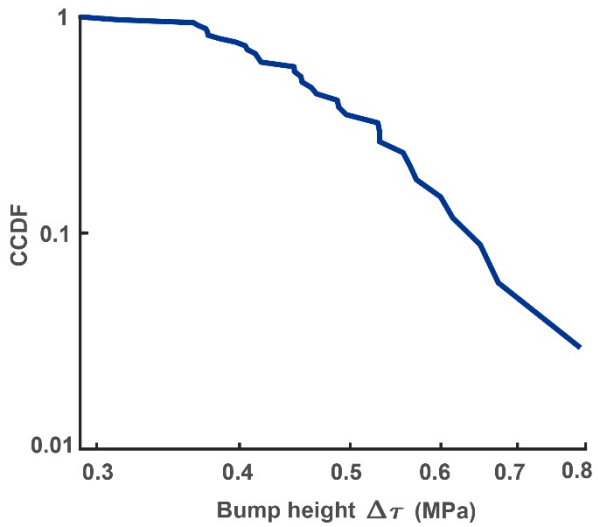

Figure S16: CCDF of stress bumps in hydrated nacre under torsion, adapted from Alghamdi et al. 2018 [1].

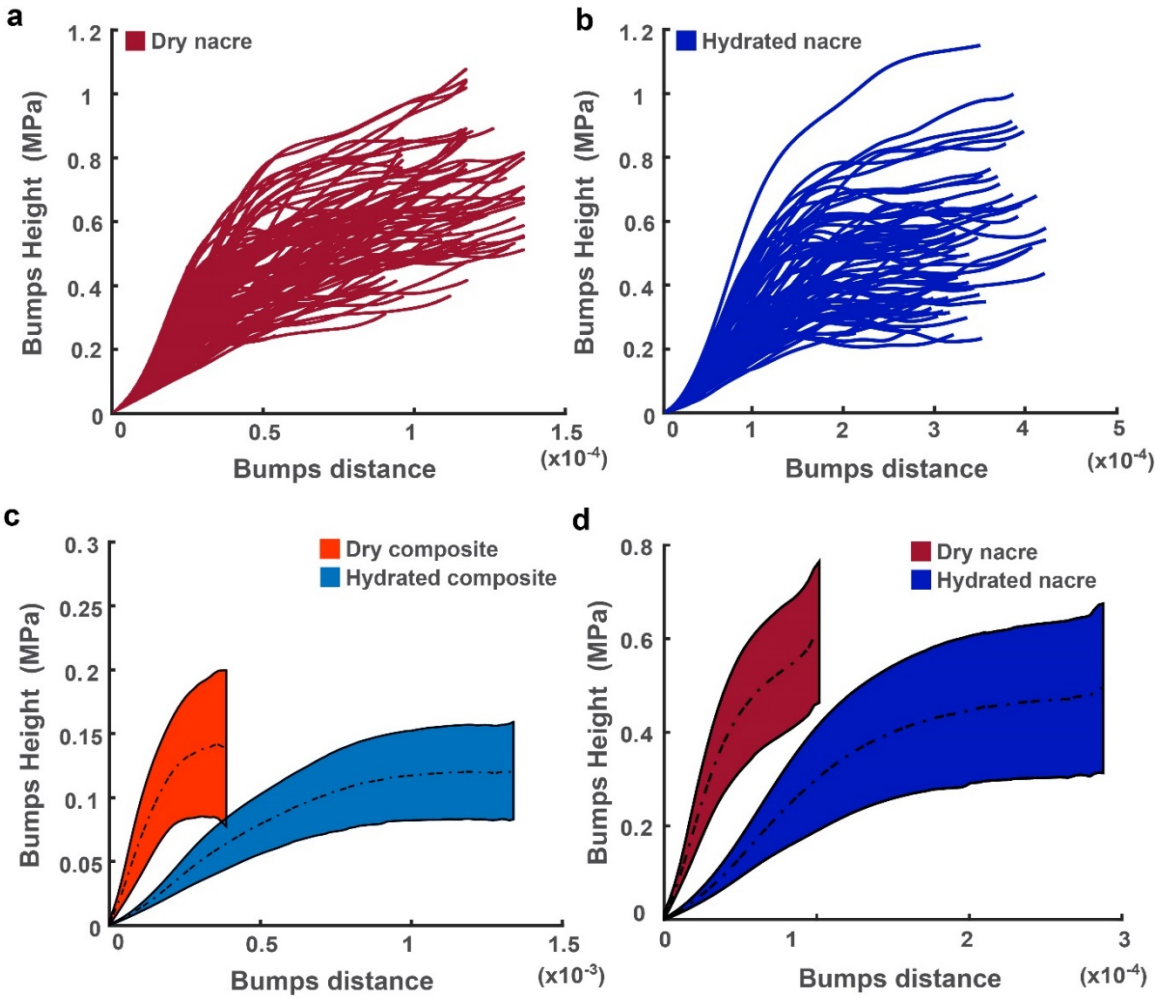

Figure S17: Statistical analysis on the overlapped bumps under tension (a) dry nacre, and (b) hydrated nacre. (c) Average bump shapes of dry and hydrated composites bounded by standard deviations. (d) Average bump shapes of dry and hydrated nacre bounded by standard deviations.

Appendix B References

[1] Alghamdi, S., Du, F., Yang, J., Tan, T., (2018). The role of water in the initial sliding of nacreous tablets: Findings from the torsional fracture of dry and hydrated nacre. *Journal of Mechanical Behavior of Biomedical Materials*, 88, 322-329.

[2] Alghamdi, S., Tan, T., Hale-Sills, C., Vilmont, F., Xia, T., Yang, J., Huston, D., Dewoolkar, M., (2017). Catastrophic failure of nacre under pure shear stresses of torsion. *Scientfic Reports*, 7, 13123.

[3] Alghamdi, S.J., (2016). A Preliminary Study on the interfacial strength of red abalone. *Master's thesis*. University of Vermont.